Università degli Studi di Napoli "Federico II"

DIPARTIMENTO DI INGEGNERIA INDUSTRIALE
Scuola di Dottorato in Ingegneria Aerospaziale Navale e della Qualitá
XXVIII Ciclo

Tesi di Dottorato in
Ingegneria Aerospaziale

Three-dimensional organization and heat transfer of jets with fractal generated turbulence

Gioacchino Cafiero

Coordinator:

Prof. Luigi de Luca

Tutors:

Prof. Tommaso Astarita
Prof. Stefano Discetti

Aprile 2016

Keep dreamin'!

Leland Melvin
(NASA Astronaut, IAC 2012)

Contents

Summary

Cooling of electronic devices, glass shaping and tempering, food processing, turbine blades cooling, paper and textile drying, airborne anti and de-icing devices are only few of the possible application fields of impinging jets for their high heat/mass transfer capabilities. Considering such a variegate portfolio of applications, it is not surprising that many efforts have been spent over the years to characterize the flow topology of impinging jets. In this sense, of particular interest is the identification of those agents that are responsible for the high scalar transfer of the jets. Two elements certainly have an overwhelming effect on it: the turbulence intensity level and the coherent structures produced by the jet. Use of different nozzle geometries, introduction of secondary flow components, insertion of mesh grids are all attempts to tamper with at least one of the aforementioned elements.

In this thesis, the use of fractal generated turbulence is proposed as an efficient mean to enhance the convective heat transfer rate of impinging jets. Starting from the exploratory work of Hurst and Vassilicos (2007), in the past 10 years a growing scientific community has devoted his interest towards multi-scale/fractal generated turbulence. Owing to the peculiar features of fractal grids (that will be introduced in chapter 1) and the effect that they have on the coherent structures organization, they are perfectly suited for the purpose of enhancing the jet scalar transfer capabilities. It will be showed that these grids (also referred to as turbulence promoters in

the following) can produce high turbulence intensity levels and sensitively enhance the jet entrainment rate. These grids have also been employed for other applications, such as fractal spoilers, modification to the leading edge of wings, promoters of a more efficient and stable combustion in burners among the others.

The results obtained in this thesis are organized in four different Chapters. Since the topic of fractal grids in turbulent jets is completely unexplored, the first step is the definition of the flow topology in the case of free jet (Chapter 4), i.e. without impinging plate. The flow field is explored both in terms of first and second order statistics and instantaneous organization. In order to best highlight the effect of the fractal grid onto the flow field, a comparison with a round jet without the turbulence promoter is carried out. Being the flow field highly three dimensional, volumetric data result to be extremely beneficial in terms of understanding of the complex organization of the coherent structure that characterize the flow field.

The effectiveness of fractal grids in terms of convective heat transfer enhancement is then assessed in Chapter 5, via dedicated IR Thermography experiments. A comparison with the well-known features of a round jet and an equivalent regular grid (i.e. with a similar blockage ratio) is carried out. Since the presence of the grid significantly reduces the passage area, the experiments are carried out under the same power input, i.e. the same product of the volumetric flow rate times the pressure difference between the stagnation chamber and the ambient (thus taking into account the pressure drop due to the grid).

The fluid dynamics mechanism that is hidden behind the higher convective heat transfer rate that characterizes fractal impinging jets is investigated in Chapter 6. The main differences with respect to the case of free jet are outlined both in terms of first and second order statistics. A particular attention is devoted to the vortical field organization, relating the flow features to the results obtained in Chapter 5.

Finally, a parametric study on the effect of the grid geometry onto the convective heat transfer rate is carried out in Chapter 7. Three different ef-

fects are taken into account: the fractal grid thickness ratio, the secondary grid iterations and the influence of the initial pattern.

CHAPTER 1

Introduction

The study of turbulent flows is considered one of the driving forces of the fluid dynamic research of the last few decades. The necessity of understanding the complex phenomena associated to turbulence represents the main goal in different application fields as aerospace engineering, biological flows (like in the human body), civil engineering to cite some. Provided the high complexity of the turbulent flows and the large amount of unknowns in the problem, one has to turn the attention to simplified scenarios; in this sense, of particular interest are the free shear flows: jets, wakes and mixing layers. These flows are remote from the walls and the turbulence arises because of mean-velocity differences (Pope, 2000). Their importance is mainly associated to the easiness both in the experimental and the numerical modelling. Despite their low complexity, many questions have found answers over the years looking at these basic flows and many others will be addressed in the future.

In a similar fashion, grid turbulence has always represented one of the best means to reproduce controlled and nearly-isotropic turbulence in wind tunnels. The necessity of finding suitable closures to the Navier-Stokes equations is indeed one of the main challenges especially for the numerical simulations. In this sense, many leads have been followed over the years

(regular grids, active grids, to cite some); in the last ten years, the use of fractal grids have provided a leap forward in the understanding of some fundamental aspects of free decaying turbulence.

In this Chapter, a review of the main features of free and impinging jets will be carried out in paragraph 1.1, with a particular focus on the round jet topology. Furthermore, the performances in terms of convective heat transfer of such jets when impinging onto a flat surface will be discussed. In paragraph 1.2 the main features of the grid generated turbulence are introduced. A short survey on the main findings over the years about the properties of freely decaying turbulence is carried out. Moreover, in paragraph 1.3 the main features of fractal generated turbulence are presented; with reference to the decaying turbulence region, a new model that significantly differs from the classic equilibrium turbulence is introduced.

1.1 Turbulent submerged jets

The importance of turbulent jets in a variegate portfolio of applications and the easiness in their modelling for the understanding of the basics laws of turbulence have made them one of the most investigated topics of the fluid dynamics research in the last decades. When a fluid with a certain amount of momentum is convected through a nozzle or an orifice and discharges in the same fluid with zero momentum, the jet is generally referred to as submerged jet (see Figure 1.1). In the next paragraphs, a description of the features of *free* and *impinging* jets will be provided in terms of mean and instantaneous flow field.

1.1.1 Free jets topology

The main features of a free turbulent round jet have been extensively detailed in the past (Abramovich, 1963; Crow and Champagne, 1971; Pope, 2000). The flow field can be generally subdivided into three main regions, as schematically represented in Figure 1.2:

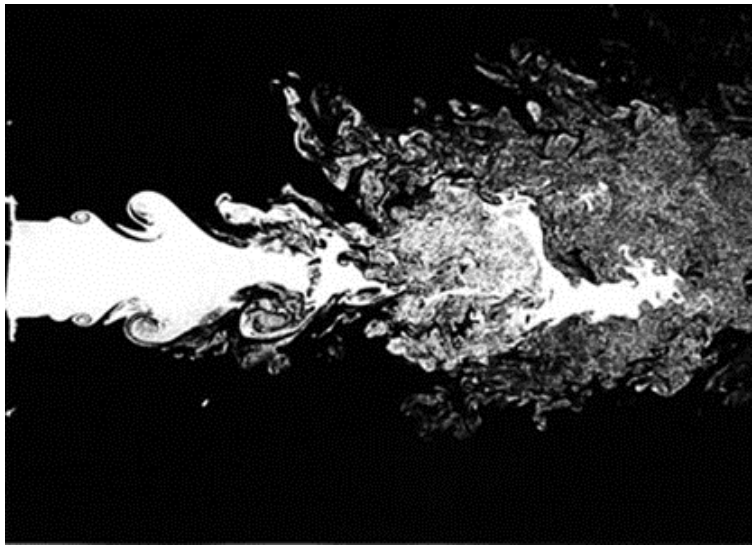

Figure 1.1: Turbulent jet visualization (image from the web `www.columbia.edu~rc16`).

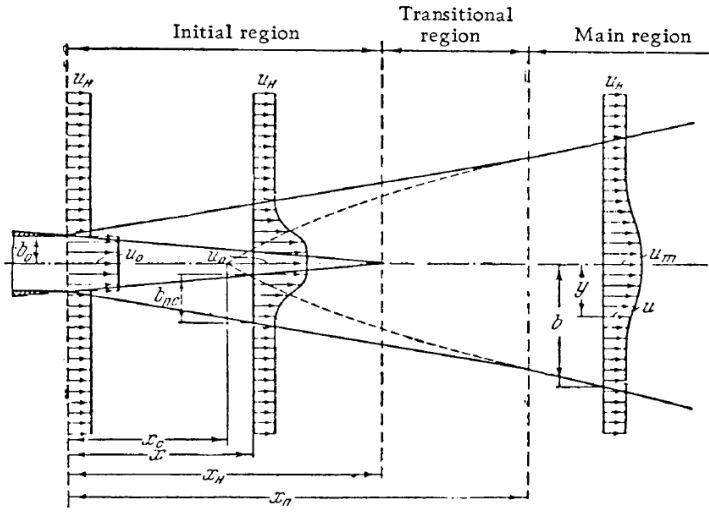

Figure 1.2: Diagram of a jet.

- an initial region, where the shear layer (i.e. the region where the velocity passes from a non zero value within the jet to a zero value outside of it) progressively penetrates towards the jet centreline; in this region, the presence of a *potential core* can be detected, where the shear effects are not present and the jet axial velocity is constant. The extent of this region can be up to $6.5d$ (Hussain and Zaman, 1981), being d the nozzle exit section diameter, basically depending on the different nozzle geometry;

- a transitional region, where the jet is completely affected by the shear layer and the velocity profile approaches a gaussian shape;

- a main region where the velocity profile becomes self-similar and the flow is generally referred to as fully developed; this region generally starts at about 8 d from the nozzle exit section.

As a consequence of the constance of the momentum, the velocity profile widens as progressively attains lower values, thus causing a spreading of the jet. This spreading is found to be linear, with a spreading rate ranging from 0.08 to 0.1 (Abramovich, 1963; Pope, 2000). It must be pointed out that, depending on the inlet conditions (i.e. depending on the nozzle length L over diameter d ratio and on the nozzle geometry), the jet spreading may occur few diameters apart from the nozzle exit section. This is the case, for example, of a short-pipe nozzle, where for about 2 d the jet width is constant. Beyond that point, the linear spreading occurs (Abramovich, 1963).

Whilst the momentum is constant in a turbulent jet, the mass flow rate progressively increases as a function of the longitudinal coordinate. Indeed, due to the momentum difference between the jet core and the quiescent fluid, an entrainment arises. This condition is favourable to the triggering of a shear layer instability generally referred to as Kelvin-Helmholtz instability, which is responsible of the entrainment process. The amplification of these disturbs within the jet shear layer, breaks into the gener-

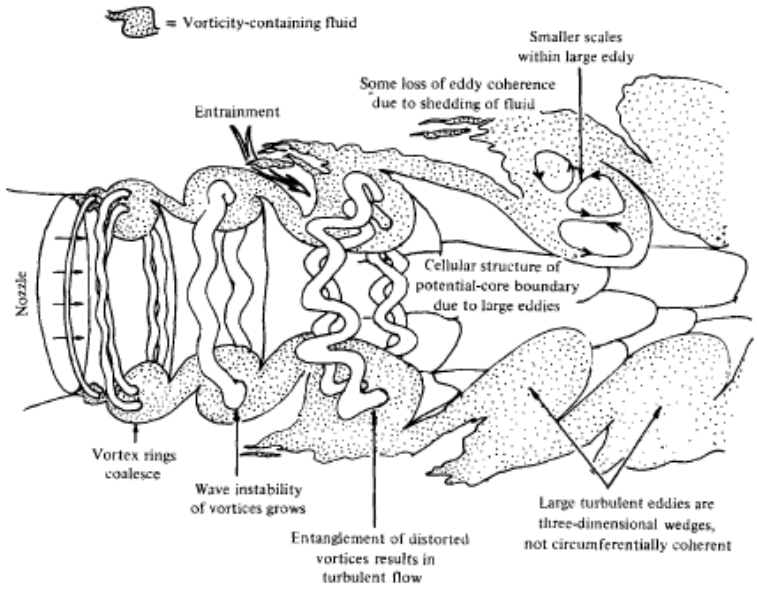

Figure 1.3: Schematic representation of a transitional jet in the vicinity of the nozzle exit section (from Yule, 1978).

ation of ring vortices (Becker and Massaro, 1968; Crow and Champagne, 1971; Yule, 1978) that embrace the jet core, as represented in Figure 1.3. These structures grow in size keeping the axial symmetry for few diameters. However, when convected downstream, their distance progressively reduces, thus leading to the pairing phenomenon (Schram et al., 2004). As a consequence of the pairing, the large structures loose their coherence and their breakdown occurs. The two reported phenomena are the main responsible for the production of noise in transitional jets (Violato and Scarano, 2013).

Liepmann and Gharib (1992) showed that a secondary flow instability also develops in the braid region between two subsequent ring vortices (referred to as primary instabilities), as shown in Figure 1.4. They result from the amplifications of the small disturbs that propagate within the jet shear layer and affect the axial symmetry of the primary structures.

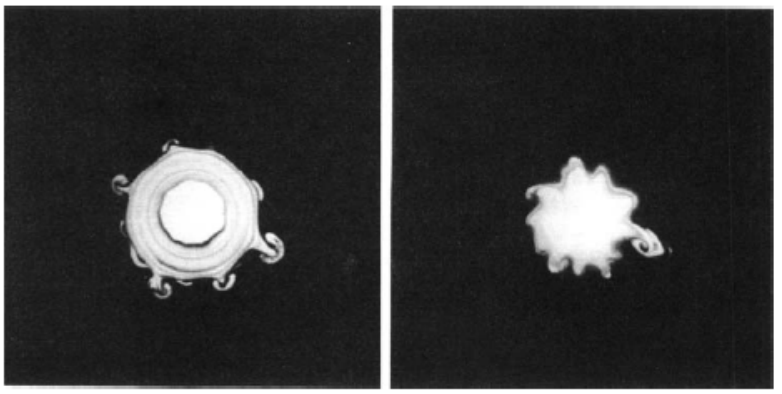

Figure 1.4: LIF cross-section of a round jet at a streamwise distance of 2.5 d from the nozzle exit section: left ring vortex, right braid region (from Liepmann and Gharib, 1992).

Indeed, a perturbation to the primary vortex leads to the tilting of the vorticity vector; as a consequence, an axial vorticity component is induced. Liepmann and Gharib (1992) demonstrated that these streamwise vortices are actually of primary importance in the entrainment mechanism. Indeed, differently from the ring vortices, they do not have an oscillating effect on the local entrainment rate; furthermore, whilst the ring vortices loose strength and effectiveness beyond the potential core, at a distance of about 10 d from the nozzle exit section the streamwise vortices are still effective.

As the entrainment rate is directly related to the scalar transfer of a jet, numerous investigations have been devoted to enhance the production of streamwise vorticity. Gutmark and Grienstein (1999) deeply investigated the flow field generated by non-circular geometries; they showed that the Kelvin-Helmholtz instabilities are still present in this case, but the nozzle geometry affects the vorticity field. Indeed, instead of an azimuthally coherent structure, a non-circular nozzle produces a structure that resembles (at least in the vicinity of the nozzle exit section) its geometry, thus presenting a non-uniform curvature. This condition is favourable for the stretching of the structure and, in a similar fashion to what occurs to round

nozzles, for the induction of streamwise vorticity. A similar argument can also be posed for cross-shaped geometries, as those described in El-Hassan et al. (2011).

The use of non-circular geometries is also effective from the noise reduction standpoint. The wide diffusion in the aeronautic engines industry of the chevron geometry for the exhaust nozzles is related to the lower noise level associated to this geometry with respect to the conventional one. Indeed, the chevron nozzle disrupts the ring vortex and converts vorticity from the azimuthal to the streamwise component. Its effect is then twofold: from one side, the absence of the ring vortex clearly avoids its breakdown, thus attaining a lower noise level (Violato and Scarano, 2011); from the other, the streamwise vorticity enhances the entrainment rate and as a consequence, the scalar transfer of the chevron nozzle (Violato et al., 2012).

1.1.2 Impinging jets: flow field and heat transfer features

The flow topology of impinging jets is affected by the adverse pressure gradient induced by the presence of the impinged plate. Numerous reviews were dedicated to the topic over the last years, trying to point out both the flow field topology and the heat and mass transfer properties of impinging jets (Martin, 1977; Polat et al., 1989; Jambunathan et al., 1992; Viskanta, 1993; Carlomagno and Ianiro, 2014). Similarly to the free jet case, the impinging jet flow field can be subdivided into several regions, as schematically represented in Figure 1.5.

In the first region, the jet is sufficiently far from the impingement surface thus behaves as a free submerged jet. This region is referred to as free jet region. Similarly to what already described in the previous section, the interaction of the emerging jet with the quiescent fluid triggers a shear-driven entrainment of mass, momentum and energy towards the jet core. However, as already mentioned, a portion of the jet is not affected by these

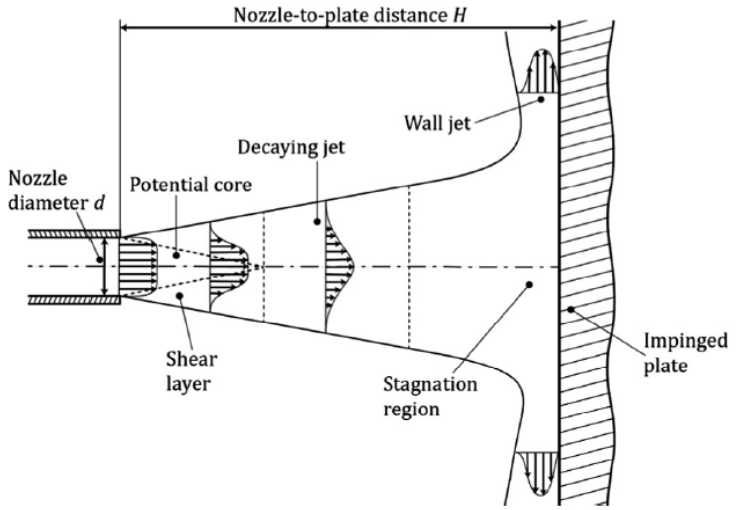

Figure 1.5: Schematic representation of the flow regions of a round impinging jet (from Carlomagno and Ianiro, 2014).

exchanges, and it is generally referred to as potential core. The extent of this region is related to the turbulence level at the nozzle exit section and to its geometry, as well as the nozzle to plate distance.

Beyond the potential core, the jet undergoes the flow developing region and it is basically equivalent to the intermediate region already discussed in the free submerged jets. Afterwards, the jet enters the fully developed region; these two regions are generally referred to as decaying jet region, where the axial velocity continuously decreases and the velocity profile can be well-approximated by a gaussian (Reichardt, 1943).

When the jet approaches the plate, the flow decreases its axial velocity and it is forced to experience a change of direction in the so called quasi-stagnation region. In particular, the momentum is practically transferred from the axial to the radial component. This leads to an increment in the static pressure that is propagated upstream.

Downstream of the stagnation region, the flow develops parallel to the

impinged plate entering the so called wall jet region. The flow is accelerated up to a maximum value that occurs at a radial distance of about one nozzle diameter from the stagnation point. In this region the boundary layer thickness grows, entraining fluid from the ambient and the maximum in the velocity profile progressively moves apart from the impinged plate; furthermore, the mean value in the velocity profile reduces. Finally, in the fully developed wall jet region, the flow becomes self-similar, with the maximum in the radial velocity that reduces down to zero as the distance from the stagnation region increases.

It must be pointed out that, at short nozzle to plate distances, some of the previously described regions may disappear. In particular, this is the case of the fully developed region that generally disappears for Y/d values smaller than 4-5 nozzle diameters. When the distance is further reduced, the whole decaying jet region may disappear.

Large scale structures triggered by Kelvin-Helmholtz instabilities are also present in the case of impinging jets. In particular, these structures develop in the jet shear layer before impinging onto the plate. They then experience an acceleration due to the conversion of the axial momentum into its radial component. In the vicinity of the impingement plate, the ring vortices interact with the boundary layer, producing its local separation at about 1.5-2d from the nozzle axis. In correspondence of this separation, a secondary structure, counter-rotating with respect to the first one, can be produced (Hadžiabdić and Hanjalić, 2008, see also for example Figure 1.6, 1.7, 1.8).

The convective heat transfer properties of round impinging jets have been detailed in numerous investigations (see Martin, 1977; Hoogendoorn, 1977; Jambunathan et al., 1992; Viskanta, 1993; O'Donovan and Murray, 2007 to cite some). As already mentioned, they result extremely performing when a high convective heat transfer rate is required. The convective heat transfer is generally presented in terms of the Nusselt number $Nu = hd/k$, being h the convective heat transfer coefficient, d a reference length (the nozzle diameter in the case of a round jet) and k the fluid ther-

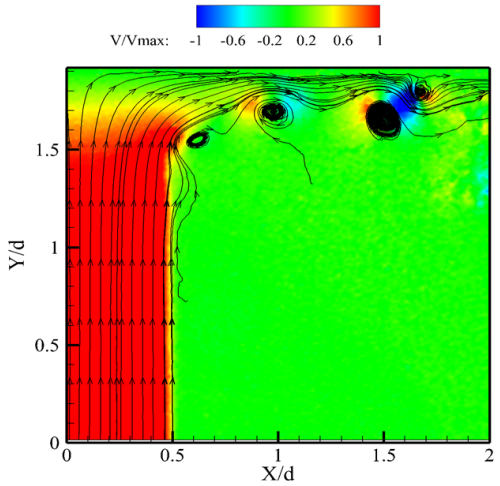

Figure 1.6: PIV instantaneous realization of a round impinging jet at a nozzle to plate distance equal to 2 nozzle diameters and $Re = 10,000$. Contour representation of the normalized axial velocity V/V_{max}, being V_{max} the maximum velocity. The primary and secondary vortices can be detected at $X = 1.5d$ with a local displacement of the streamlines apart from the impingement plate.

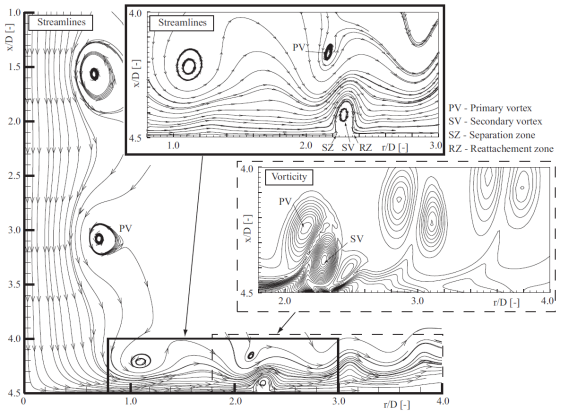

Figure 1.7: Instantaneous flow field of a laminar round impinging jet (from Rholfs et al., 2012).

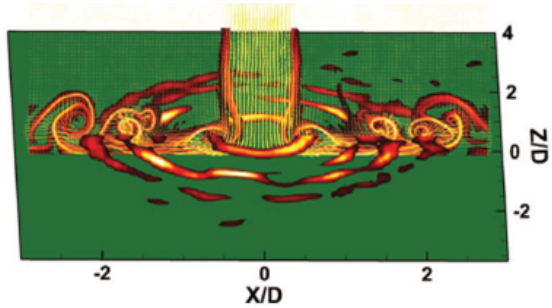

Figure 1.8: 3D view of the Lagrangian coherent structures, color coded according to the FTLE (Finite-time Lyapunov exponent) values (from El-Hassan et al., 2013).

mal conductivity. At the stagnation point, at relatively short nozzle to plate distances H, the Nu values increase as H/d increases. In particular, this is associated from one side to the fact that the axial velocity is nearly constant within the potential core, whose extent ranges from 4.5 to 6 d; on the other side, the progressive penetration of the shear layer towards the jet axis produces an increment of the convective heat transfer rate. Beyond this limiting distance, which one could associate to the extent of the potential core itself, the stagnation point Nu monotonically decreases.

As the distance from the nozzle axis increases, for short nozzle to plate separations the radial Nu profile presents a double peak radial distribution (see Figure 1.9). An inner peak, located at about 0.5 d from the axis, is addressed to the concurrent effect of the impinging jet shear layer and to the high values of the impinging jet axial velocity, which then convects a large amount of fluid in this region, causing an increment of the heat transfer rate. As shown also by the flow field results, the fluid converts its axial velocity into a radial component, accelerates but then experiences a local separation due to the effect of the secondary vortex, as reported in Figure 1.7. This has two direct consequences: first, the local separation produces a minimum in the heat transfer rate; second, downstream of the separation, the reattaching fluid produces a further enhancement of the

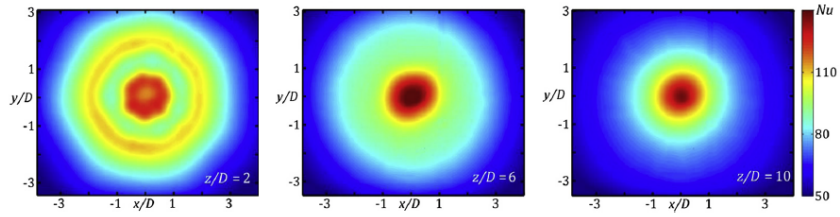

Figure 1.9: Nusselt number distributions of a circular impinging jet at three nozzle to plate distances, namely $2d$, $6d$ and $10d$ (from Ianiro and Cardone, 2012).

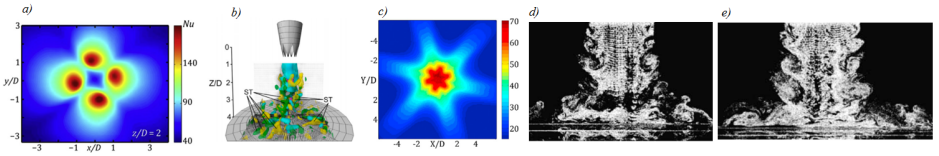

Figure 1.10: a) Nusselt number distribution of a swirling impinging jet at a nozzle to plate distance equal to $2d$ (from Ianiro and Cardone, 2012); b-c) Three dimensional flow organization and Nusselt number distribution of a chevron impinging jet (from Violato et al., 2012); d-e) Flow field visualization of an impinging orifice jet with mesh screens with different blockage ratios (from Zhou and Lee, 2004).

Nu values (see Figure 1.9). Depending on the nozzle geometry and on the upstream turbulence level, the second maximum is generally located at radial separations from the nozzle axis ranging from 1.5 to 2 d. For nozzle to plate distances larger than $6d$, the Nu radial profile is monotonically decreasing, as from one side the axial impinging velocity decreases; from the other, the primary ring vortex at the impinging plate is not strong enough to cause the wall boundary layer separation and. In the wall jet region, the Nu values monotonically decrease.

In the case of non-circular nozzle geometries, the Nusselt number distribution may sensibly differ from the picture above described. Rau et al. (2014) showed that when using cross-shaped nozzles, as a consequence of

the produced streamwise vorticity the impinging jet may experience an axis-switching, thus leading to regions of maxima in the convective heat transfer rate tilted with respect to the nozzle principal directions. Huang and El-Genk (1998) demonstrated that the application of an upstream swirl component to the main flow file may lead to a significant enhancement of the convective heat transfer rate (see Figure 1.10a). Violato et al. (2012) showed that the use of a chevron nozzle leads to an increment of the convective heat transfer rate in the vicinity of the nozzle axis, but on the downside a sensitive decrease in the Nu uniformity (see Figure 1.10c).

Another typical mean to enhance the heat transfer rate of impinging jets is the use of grids or mesh screens. Zhou and Lee (2004) investigated the heat transfer rate of a sharp-edged orifice with a mesh screen placed $1.4d$ upstream of the outflow section (see Figure 1.10d-e). Their results highlight that the achieved heat transfer enhancement is very limited (only 3.6% in the stagnation point). In a subsequent study, Zhou et al. (2006) have shown that a more consistent improvement can be obtained if the grid is placed right before the orifice, with an increase of about 27% of the Nusselt number in the stagnation point for a grid with blockage ratio of 25% and nozzle-to-plate distance equal to 0.2.

The outcome of these considerations is that tampering with the large scale structures organization and the turbulence intensity level may produce a significant increment of the convective heat transfer rate. In the next paragraph, the turbulence characteristics of fractal grids will be introduced in the broad scenario of grid generated turbulence. Their peculiar features in terms of turbulence intensity profile will be detailed. In the next chapters, it will be shown that these grids are also particular efficient in producing streamwise vorticity. As a consequence, the applications of these grids with the purpose of enhancing the convective heat transfer rate will be detailed.

1.2 Fundamental aspects of decaying turbulence

In this paragraph some general aspects of turbulent shear flows will be discussed, with a particular attention to grid generated turbulence. This topic has been extensively studied since the beginning of the last century, due to the peculiar property of producing a quasi-isotropic turbulent flow (both locally and globally) far enough from the grid. This is particularly favourable for investigating the turbulence characteristics in the decaying region. Indeed, especially for the closure of the numerical models (as the Reynolds averaged Navier Stokes equations) additional conditions on the turbulence behaviour are necessary. The first steps in this direction were moved by Richardson in 1922 (see Richardson, 1922), who proposed a picture of turbulence based on a cascade of eddies: *big whirls have little whirls which feed on their velocity ... and so on to viscosity.* The main idea of Richardson's work, that will be then followed by Kolmogorov, is that the large-scale eddies of size l and characterized by a turbulent kinetic energy K (*tke*) extract energy from the flow they are embedded in through the Reynolds stresses. The *tke* is then transferred to smaller and smaller eddies. This phenomenon is interrupted when the size of the eddies is such that $\sqrt{K_n} l_n \approx \nu$ (the subscript n indicating the n-th energy transfer where the size of the eddies is such that the local Reynolds number is approximately unitary, thus making ν the fluid kinematic viscosity). At this stage, they lose their energy due to dissipation (into heat).

Successively, Kolmogorov (1941) extended Richardson's findings to an arbitrary turbulent flow with a large Reynolds number value. He hypothesized that the large scale eddies are the energy containing ones and the small eddies are responsible of the dissipation. The latter are in statistical equilibrium and depend on the viscosity ν and on the energy transfer that occurs from the large scales to the small ones. In addition to the previous works, he also defined from a dimensional analysis a functional

expression for the small length-scales, that is generally named after him as Kolmogorov length-scale, $\eta = (\nu^3/\epsilon)^{1/4}$. Furthermore, he argued that between the large scales and the dissipative ones, there must be an intermediate region, referred to as *inertial subrange*, where the spectrum of the velocity field follow a $k^{-5/3}$ power law, with k indicating the spectral wavenumber.

Basing on phenomenological observations, (Taylor, 1935a,b) proposed a valuable scaling for the turbulence dissipation rate as function of the size of the large scale eddies l and the *tke*, in particular $\epsilon \propto \sqrt{K^3}/l$. Due to the astonishing versatility of this expression, and its independence on the molecular viscosity, it is currently used in numerous applications and turbulence models, as $K - \epsilon$ (see Pope, 2000) and Large eddy simulation (LES, see Pope, 2000). It is generally expressed in the form:

$$C_\epsilon = \frac{\epsilon L}{u'^3} \approx constant \tag{1.1}$$

where u' is representative of the root mean square of the streamwise velocity fluctuation, and L the streamwise lengthscale that can be evaluated as the autocorrelation function of u'. In this framework, C_ϵ is generally considered as a constant independent on time, space and Reynolds number, provided that its value is large enough. However, a word of warning came from Taylor (1935a), who argued that the C_ϵ value must not be considered as a constant, irrespective of the boundary conditions where the turbulence is produced. Equation 1.1 is generally referred to as *the cornerstone assumption* of any turbulence theory and model (Tennekes and Lumley, 1972). However, despite the simplicity of the equation 1.1, there are several implications; it indeed fixes the dissipation rate dependence upon the longitudinal coordinate. Moreover, it also identifies the relation between scales of the motion, as for example the ratio between the integral and Kolmogorov lengthscale is fixed to $L/\eta \approx Re_L^{3/4}$, being $Re_L = u'L/\nu$. Notwithstanding its importance in the turbulence modelling scenario, not much work was done to confirm the constancy of C_ϵ during the fifty year

successive to Kolmogorov work. Batchelor (1953) collected data obtained in the lee of regular grids with different mesh sizes and two wind tunnel velocities. Although a rather relevant scatter in the data distribution was found, both Sreenivasan (1984) and Lumley (1992) concluded that a power-law dependence of C_ϵ could not be argued and suggested that for $Re_\lambda > 100$, being λ the Taylor microscale [1], the constancy of C_ϵ is respected. Sreenivasan (1984) also suggested that, also confirming what stated by Taylor (1935a), the value achieved by C_ϵ could be dependent on the inlet boundaries.

Starting from the first 90's, also thank to the increasing calculation capabilities of computers and the possibility of numerically simulate sufficiently high local Reynolds numbers, numerous development were introduced in the field, that then culminated with the study of fractal generated turbulence and the new dissipation law for nonequilibrium turbulence. In the next paragraph the main features of fractal generated turbulence are introduced and the discrepancies with respect to equation 1.1 are outlined.

1.3 Fractal generated turbulence

Hurst and Vassilicos (2007) carried out a pioneering work where they investigated the decay features of fractal generated turbulence. They performed hot wire anemometry studies on 21 different fractal grids installed in two different wind tunnel facilities. The fractal grid is obtained by repeating the same pattern at increasingly smaller scales. Three patterns where investigated: "I", "cross" and "square". The most interesting findings were related to the latter. Differently from classical grid turbulence, in the case of fractal generated turbulence the streamwise velocity fluctuation presents an elongated production region where the turbulence intensity level builds up, a local peak and a fast decay; moreover, the extent of the

[1] the Taylor microscale is defined through the relation $\left(\frac{\partial u'}{\partial x}\right)^2 = \frac{u'^2}{\lambda^2}$; for isotropic turbulence, this relation reduces to $\lambda_{ISO}^2 = 15\nu u'/\epsilon$

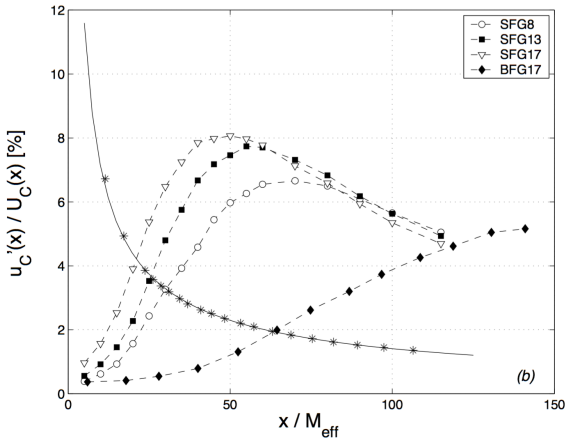

Figure 1.11: Streamwise velocity fluctuation for a regular grid ($\star$) and different square fractal grids as a function of the grid thickness ratio (from Hurst and Vassilicos, 2007).

production region is related to the grid geometry, as reported in Figure 1.11. In the decay region, Hurst and Vassilicos (2007) and successively Gomes-Fernandes et al. (2012) and Valente and Vassilicos (2011) found that the fractal generated turbulence was sufficiently isotropic. The striking difference with respect to the regular grids turbulence was related to the fact that the decay rate could be fitted with an exponential instead of a classical power law. In addition to that, the longitudinal integral length scale and the Taylor microscale both showed only a slight growth with the streamwise distance. Seoud and Vassilicos (2007) showed that $L/\lambda \approx const$ and Re_λ is a decreasing function of the longitudinal coordinate. This behaviour is at odds with equation 1.1, and represents the first clear break of the so-called dissipation anomaly (as it is generally referred to equation 1.1).

Subsequently, Mazellier and Vassilicos (2010) introduced the wake-interaction lengthscale x^*. This quantity is particularly significant from the turbulence intensity profile standpoint. It is defined in terms of the

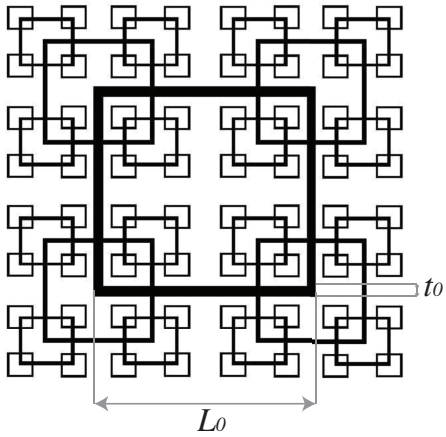

Figure 1.12: Schematic representation of a square fractal grid.

largest grid bar length and thickness (L_0 and t_0 respectively, see Figure 1.12). Following Prandtl's mixing length theory, they assumed that the characteristic size of the wake generated by the grid bar having thickness t_0 would be $L_0 \approx \sqrt{t_0 x}$, considering that the other grid iterations have no effect on the spreading of this wake. This leads to the expression for the wake interaction length-scale:

$$x^* = L_0^2/t_0 \tag{1.2}$$

It physically represents the longitudinal distance where the wakes detaching from the largest grid iterations would meet in the case they were isolated. They found this parameter particularly significant as it represents a valid scaling parameter for fractal generated turbulence. Indeed, the turbulence intensity peak can be expressed as a solely function of the wake

interaction lengthscale x^* as in equation 1.3 [2].

$$x_{peak} = 0.45x^* \tag{1.3}$$

This result is general, and also applies to regular grids, substituting the effective meshlength M to L_0. Using this scaling, they found a perfect collapse of all the streamwise velocity fluctuations profiles, independent on the thickness ratio as reported in Figure 1.13. The fact that the scaling in the turbulence intensity profile was the same represented the first indication of the possibility that the findings associated to fractal generated turbulence might be more general. Indeed, these findings paved the way to a new approach to the decay turbulence modelling, which is generally referred to as nonequilibrium turbulence (Vassilicos, 2015; Valente and Vassilicos, 2015; Castro, 2016).

Mazellier and Vassilicos (2010) also showed a slightly different scenario from what previously seen in Seoud and Vassilicos (2007): both the integral and Taylor microscale were slightly increasing function of the longitudinal distance, thus making their ratio still a constant. Furthermore, they also resulted to be dependent on the inlet velocity (i.e. on the global Reynolds number). Investigating a significantly larger portion of the wind tunnel, they also showed that the decay could be fitted with a fast power law instead of an exponential.

To summarize, the results obtained in the decay region of turbulence generated by square fractal grids are such that:

$$L/\lambda \approx Re_0^{\alpha} A\Big(\frac{x - x_0}{x^*}\Big) \tag{1.4}$$

and

$$Re_{\lambda} \approx Re_0^{\beta} B\Big(\frac{x - x_0}{x^*}\Big) \tag{1.5}$$

[2] This scaling was corrected to account for free stream turbulence intensity in Gomes-Fernandes et al. (2012) and showed a better agreement for results obtained with different inlet conditions.

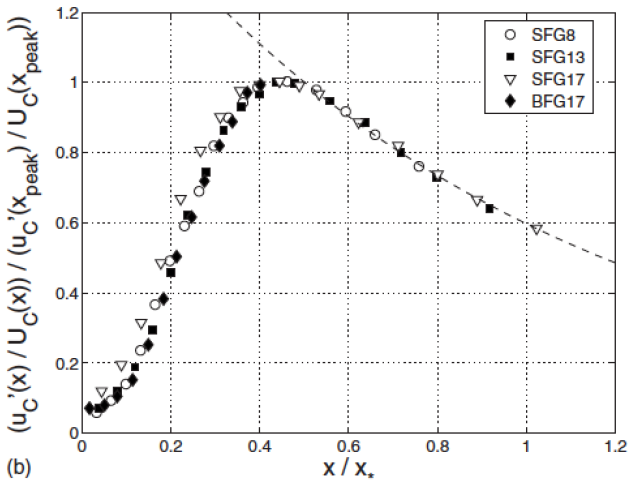

Figure 1.13: Streamwise velocity fluctuation intensity as a function of the normalized distance from the grid. The measurements are taken on the centreline of the wind tunnel (from Mazellier and Vassilicos, 2010).

being Re_0 the global Reynolds number, i.e. based on the inlet velocity and on the integral lengthscale, A an approximately constant function, B a steep power law, α and β positive real numbers.

Both Hurst and Vassilicos (2007) and later Gomes-Fernandes et al. (2012) showed that both the global and local isotropy values are close to be unitary[3]. This enabled them to use $\epsilon = 15\nu u'^2/\lambda^2$, which along with equation 1.1 leads to:

$$L/\lambda = \frac{C_\epsilon}{15} Re_\lambda \tag{1.6}$$

From equation 1.6 it is possible to see that, being Re_λ a decreasing function of x and L/λ nearly constant, C_ϵ cannot clearly be constant. Using 1.6 in conjunction with equations 1.4-1.5, Valente and Vassilicos (2011) expressed

[3] The global isotropy is measured as the ratio between the streamwise and crosswise velocity fluctuation; the local isotropy is instead measured of the velocity derivatives (Pope, 2000)

the functional dependence of C_ϵ on the longitudinal coordinate x as:

$$C_\epsilon = 15 Re_0^{\alpha-\beta} \frac{A\left(\frac{x-x_0}{x^*}\right)}{B\left(\frac{x-x_0}{x^*}\right)} \tag{1.7}$$

Equation 1.7 shows that C_ϵ rapidly increases as a function of the longitudinal coordinate (because of B) and also depends on the global Reynolds number Re_0 (see Figure 1.14). The reported data are relative to a regular grid and a fractal grid for different wind tunnel inlet conditions (i.e. asymptotic speed).The dashed-dot lines follow the form Re_λ^{-1}. The dependence on the local Reynolds number predicted by equation 1.7 is respected. Furthermore, as expected, the values attained by the fractal grids in terms of local Reynolds number are significantly larger than those of the regular grid.

In their experiments Valente and Vassilicos (2011) tested both a square fractal grid and a regular grid with the purpose of validating their findings. In particular the use of a regular grid was twofold: first it enabled to extend their results to the more general case of classic grid and second, considering the significantly smaller x^* value, it was useful to detect the extent of validity of their dissipation scaling. They found that at a certain distance from the grid (about $x > 5x_{peak}$, see Figure 1.15) a sudden change in the C_ϵ curve is experienced that is related to the transition from the dissipation scaling law $C_\epsilon \approx Re_0^m / Re_\lambda^n$ to the well known equation 1.1.

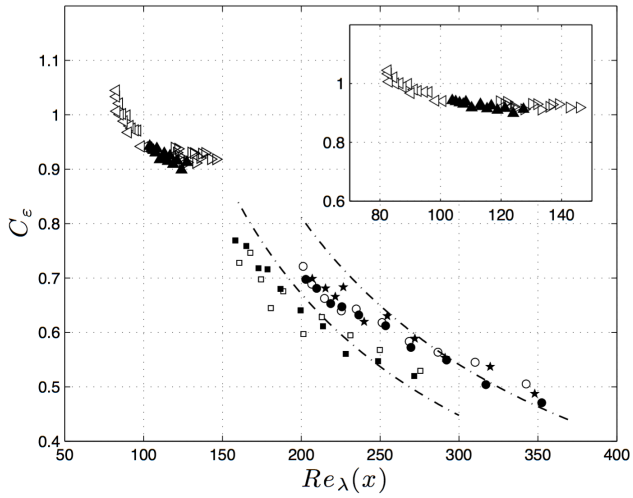

Figure 1.14: Dependence of the turbulence dissipation rate C_ϵ on the local Reynolds number values Re_λ for both regular and fractal grids at different inlet velocities. (■) FSG $U_\infty = 10ms^{-1}$, $l_w = 1mm$, (□) FSG $U_\infty = 10ms^{-1}$, $l_w = 0.45mm$, (●) FSG $U_\infty = 15ms^{-1}$, $l_w = 1mm$, (○) FSG $U_\infty = 15ms^{-1}$, $l_w = 0.45mm$, (⋆) FSG $U_\infty = 15ms^{-1}$, $l_w = 0.2mm$, (◁) RG $U_\infty = 10ms^{-1}$, $l_w = 0.45mm$, (▲) RG $U_\infty = 15ms^{-1}$, $l_w = 0.45mm$, (▷) RG $U_\infty = 20ms^{-1}$, $l_w = 0.45mm$. From Valente and Vassilicos (2011).

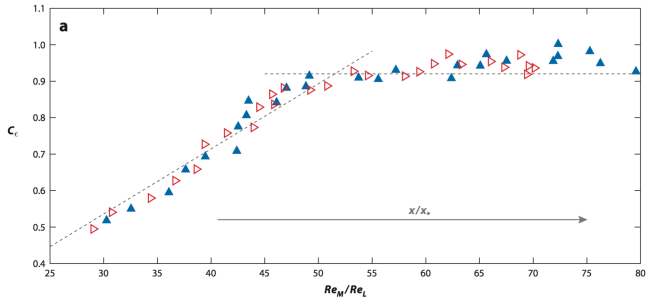

Figure 1.15: Dependence of the turbulence dissipation rate C_ϵ on the local Reynolds number values Re_λ for regular grids at different inlet velocities. (◁) $U_\infty = 10ms^{-1}$, $l_w = 0.45mm$, (▲) $U_\infty = 15ms^{-1}$, $l_w = 0.45mm$, (▷) $U_\infty = 20ms^{-1}$, $l_w = 0.45mm$. From Vassilicos (2015).

CHAPTER 2

Tomographic Particle Image Velocimetry

In this chapter the basic principles of Particle Image Velocimetry (PIV) will be presented and discussed. Some of the main aspects that must be taken into account when designing either a planar or volumetric PIV experiment are introduced. A more detailed description of the necessary steps to perform a tomographic PIV experiment is also carried out.

2.1 Working principle

Particle image velocimetry is a non intrusive anemometric technique that allows to compute the whole velocity field within the investigated area when opportunely illuminated, imaged and seeded. PIV generally requires three different subsystems in order to work properly: a light source that provides a uniform illumination of the investigated volume, a camera system that allows to capture two or more frames at short temporal distance and a system that allows to release within the flow tracing particles. The captured images are subdivided into smaller areas, called interrogation windows. In each window, the most probable displacement is determined

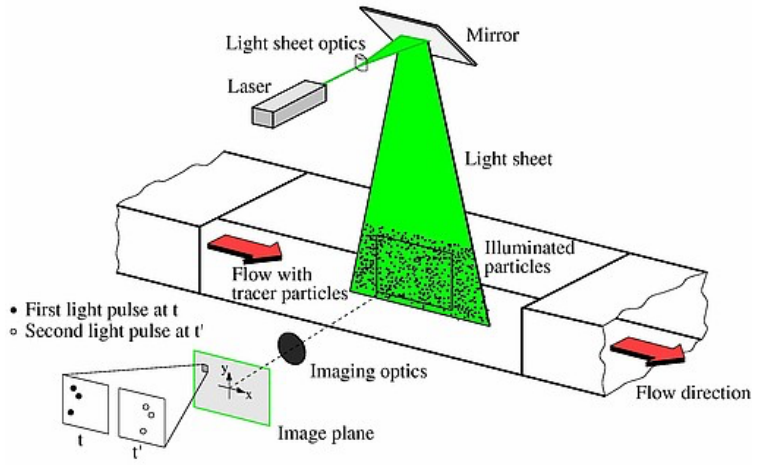

Figure 2.1: Schematic representation of a classical PIV system (from Raffel et al., 1997).

using an auto-correlation algorithm in the case of double exposure images (Adrian and Yao, 1984) or the cross-correlation operation in the case of single exposure images (Willert and Gharib, 1991). Once the planar displacements Δx and Δy are measured, the planar velocity components can be expressed as:

$$\begin{Bmatrix} u \\ v \end{Bmatrix} = \frac{M_0}{\Delta t} \begin{Bmatrix} \Delta x \\ \Delta y \end{Bmatrix} \tag{2.1}$$

where u, v are representative of the two components of the velocity vector in the target plane respectively; Δt is the temporal separation between the two frames; this value should be accurately set in order to obtain a particles' displacement onto the image plane of about 8-12 pixels. M_0 is representative of the magnification factor, calculated as the ratio between z_0, distance between the lens and the image plane and Z_0, distance between the lens and the target plane. Whereas this value can be assumed to be constant across the whole image in the case of planar PIV experiments, in the case of volumetric experiments the cameras are generally tilted with

respect to the target plane. This leads to the fact that M_0 value is not constant within the volume.

2.2 Experimental details

2.2.1 Illumination and camera system

Due to necessity of collimated intense pulses of light at short temporal distance, only pulsed lasers are usually employed in PIV applications. Depending on the application (low or high acquisition frequency) the laser can be either Nd:YAG or a Nd:YLF. The former is generally used for low frequency purposes (up to 15 Hz) and it is characterized by a high energy content per pulse, ranging from 100 up to 800 $mJ/pulse$; the working wavelength of this kind of lasers is 532 nm. The latter has generally lower energy (up to 30 $mJ/pulse$) but very high frequency (up to 10 KHz), with a working wavelength of 526 nm. Since the light intensity decreases linearly with the thickness of the illuminated volume, when performing volumetric experiments the demand in terms of laser energy becomes larger and larger. In order to enlarge the maximum illuminated region, Ghaemi and Scarano (2010) proposed the use of a multi-pass system: the laser beam is reflected different times within the volume, leading to a larger light intensity for fixed illuminated region thickness (commonly referred to as fluence) or for fixed fluence a larger illuminated region.

The sequences of tracer particles are collected using cameras with a charged-coupled device (CCD) or complementary metal-oxide-semiconductor (CMOS) sensor. The dimensions of the sensor, at this stage of technology, range from 1 MPix up to 16 MPix with the acquisition frequency that need to be clearly aligned to that of the light source aforementioned.

2.2.2 Seeding particles

The choice of the proper seeding particles is strongly dependent on the working fluid, since it is assumed that the tracers are capable of accurately

follow the flow motion without perturbing it. An indicator of the accuracy of the particles in following the flow is given by the particle relaxation time (τ_s, see Raffel et al., 1997):

$$\tau_s = d_p^2\Big(\frac{\rho_p}{18\mu}\Big) \tag{2.2}$$

being d_p and ρ_p the particles' dimension and density respectively and μ the working fluid dynamic viscosity. A decrease in either the particle dimension or the particle density leads to a reduction in τ_s. The smaller the relaxation time, the better is the tendency of the particles to follow accurately the flow. On the other hand, working with a fluid with larger dynamic viscosity, allows the use of larger particles.

2.2.3 Imaging

The imaging is another key element when performing PIV experiments. When illuminated by the laser light, the intensity collected onto the camera sensor will be made of two contributions: a first associated to the particle geometry (i.e. its actual size) and a second associated to the diffraction of the light scattered in all the direction by the illuminated particle. This turns into the following relation for the particle diameter on the sensor (from Adrian, 1991):

$$d_\tau = \sqrt{d_{geom}^2 + d_{diff}^2} = \sqrt{(M_0 d_p)^2 + (2.44 f_\#(1+M_0)\lambda)^2} \tag{2.3}$$

where d_{geom} is the particle dimension as imaged onto the sensor plane, d_{diff} is the contribution associated to the diffraction model, $f_\#$ is the ratio between the focal length and the aperture diameter (this equality rigorously holds only in the thin-lens approximation) and λ is the wavelength of the illuminating source. The particle dimension d_τ should be as small as possible to reduce the uncertainties in the displacement determination; however, there are several known problems that arise when the particle dimension is smaller than 2 pixels, as the peak-locking (the bias of

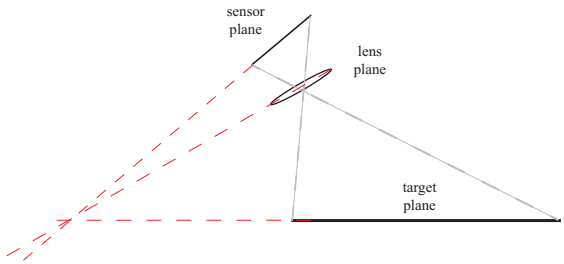

Figure 2.2: Schematic representation of the Scheimpflug condition.

the correlation peak towards integer values, Westerweel, 1997). It is then common rule to set the imaging system in order to have a d_τ larger than 2 pixels and smaller than 5 pixels.

Especially in three dimensional experiments, an element that plays a key-role is the depth of field dz, which represents the distance orthogonal to the object plane over which the blur spot size does not exceed a specified spot size. The depth of field dz is defined as:

$$dz = 2f_{\#}d_{diff}\left(\frac{1+M_0}{M_0^2}\right) = 4.88f_{\#}^2\lambda\frac{(1+M_0)^2}{M_0^2} \tag{2.4}$$

It is important to consider that, when performing volumetric PIV experiments, the cameras must be tilted with respect to the object plane. This actually produces a reduction of the effective depth of field of the camera, as a function of the Euler angles between the cameras and the object plane. As a consequence, one can either enlarge the depth of field (for example increasing $f_{\#}$ but involving a reduction of the collected scattered intensity) or operate the cameras in *Scheimpflug* arrangement. The Scheimpflug condition is satisfied when, rotating the lenses with respect to the sensor, the focal plane, the lens plane and the target plane will converge into one straight line (see Figure 2.2). The Scheimpflug condition is satisfied by using a specialized lens mount, which can be either bought from manufacturers or opportunely designed.

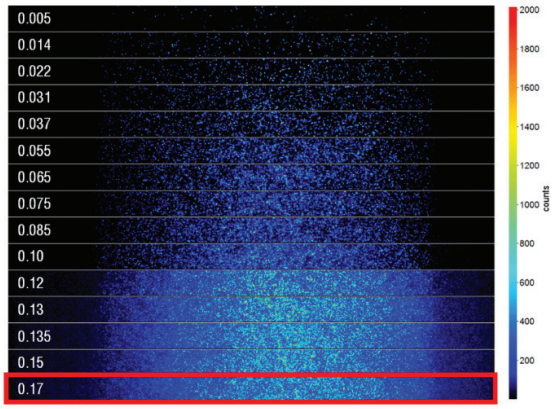

Figure 2.3: Samples of particle images at various seeding density in volumetric experiments (from Michaelis et al., 2010).

2.2.4 Seeding density

The choice of a correct seeding density is of paramount importance in order to perform a proper PIV experiment. Depending on the desired spatial resolution, the amount of seeding that should be used for an experiment may strongly vary. It is commonly considered as a good value to have about 10 particles per interrogation window in the case of planar experiments. This value is generally relaxed to 5-7 particles per interrogation volume in the case of volumetric experiments, because the particles do not leave the investigated illuminated region. The parameter that is most commonly looked at to properly set the seeding density is the particle image density, expressed in particle per pixel (*ppp* [1]). The *ppp* in the case of planar PIV experiments is generally pushed up to values equal to 0.15, in order to stress the maximum achievable spatial resolution. On the other hand, the *ppp* strongly affects the reconstruction quality in the

[1] It should be explicitly noticed that rigorously the parameter that affect the seeding density is the source density N_S, defined as $N_S = ppp \cdot \frac{\pi}{4}(d_\tau/\Delta_{pix})^2$, with Δ_{pix} indicating the pixel size. However, its computation is not as straightforward as the *ppp*.

case of volumetric PIV experiments (Elsinga et al., 2006, see paragraph 2.3.2). In Figure 2.3, Michaelis et al. (2010) carried out a series of experiments at progressively increasing seeding density. It is clear how, for *ppp* values larger than 0.12 it is not possible to distinguish the particles from each other. This is not a favourable condition both for the self calibration and volume reconstruction standpoint (see paragraph 2.3.1 and 2.3.2). A well accepted value is 0.05, although recently, exploiting the features of time resolved particle tracking velocimetry conjugated to the Shake-the-box technique (STB, Schanz et al., 2013) or to the sequential motion-tracking enhanced (SMTE, Lynch and Scarano, 2015) this limit has been pushed well-beyond 0.1 also in the case of volumetric experiments.

2.3 3D Technique: Tomo-PIV

The main field of application of PIV is the study of turbulent flows. As it is well known, a turbulent flow is inherently three dimensional, thus often making very complex the understanding of the flow field features from only four components of the velocity gradient tensor. This element pushed the development of more complex techniques, whose aim is to fully determine the flow field in a volume and not only in a plane. A rather recent and reliable technique is the tomographic PIV (Tomo-PIV, Elsinga et al., 2006). Tomo-PIV requires a more complex experimental facility than planar PIV, although the basic idea is the same. The illuminating source, which is often a laser, although other solutions can be also used as for example LED, is generally shaped in a volume, whose thickness strongly affects the quality of the experiment. The sequences of tracing particles are collected using a larger number of independent views (i.e. cameras) than the planar case; a typical Tomo-PIV experiment requires a set of 4 cameras disposed in Scheimpflug arrangement (see paragraph 2.2.3), although there are examples in the literature of much more complex systems (for example the 12 cameras system proposed by Lynch and Scarano, 2014). In the following paragraphs, a brief review on the necessary steps to perform a

tomographic PIV experiment will be carried out.

2.3.1 Calibration and self-calibration procedure

The necessity of defining a common reference system for all the cameras used in the experiment, requires an *in-situ* optical calibration. The calibration procedure is generally based onto two different steps: a first one where the optical calibration is carried out, i.e. a common reference frame is defined for the set of cameras using an *ad hoc* calibration target; a second step, the self-calibration (Wieneke, 2008), where the seeding particles are used to further correct the positioning of the cameras.

The optical calibration is often performed moving a calibration target (with known characteristics as markers size and spacing) through the volume and capturing images from all the cameras at different positions. An interpolation model is then used to match the position of the markers at all the locations across the measurement volume. The most commonly used models are those proposed by Tsai (1987) and Soloff et al. (1997). The former is particularly appealing due to its simplicity: it consists in considering the line of sights of the cameras as straight lines and also gives to the user the calibration parameters in terms of physical quantities as the Euler angles of the camera, the focal length of the objective lens and other geometrical parameters. However, this model is particularly sensitive to the lens distortions, especially when varying across the volume. The method proposed by Soloff et al. (1997) is instead based on interpolating the markers map with a 3rd order polynomial function in x, y and a second order polynomial in the z direction. Although generally this method leads to lower calibration errors, the pinhole method proposed by Tsai (1987) is often more reliable due to its simplicity and to the fact that the user can actually check with physical arguments the calibration constants.

The necessity of a high accuracy in the determination of the relative positioning of the camera system when performing volumetric experiments, requires the introduction of a further step to correct possible misalign-

ments between the cameras. It often occurs that, as a consequence of the experimental conditions, small perturbations to the relative angles between the cameras could be introduced (Avallone et al., 2014). The volume self-calibration (Wieneke, 2008) is a technique that, using the triangulation of the seeding particles between the images acquired by the camera system, allows a sensitive reduction of the calibration error. The schematic work-flow (Figure 2.4) is the following: a set of candidate particles are identified for the first camera of the system fixing an opportune threshold. Second, the forward-projection of each particle position through the volume is computed and then back-projected onto the second camera of the system. This forms an epipolar line (shadowed region in Figure 2.4). A search radius is established (indicated as ϵ_s) about this line and all particles detected within this region are flagged as potential marching candidates (after two cameras, the epipolar line is an epipolar point). The procedure continues for all cameras of the system to reduce the number of candidate matches. If a match is found in all camera images, the particle is considered a true match and least-squares triangulation estimates the particle position in the reference frame established with the optical calibration (referred to as world coordinates). Back-projection of this position to all cameras and comparison to the particle images yields a disparity for each camera at the world coordinates of the particle.

2.3.2 Volume reconstruction

Tomography deals with the reconstruction of a $m-$dimensional object from a set of $(m-1)-$dimensional projections. A projection is defined as a line integral of the object to be reconstructed along a viewing direction. This problem is known also in other applications field, as bio-engineering. It is indeed the same working principle of the X-ray computed tomography (CT) but with a strong and paramount difference. In the CT scan the patient is generally asked to be at rest and numerous views of its body (the whole or only a part of it) is imaged by means of rotating cameras,

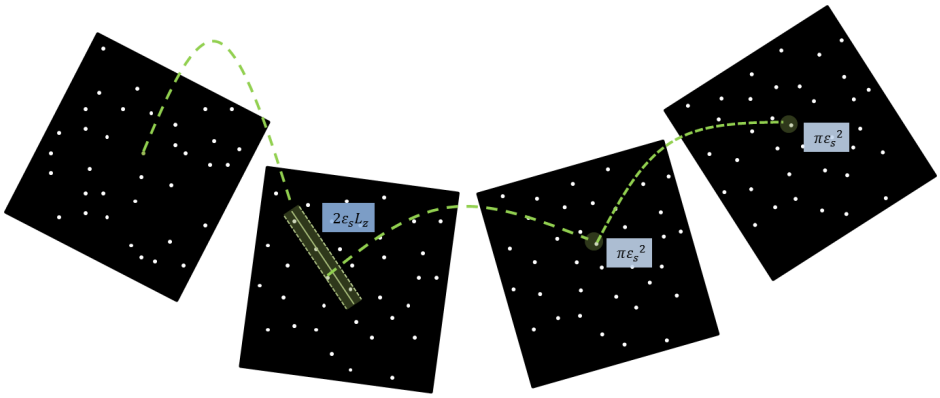

Figure 2.4: Schematic of the self-calibration procedure (from Discetti and Astarita, 2014).

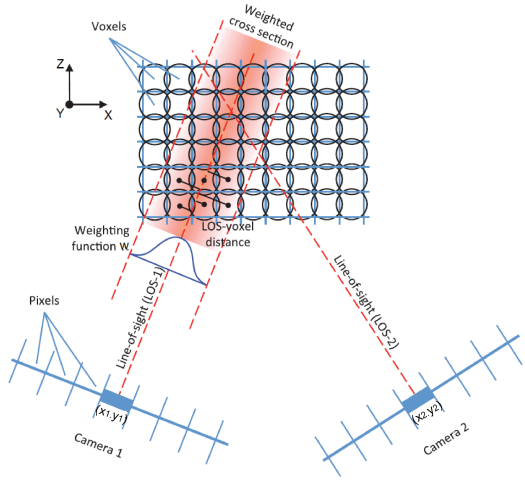

Figure 2.5: Schematic representation of the voxel distribution and the camera system. In the shaded region, the weighting functions are non-zero, thus those voxels participate in the intensity recorded on the camera array (from Scarano, 2013).

thus leading to a significantly redundant quantity of information; for PIV applications, the complexity is sensitively higher. More specifically, in tomographic PIV the object is the 3D distribution of the light scattered by the tracer particles $E(x, y, z)$ (where x, y, z are the spatial coordinates in a 3D reference system), while the recorded intensity values on the cameras constitute the set of projections $I(X, Y)$ (where X, Y are the coordinates in the 2D camera reference system). In the case of the iterative algebraic reconstruction techniques (Herman and Lent, 1976), the object is discretized as a 3D array of voxels. The line integrals of the intensity along the lines of sight are discretized as a weighted sum of the voxel intensities

$$I(X_i, Y_i) = \sum_{j=1}^{N_{vox}} w_{i,j} E_j \tag{2.5}$$

The subscript i and j indicate the $i-th$ pixel and the $j-th$ voxel, respectively; E_j is representative of the voxel intensity having coordinates x_j, y_j, z_j; N_{pix} and N_{vox} are the total number of pixels and voxels; $w_{i,j}$ is a weighting coefficient, determining the influence of the intensity of the $j-th$ voxel on the intensity recorded on the $i-th$ pixel (see Figure 2.5). The value of $w_{i,j}$ ranges from 0 to 1 and is calculated as the volumetric fraction of voxel j intersected by the line of sight of pixel i, modelled, for example, as a cylinder having cross section equal to the pixel area. The equation 2.5 results in a system of N_{pix} linear equations with N_{vox} unknowns. The problem is under determined and ill-posed; some additional constraints can consistently reduce the dimension of the space of the solutions. The solution of the system represented in equation 2.5 can be approximated via different methods. In particular, two classes of algebraic schemes are distinguished: additive and multiplicative. The benchmark methods belonging to these two classes are ART (algebraic reconstruction technique) and MART (multiplicative ART). The former converge to the minimum norm solution, whilst the latter is demonstrated to maximize the entropy value (Gordon and Herman, 1971). At each iteration k, the MART scheme

updates the intensity field according to the following relation:

$$E_j^{k+1}(x,y,z) = E_j^k(x,y,z)\left(\frac{I(X_i,Y_i)}{\sum_j w_{i,j}E_j^k}\right)^{\mu w_{i,j}} \tag{2.6}$$

where μ is a relaxation parameter that should be set to a value smaller than 1 for stability. In order to have a rather accurate reconstruction using MART, 5 iterations can be sufficient (Elsinga et al., 2006). Besides MART, which can be considered as a row-action algorithm, operating on each single row of equation 2.6 at a time, a different approach is given when updating the whole intensity field simultaneously. The sMART (simultaneous-MART, Mishra et al., 1999) updating equation is:

$$E_j^{k+1}(x,y,z) = E_j^k(x,y,z)\prod_c^{N_c}\left[\left(\frac{I(X_i,Y_i)}{\sum_j w_{i,j}E_j^k}\right)^{\mu w_{i,j}}\right]^{1/N_c} \tag{2.7}$$

where c is the camera index and N_c is the total number of cameras. It must be considered that generally for convergence, sMART requires a larger number of iterations than MART.

The reconstruction quality is affected by many artefacts arising from the under determination of the system reported in equation 2.5. These artefacts in the tomographic reconstruction process are named ghost particles (Maas et al., 1993). They represent intensity blobs forming at the intersection of line of sight carrying non-zero values, but not corresponding to the position of actual particles. The mechanism of the ghost particles formation is sketched in Figure 2.6 for the simplified case of a 2D slice reconstructed by two 1D cameras. Obviously the larger is the number of particles, the larger is the number of ambiguities in the reconstruction (Discetti, 2013); furthermore, the thicker is the volume (Δz_0), the higher is the number of positions that each true particle may occupy into the reconstructed volume, and accordingly the higher is the probability of ghost particles occurrence. An estimate of the number of ghost particles for a

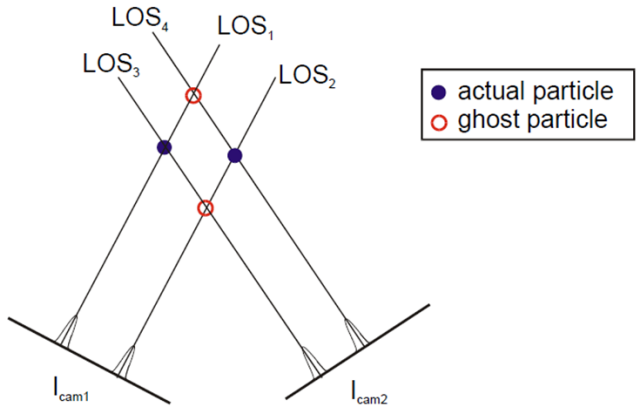

Figure 2.6: Mechanism of formation of ghost particles. a) two particles imaged by two cameras lead potentially to two ghost particles (this is not exactly true in 3D, as the lines of sight can be non-coplanar. b-c-d) three possible solutions of the reconstruction problem (Elsinga et al., 2006).

general N_{cam} camera system is proposed by Discetti (2013).

$$\frac{N_g^{N_{cam}}}{N_p} = \frac{4}{\pi d_\tau} N_S^{N_{cam}-1} \Delta z_0 M \tag{2.8}$$

The number of ghost particles may be also of the same order of that of the true particles. However, as the number of MART/sMART iteration increases, the difference in intensity between real and ghost particles increases as well. A practical criterion to assess the goodness of the reconstruction is associated to the ratio between the reconstructed particles' intensity level and the ghost particles' intensity level. The SNR should be always larger than 2 in order to achieve a good reconstruction (Scarano, 2013). The effect of ghost particles on the velocity field is to modulate the velocity gradients, particularly those along the viewing direction. However, if the real particles move enough between the two exposures, the ghost particles pattern becomes decorrelated, and the correlation signal and displacement estimate are the product of only the real particles.

Ghost particles can be then considered as one of the main problems that affect the Tomo-PIV. Different techniques attempted to reduce their effect by detecting and removing them, without paying in terms of spatial resolution. One of the most efficient is based on the coherence of a particle field between snapshots. The Motion Tracking Enhanced MART (MTE-MART, Novara et al., 2010) improves reconstruction accuracy by using the local velocity field to introduce information on the coherence of the particle field between times to present an improved initial guess to the MART procedure. As the velocity field is not known a priori, the method is iterative and has as its primary disadvantage a significantly greater computational cost. A further development of this technique is provided by the sequential MTE (SMTE, Lynch and Scarano, 2015), which takes advantage of the time resolved data in order to enhance the performances of the classic MTE-MART also in terms of computational cost. The method is a sequential algorithm that produces a time-marching estimation of the object intensity field based on an enhanced guess, which is built upon the object reconstructed at the previous time instant. The method is inherently thought for time resolved data as it becomes effective after 5-10 snapshots.

2.3.3 3D CORRELATION

Once the volumes representative of the first and second exposure are reconstructed using one algorithm as reported in the previous paragraph, the velocity field is estimated using the three-dimensional cross correlation. However, the operation is particularly onerous from the computational point of view. Discetti and Astarita (2012a) proposed the use of an efficient algorithm that allowed to significantly reduce the number of calculations taking into account the overlapping windows. Furthermore, the use of sparse direct cross-correlations can consistently reduce the computational cost since the number of non-zero voxels is generally a quite small percentage of the whole volume.

CHAPTER 3

IR Thermography for convective heat transfer measurements

IR Thermography represents an excellent tool to perform non-intrusive investigations of the thermal field. This makes it particularly appealing for several application; amongst the other we may recall the non-destructive inspections of materials, the presence of leakages, thermal bridges or humidity in buildings walls. However, this chapter will focus on the use of IR Thermography for fluid dynamics applications. At the beginning some theoretical aspects of the energy transport that occurs by means of radiation will be recalled . Afterwards the constitutive elements of an IR scanner will be presented. Finally, the application of such devices for the measurement of the convective heat flux in fluid dynamics will be discussed. For a more detailed discussion, one may refer to specialized textbooks as Astarita and Carlomagno (2013).

3.1 Theoretical Background

Heat transfer by radiation is an energy transport mechanism that occurs by means of electromagnetic waves. Contrary to the case of heat

conduction, energy can also be transmitted by thermal radiation in the absence of a medium. The presence of a medium between two bodies that are transferring energy to each other, may cause or not the loss of some amount of this energy. In particular, a certain amount of the transferred energy may be absorbed or reflected; in this case the medium will be referred to as *partially transparent*. However, it may also occur the case where the medium does not downgrade the energy transmitted between the bodies, thus being called *fully transparent*.

Every body in nature that is at an absolute temperature above $0K$ emits energy by means of electromagnetic waves. The amount of thermal radiation which is absorbed or emitted, as well as its propagation, depends not only on the nature of the material and surface finish, but also on its thermodynamic state and on the specific wavelength of the considered electromagnetic wave.

The wavelength λ is linked to the frequency of the wave ν by its speed of propagation c through the medium:

$$\lambda = \frac{c}{\nu} = \frac{c_0}{\nu n} \tag{3.1}$$

where c_0 is the speed of propagation in vacuum (independent on λ, $2.998 \cdot 10^8 m/s$) and n is the index of refraction of the medium, which generally is a function of the wavelength.

The entire electromagnetic spectrum is divided into a number of wavelengths intervals, called *spectral bands*, and extends from very small wavelengths values ($\lambda \to 0$) to extremely large ones ($\lambda \to \infty$), as reported in Figure 3.1. The thermal radiation band is conventionally defined as a portion of the complete spectrum, between $0.1\mu m$ and $1000\mu m$, including part of the ultraviolet and all of the visible and IR bands.

At ambient temperature, the largest amount of energy emitted by a body is within the Infrared band. This band is further subdivided into four subcategories: near infrared ($0.76 - 3\mu m$), middle infrared ($3 - 6\mu m$), far infrared ($6 - 15\mu m$) and extreme infrared ($15 - 1000\mu m$).

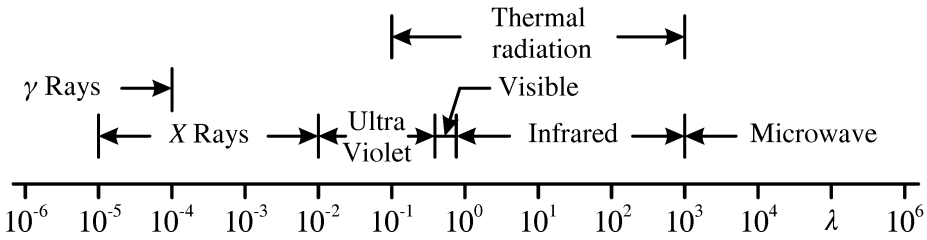

Figure 3.1: Electromagnetic spectrum (from Astarita and Carlomagno, 2013).

The largest number of currently used IR camera for thermo-fluid dynamics applications are sensitive in the middle (MWIR) or the long wavelength (LWIR). However, it must be explicitly noted that, due to high atmospheric absorption between $\lambda = 5\mu m$ and $\lambda = 7.5\mu m$, there are no IR camera detectors working in this range of wavelengths.

However there are several solids and liquids that are opaque (non completely transparent to the IR radiation), thus a portion of the incident non-reflected radiation is absorbed. Generally speaking an opaque body at a specified temperature emits from its surface in many directions and in a wide range of wavelengths. Moreover, the energy emitted by radiation depends on the material nature and its surface characteristics, including as already mentioned the surface finish. It is then useful to introduce a conceptual body, called *black body*, which can be considered as a perfect emitter and absorber of radiation. It is then able to absorb all of the incident radiation, regardless of its wavelength and direction; moreover, the black body for a fixed temperature and wavelength, emits uniformly in all the directions the maximum amount of radiation. A good approximation of a black body is given by an isothermal cavity with a very small aperture; the thermal radiation that enters within the cavity before leaving it undergoes a series of reflections onto the surfaces of the cavity itself. As a consequence,only a small amount of the total thermal radiation will leave the cavity. In a similar fashion, the radiation emitted by the internal surface of the cavity will experience a series of reflection thus producing a

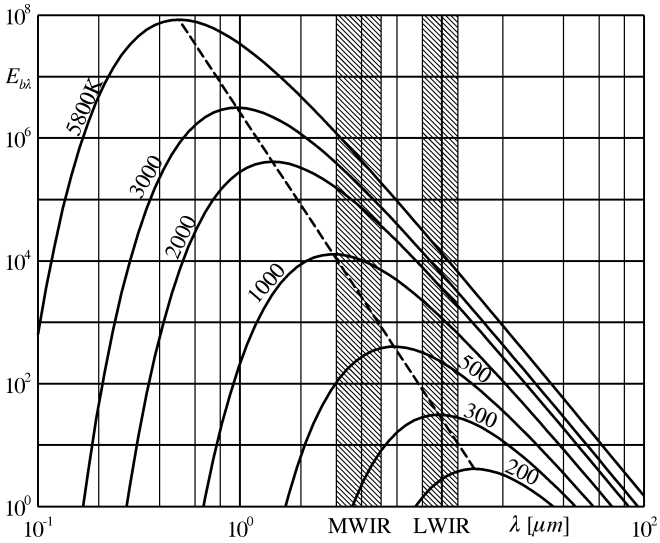

Figure 3.2: Spectral hemispherical black body emissive power ($W/m^2\mu m$) in vacuum for several absolute temperature (K) values as a function of the wavelength (from Astarita and Carlomagno, 2013).

maximum emission in all directions.

The law that permits to evaluate the energy flux per wavelength (i.e. the spectral power) which is emitted by a black body in vacuum is Planck's law of radiation:

$$E_{b\lambda}(\lambda, T) = \frac{C_1}{\lambda^5(e^{C_2/(\lambda T)} - 1)} \tag{3.2}$$

where T is the absolute body temperature and $C_1 = 3.742 \cdot 10^{-6} W m^2$ and $C_2 = 1.439 \cdot 10^{-2} K m$ are the first and second radiation constants.

Equation 3.2 is plotted as a function of the wavelength in Figure 3.2. The maximum in the spectral power increases as a function of the body absolute temperature; furthermore, there is an appreciable shift of its location towards smaller wavelengths as the absolute temperature increases. The locus of the points that individuate the maxima of Planck's equation as a function of the absolute temperature (dashed line in Figure 3.2) is

given by Wien's law:

$$\lambda_{max} T = 2898(\mu K) \tag{3.3}$$

Equation 3.3 enables one to find the wavelength λ_{max} at which a black body emits its maximum spectral emissive power as a function of its temperature.

Integrating Planck's law (eq. 3.2) over the whole spectrum, the Stefan-Boltzmann law can be obtained. This law permits to calculate the total black body hemispherical emissive power E_b:

$$E_b = \int_0^\infty E_{b\lambda}(\lambda, T)\, \mathrm{d}\lambda = \sigma T^4 \tag{3.4}$$

where $\sigma = 5.6710^{-8} W/(m^2 K^4)$ is the Stefan-Boltzmann constant.

Real bodies radiation is quite different from that of black bodies. Indeed, both emitted and absorbed radiations of a black body are upper limits for real bodies. As shown in Figure 3.3, the incident radiation is only partially absorbed by the body (schematically represented as a slab in Figure 3.3); the remaining part can be transmitted through the slab and/or reflected by the slab. By indicating with α_r the amount of incoming radiation absorbed by the slab, with ρ_r the radiation reflected by the slab and τ_r the portion transmitted through the medium, from energy conservation it stands that:

$$\alpha_r + \rho_r + \tau_r = 1 \tag{3.5}$$

being α_r, ρ_r and τ_r the absorptivity (absorptance), the reflectivity (reflectance) and transmissivity (transmittance) coefficients of the body, respectively. These coefficients are clearly non-negative and lower than one. For a black body, $\alpha_r = 1$ and as a consequence, $\rho_r = \tau_r = 0$. For an opaque body, $\alpha_r = 1 - \rho_r$.

Both on a total and spectral basis, a real body will always emit a fraction of the radiation emitted by a black body at the same temperature.

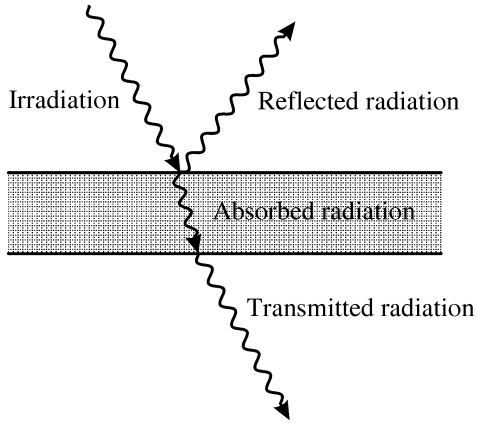

Figure 3.3: Reflection, absorption and transmission of the irradiation in a slab (from Astarita and Carlomagno, 2013).

It is helpful to introduce a coefficient that is representative of this fraction; the spectral hemispherical emissivity coefficient ϵ_λ is defined as:

$$\epsilon_\lambda = \frac{E_\lambda(\lambda, T)}{E_{b\lambda}(\lambda, T)} \tag{3.6}$$

In a similar fashion, the total hemispherical emissivity coefficient is defined as:

$$\epsilon = \frac{E(T)}{E_b(T)} \tag{3.7}$$

The emissivity coefficient is in general also a function of the angle between the emitted radiation and the emitting surface. When this dependence is not considered, the body is called a diffuse emitter. The spectral emissivity of a body is also dependent on the wavelength of the emitted radiation, the emitting body material and the conditions of its surface. A material whose spectral emissivity is independent on the λ values is called grey body. Although a proper grey body does not exist, it often occurs that a real surface may have a quite constant emissivity over the used IR detector band, thus allowing us to consider the grey hypothesis as satisfied.

For diffuse emission, Kirchhoff's law states that the spectral emissivity is equal to the spectral absorptivity coefficient $\epsilon_\lambda = \alpha_\lambda$. As a consequence, for an opaque body, as those commonly used in IR Thermography, it stands that:

$$\epsilon_\lambda + \rho_{r\lambda} = 1 \tag{3.8}$$

This leads to the consideration that bodies with low emissivity not only emit less energy but also reflect a large amount of the radiation impinging on them.

3.2 IR Scanner

A schematic representation of the components required for an infrared scanning radiometer is reported in Figure 3.4. The amount of thermal radiation that enters within the scanner is collected by an optical system and sent into a temperature detector that is sensitive to the selected IR band. The electric signal generated by the detector is acquired by a frame grabber and is processed by a dedicated electronic board in order to obtain a temperature map of the scanned scene. The main parameters that determine the performances of an IR scanner are reported in the following sections. In particular: the thermal sensitivity, the spatial resolution, the acquisition frequency as well as temperature and dynamic ranges.

3.2.1 Thermal sensitivity

Thermal sensitivity is generally expressed in terms of mean *noise equivalent thermal sensitivity* (NETD), which is defined as the time standard deviation of the random background noise averaged over all pixels of a black body scene (Levesque et al., 2005). The NETD is a function of the used black body temperature and the manufacturer provides it at ambient temperature in terms of mK. At a temperature of 20^oC a typical NETD value for an uncooled IR scanner is about $100mK$ whilst for cooled detectors this value can be reduced down to $10mK$.

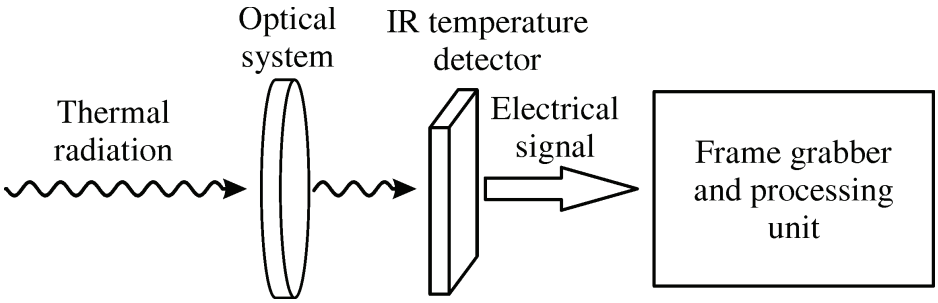

Figure 3.4: The main elements that characterize an IR scanner (from Astarita and Carlomagno, 2013).

The thermal sensitivity is a decreasing function of the spatial frequency of the input thermal signal; for this reason, it may be also expressed in terms of *minimum resolvable temperature difference* (MRTD), which is the minimal temperature difference of a 4-bar target detectable by the operator. A similar index is the *minimum detectable temperature difference* where a series of circular targets are used instead of the 4-bar one. Both indices are equivalent to the NETD when the input thermal signal is characterized by low spatial frequency.

3.2.2 Spatial resolution

The spatial resolution characterizes the capability of an infrared scanner to resolve temperature differences between points placed at relatively small distances.

A coarse definition of the spatial resolution is based on the instantaneous field of view (IFOV) defined as the ratio of the detector size width over the lens focal length and is normally expressed in *mrad*. However, this is only an ideal design parameter and does not fully describe the performance of the IR scanner.

A more rigorous definition of the spatial resolution of an IR scanner is given in terms of the scanner Modulation Transfer Function (MTF), which is the magnitude of the normalized complete Optical Transfer Func-

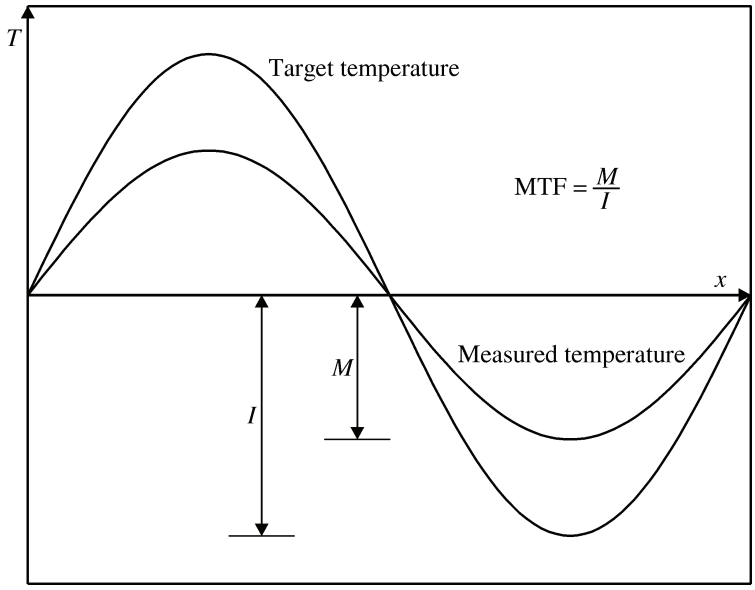

Figure 3.5: Modulation effect (from Astarita and Carlomagno, 2013).

tion (OTF). A physical meaning to the definition of spatial resolution in terms of MTF can be given considering a sinusoidal temperature signal of amplitude I as represented in Figure 3.5 that is an only function of the x coordinate. The measured temperature signal exhibits a smaller amplitude M, which is generally referred to as modulation. The modulation, is generally a decreasing function of the signal spatial frequency.

3.2.3 Acquisition frequency

The choice of the acquisition frequency is an important parameter for the study of transient phenomena in thermo-fluid dynamics and is basically dependent on the response time of the thermal detector. It is generally expressed in number of full frames acquired per second (thus a frequency, Hz). This value may vary in a quite wide range: from tens of Hz up to dozens of kHz. To date, an advanced IR camera is capable of acquire im-

ages of 640x512 pixels at a frame rate of 62 kHz and even exceed this limit when cropping the sensor dimension. The maximum acquisition frequency is also limited by the minimum integration time needed by a detector pixel to measure correctly the temperature of the target object. This time is reasonably inversely proportional to the measured temperature so that, for low object temperatures, the maximum acquisition frequency could be smaller than at higher ones.

3.2.4 Temperature and dynamic ranges

The temperature range that can usually be measured with an IR scanner spans from -20 to 1500°C.

The dynamic range is expressed in terms of the number of digital intensity levels the individual pixels is made of. The latest generation of cameras typically provide 14 bits A/D conversion, although with some manipulations some products can achieve also 16 bits artificially extending the dynamic range.

In any case, the temperature range is clearly limited at relatively small temperatures because of the extremely small radiative flux that impinges on the detector. Besides, since the radiative flux is a non linear function of the temperature, when measuring large temperatures, the detector integration time must be significantly reduced or the incident radiation filtered, thus leading to a loss in the accuracy when simultaneously measuring lower temperatures.

3.3 IR scanner radiometric calibration

The output signal of an IR scanner depends on the radiation energy that impinges on it and a calibration function is needed to convert the produced electrical signal into the real viewed object (target) temperature. Most modern cameras are already calibrated so that the system software is able to directly calculate the temperature; the user does not receive the

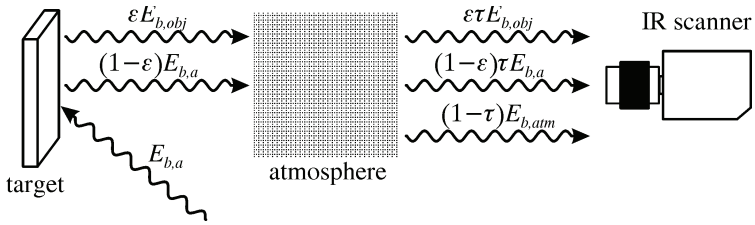

Figure 3.6: Schematic representation of the radiation detected by the IR scanner (from Astarita and Carlomagno, 2013).

raw signal as an output but rather an exhaustive 2D map of temperatures.

Nevertheless, often a more accurate calibration, or a recalibration (e.g. in a different temperature range, smaller or larger) of the IR scanner is required. As shown in Figure 3.6 only a fraction of the radiation flux collected by the IR scanner is actually emitted by the target. Indeed, two more contributions must be taken into account: one associated to the radiation emitted by the ambient and another to the the atmosphere emission. Furthermore, it must be considered that the atmosphere itself represents a medium, thus constituting an attenuation for the radiation that reaches the scanner. Keeping in mind these considerations, if the emitting body is at a temperature T_{obj} it will emit only a fraction ϵ_t of the radiation a black body would emit at the same temperature. If the transmissivity coefficient of the atmosphere is τ_r the radiation emitted by the object that reaches the IR scanner detector will be $\tau_r \epsilon_t T_{obj}$.

When performing IR Thermography experiments, every effort must be made to avoid any fluctuations in the ambient temperature, in order to consider the ambient at a constant temperature T_a. Since the temperature is constant and the extension of the ambient is much larger than that of the emitting body, it is reasonable to assume the ambient as a black body, thus the emitted radiation is $E_{b,a}$.

The target is assumed as opaque, thus the reflectivity coefficient can be evaluated as $1 - \epsilon_t$ and, taking also into account the absorption of the atmosphere, the radiation emitted by the surrounding ambient environ-

ment reflected by the target and finally collected by the detector is equal to $(1-\epsilon_t)\tau_r E_{b,a}$.

In a similar fashion, supposing that the atmosphere is at a constant temperature T_{atm} and its emissivity is $(1-\tau_r)$, the radiation collected by the IR scanner detector will be $(1-\tau_r)E_{b,atm}$.

It is then possible to express the total radiation collected by the IR scanner detector:

$$E_t = \tau_r \epsilon_t E_{obj} + (1-\epsilon_t)\tau_r E_{b,a} + (1-\tau_r)E_{b,atm} \tag{3.9}$$

The output signal of the IR detector U, which could be either a current I or a voltage V can be considered as linearly dependent on E_t:

$$U = \tau_r \epsilon_t U_{obj} + (1-\epsilon_t)\tau_r U_{b,a} + (1-\tau_r)U_{b,atm} \tag{3.10}$$

The output signals $U, U_{obj}, U_{b,a}, U_{b,atm}$ can be correctly approximated by a function similar to Planck's law, being the IR bands quite narrow (see paragraph 3.1).

$$U = \tau_r \epsilon_t \frac{R}{e^{B/T_{obj}} - F} + (1-\epsilon_t)\tau_r \frac{R}{e^{B/T_a} - F} + (1-\tau_r)\frac{R}{e^{B/T_{atm}} - F} \tag{3.11}$$

The three calibration constants $R(V \text{ or } A)$, $B(K)$, $F(\text{dimensionless})$ mainly depend on the integration time and on the IR scanner properties. In particular, comparing equation 3.11 to equation 3.2 it is possible to infer that B is inversely dependent on the wavelength and F should be equal to 1. A different value can be used to compensate non-linearities in the IR scanner. R is mainly dependent on the IR scanner properties and on the wavelength of the detected band. Solving equation 3.11 for T_{obj}:

$$T_{obj} = \frac{B}{\log\left(\frac{\epsilon_t \tau_r R}{U-(1-\epsilon_t)\tau_r U_a-(1-\tau_r)U_{atm}} + F\right)} \tag{3.12}$$

When performing measurements at relatively short distances, normally

the atmospheric transmissivity coefficient can be practically put equal to 1, therefore, the terms associated with atmospheric absorption and emission may be neglected. For the sake of simplicity, this hypothesis is also assumed in the following. If a semi-transparent window (or a mirror) is placed in the optical path, other terms, similar to that relative to the atmospheric absorption, should be included in the previous equations and both the optical characteristics of the window (mirror) and its temperature should be known.

To determine the calibration constants, a black body is normally used as reference so that the emissivity is equal to 1 and also the spurious reflections can be neglected. Moreover, as to consider $\tau_r = 1$, the black body should be put at relatively short distance from the IR scanner. Equation 3.12 becomes:

$$T_{obj} = \frac{B}{\left(\frac{R}{U} + F\right)} \tag{3.13}$$

By changing the black body temperature in the range of interest, it is possible to record the output signal from the IR scanner and then the calibration constants can be found by making a non-linear best fit of the n independent measurement points. In particular, by indicating with T_b the black body temperature, measured with a high-accuracy thermometer, the calibration constants are evaluated by varying R, B and F in order to minimize, with a standard optimization algorithm, the functional:

$$\sum_{i=1}^{n}\left(T_b^i - T_{obj}^i\right)^2 \tag{3.14}$$

The calibration range should be chosen such that it is slightly larger than the one of interest for the experiments.

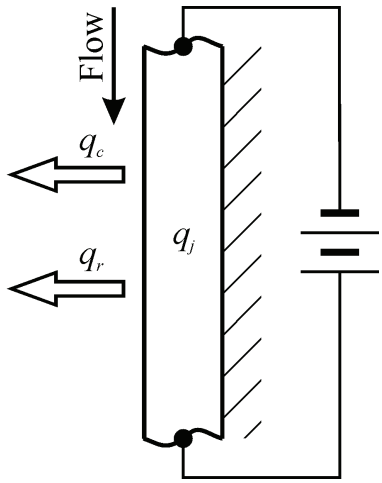

Figure 3.7: Schematic representation of the heated thin foil heat flux sensor (from Astarita and Carlomagno, 2013).

3.4 Heated thin foil heat flux sensor

IR cameras provide temperature measurements, but with proper implementation can also be used to measure convective heat flux. One of the possible solutions is the heated thin foil heat flux sensor. The sensor is made of a thermally thin foil (as schematically represented in Figure 3.7), which can be either metallic (stainless steel, constantan) or a printed board circuit, heated by a known heat flux, generally provided via Joule effect. One side of the foil is exposed to the incoming fluid, whilst the other is generally thermally insulated. In the case of the experiments reported in this thesis, one side is exposed to an impinging flow and the other is imaged by the IR camera. This is possible since the thermally thin condition is satisfied, i.e. the Biot number ($Bi = hs/k_f$, being h the convective heat transfer coefficient, s the foil thickness and k_f the foil thermal conductivity) is much lower than unity. The emissivity of this side is artificially increased by coating it with a thin layer of thermally black paint in order to increase the signal acquired by the thermal detector. In the hypothesis

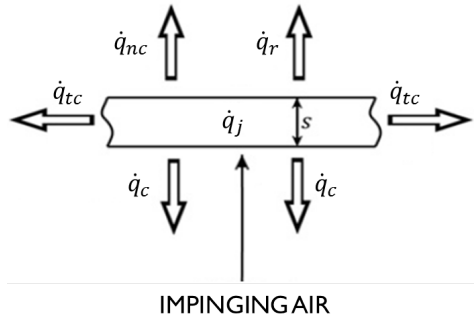

Figure 3.8: Energy balance within the slab.

of thermally thin foil, an energy balance can be posed within the control volume represented by the thin slab, as represented in Figure 3.8 in the case of an impinging jet experiment:

$$q_j = q_c + q_r + q_{nc} + q_{tc} \tag{3.15}$$

The terms reported in equation 3.15 are representative of:

- $\dot{q}_j$ is the heat flux provided via Joule effect with the stabilized power supply;

- $\dot{q}_c$ is the convective heat flux that can be expressed in terms of Newton's law as the product of the convective heat transfer coefficient h times the difference of the wall temperature T_w and the adiabatic wall temperature T_{aw};

- $\dot{q}_r$ is the radiative heat flux; this term is made of two contributions: one towards the impinging flow, which is negligible according to the small value of the emissivity of the plate in that direction. A second term is the radiation towards the ambient, which is regulated by Stefan-Boltzmann's law, $\dot{q}_r = \sigma\epsilon(T_w^4 - T_{amb}^4)$, being T_w the foil temperature T_{amb} the ambient temperature;

- $\dot{q}_{nc}$ is the natural convection heat flux; this term can be either estimated performing ad hoc experiments, correlating the natural convection heat flux to the power supplied to the foil via Joule effect or using the correlations available in the literature for an upward/downward facing hot plate (Incropera et al., 2011; McAdams, 1954).

- $\dot{q}_{tc}$ is the tangential conduction heat flux, which can be estimated as $\dot{q}_{tc} = k_f s \nabla^2 T_w$. This term is usually very small with respect to the heat flux provided by Joule effect (in the present case lower than 1%).

Equation 3.15 can be solved for h:

$$h = \frac{\dot{q}_j - \dot{q}_r - \dot{q}_{nc} - \dot{q}_{tc}}{T_w - T_{aw}} \tag{3.16}$$

It needs to be explicitly pointed out that both the heat losses and q_r are to be considered as correction terms and, in order to obtain accurate data, they should be a small fraction of the total Joule heating; otherwise, an error in their evaluation could produce a significant error in the measured h.

The T_w is representative of the wall temperature when the heat flux by Joule effect is provided to the plate and the jet is impinging onto it. The T_{aw} refers instead to the temperature distribution achieved by the plate when only the jet is impinging onto it and no electric current is provided. It physically represent the temperature distribution for which there is no convective heat transfer between the impinged plate and the surrounding fluid. It is frowned upon that both the T_w and the T_{aw} are captured (for the current application) at the steady state.

CHAPTER 4

Flow field topology of submerged jets with fractal generated turbulence

In this chapter, an extensive experimental study of the mean an instantaneous flow field features of a round jet equipped with a fractal grid is carried out . The results are compared to those obtained with the same round jet without the fractal insert. The influence of the presence of the grid on the velocity fluctuations, the spreading rate and the entrainment is detailed. Furthermore, the vortical features related to the effect of the grid onto the flow field are addressed.

4.1 Experimental procedure

4.1.1 Experimental setup and measurement technique

The experiments are carried out in the air jet facility at the University of Naples Federico II. Air is collected from the ambient using a centrifugal blower; an inverter is used to regulate the input shaft power. The flow rate is measured using a rotameter, then the blown fluid passes through

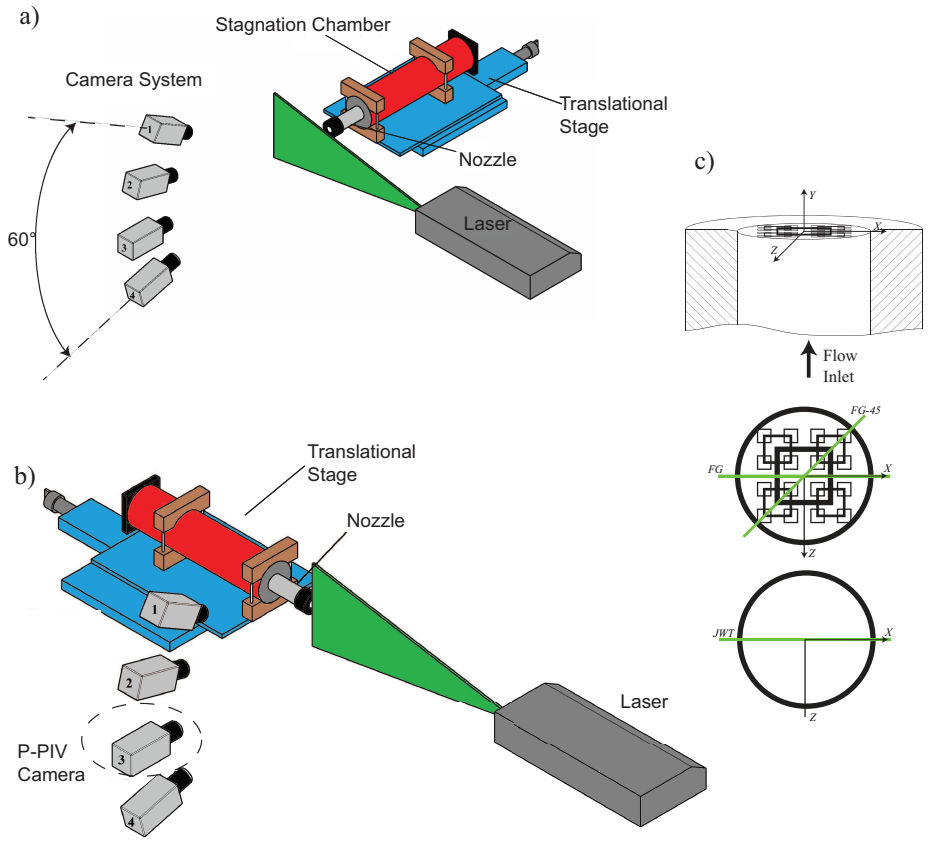

Figure 4.1: Experimental apparatus layout for Tomo-PIV experiments SET-A (top-left, a) and SET-B (bottom-left, b); for P-PIV experiments, the setup b) is representative of the real conditions, considered that only camera 3 is used and the laser volume is reduced to a laser sheet 0.5 mm thick. c) Detail of the grid located at the nozzle exit section with indication of the measurement plane for P-PIV. FG refers to the case of laser aligned to XY plane; in the FG-45 the laser is instead rotated around the Z axis of 45 deg with respect to the previous case (i.e. aligned to the diagonal of the largest grid iteration).

a radiator to control it in temperature and it is then collected within a stagnation chamber (internal diameter and length equal to 3 d and 20 d, respectively, being $d = 20mm$) located downstream of the nozzle to reduce the effects of fluctuations and biases from the feeding circuit. Furthermore, two honeycomb grids are located within the chamber in order to reduce the turbulence level due to large flow structures. Finally a contoured entrance is used to carry the air flow to a short-pipe round nozzle ($6.2d$ long) and a terminating cap in correspondence of the nozzle exit section where the grid is located (see Figure 4.1c for details). The final part of the air circuit (stagnation chamber and nozzle) is arranged on a traversing stage (as illustrated in Figure 4.1a-b), which ensures the movement of the nozzle along its own axis with accuracy of $0.1mm$.

The flow is seeded with olive oil particles (about $1\mu m$ diameter) generated by a Laskin nozzle. The mixing between the working fluid and the seeding particles occurs in a reservoir located upstream of the stagnation chamber.

The light source is a Quantel Evergreen laser for PIV applications ($532nm$ wavelength, $200mJ/pulse$, $< 10ns$ pulse duration) with an exit beam diameter of about $5mm$. The laser beam is enlarged using a bi-concave lens with negative focal length ($-50mm$); it is then adjusted in thickness using a second bi-convex lens with positive focal length ($100mm$), in order to ensure a uniform illumination along the depth direction. Finally a cylindrical lens (focal length $100mm$) enlarges the laser in the plane orthogonal to the optical axis of the camera. In the Tomo-PIV experiments the optical arrangement is slightly different with respect to the P-PIV one: the second spherical lens has a focal length equal to $200mm$; moreover, a pinhole is used in order to cut the peripheral region of the laser beam.

Two different sets of Tomo-PIV experiments are carried out (see Figure 4.1). A first set (here and in the following referred to as SET-A) where the crosswise flow field is investigated, with the track of the laser volume being parallel to the XZ plane (see Figure 4.1c for the reference system). In this case the illuminated region extends for about $8mm$ along the Y

direction (i.e. $1.6 < Y/d < 2$ along the nozzle axis) and for $30mm$ along the X and Z direction. A second set (here and in the following referred to as SET-B) is instead devoted to highlight the streamwise organization of the flow field. The laser volume is in this case directed along the YZ plane and such that about one side of the central square of the fractal grid belongs to the illuminated region. The extent of the laser volume is of $60mm$ along the Y direction, $26mm$ along the Z direction and $7mm$ along the X direction. A detail of the illuminated region for the two cases is given in Figure 4.2.

The P-PIV imaging system is made of one Andor sCMOS 5.5Mpixels camera (camera 3 in Figure 4.1b) equipped with a Nikon objective with focal length $50mm$; four Andor sCMOS cameras (camera 1-4 in Figure 4.1a-b) in Scheimpflug arrangement equipped with Tokina $100mm$ macro objectives are instead used for the Tomo-PIV experiments. The cameras are co-planar and subtend a solid angle of about 60 deg.

Both for P-PIV and Tomo-PIV experiments the acquisition frequency is set to $15Hz$.

The flow rate is regulated using a rotameter in order to obtain a Reynolds number (based on the nozzle exit section diameter d) equal to $Re = 15,000$. The resulting bulk velocity is then $V_j = 10.5m/s$ and this will be the value used to normalize all the quantities in the following of this chapter.

In the P-PIV experiments $2,000$ snapshots are captured. The imaged area extends for about $3d$x$11.5d$ in the XY plane, with a spatial resolution of about $10.5pix/mm$, i.e. $210pix/d$. The image interrogation is performed using a window size of 24x24pixels, 75% overlap and Blackman filtering window within the correlation process to tune the spatial resolution (Astarita, 2007).

The calibration procedure for the Tomo-PIV experiments is performed by taking images of a target (black dots on white background, $5mm$ pitch) moved through the measurement volume in seven different locations using a translational micrometric stage. The maximum calibration error is of

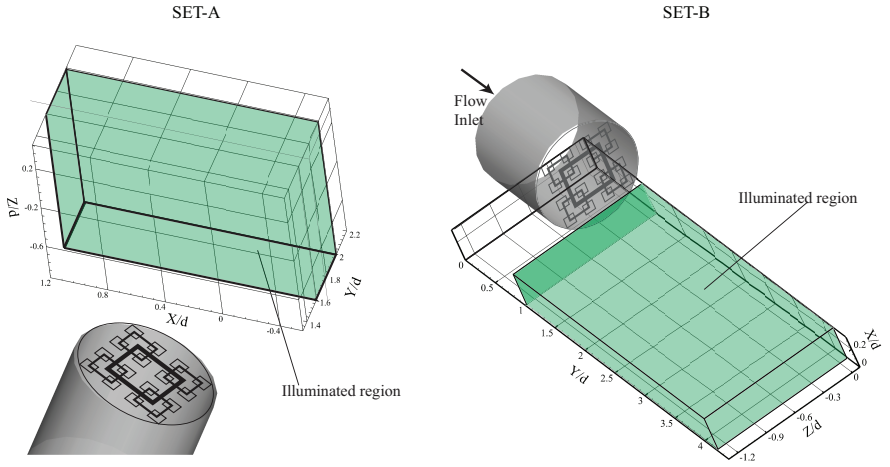

Figure 4.2: Definition of the illuminated regions for the SET-A and SET-B.

the order of 0.5 pixels. A self-calibration (Wieneke, 2008; Discetti and Astarita, 2014) procedure is then carried out in order to further correct the location of the laser volume using the scattering particles and to reduce reciprocal misalignments of the cameras. This leads to a reduction of the calibration error down to $0.03 pixels$.

The imaged area for the SET-A extends for $1.5d$ x $1.5d$ in the two directions orthogonal to the nozzle axis (namely X and Z) and about $0.45d$ along the nozzle axis (Y), with a digital resolution of $50 voxels/mm$ in the middle of the interrogation volume. For the SET-B the imaged area is of about $3d$ along the nozzle axis (Y), $1.3d$ in the direction aligned to the grid bar (Z) and $0.35d$ in the third direction (X), with a digital resolution of $36 voxels/mm$ in the middle of the interrogation volume.

For the SET-A, a sequence of 1,000 couples of images is acquired for each of the two investigated cases (FG and JWT). In the SET-B only the FG case is considered, still on a dataset of 1,000 samples.

A pre-processing is applied to the raw images in order to reduce the background noise. The pre-processing consists in: temporal minimum im-

age subtraction, in order to limit the effect of laser reflections within the flow field; a sliding minimum subtraction over a kernel of 7x7 pixels; a sharpening and Gaussian filtering over a 7x7 pixels in order to smooth the particles shape.

The reconstruction algorithm used for both SET-A and SET-B is the same. The 3D volume is reconstructed from the pre-processed images using 5 MART iterations (Elsinga et al., 2016), 1 MTE iteration (Novara et al., 2010) and 3 final MART iterations. During the iterative reconstruction with MART a non-isotropic Gaussian smoothing is applied on a 3x3x1 kernel (SFIT, Discetti et al., 2013) in order to reduce the artifacts of the reconstruction due to particles elongation along the depth direction in the reconstructed volumes. In order to check the quality of the reconstruction the signal to noise ratio defined as the reconstructed particles intensity inside the illuminated area versus that reconstructed outside is calculated. In the present experiment, the intensity of the laser is uniformly distributed across the volume which extends in the SET-A for about 450 *voxels* in depth and for about 260 *voxels* in depth in the SET-B, leading to a S/N ratio larger than 2 for both cases.

In the SET-A the reconstructed volume is interrogated using a 3D cross-correlation algorithm based on a final interrogation volume of 48x48x48 *voxels* (0.96x0.96x0.96mm^3), 75% overlap. The resulting vector pitch is 0.24mm. In the SET-B the final interrogation volume is slightly larger than the previous case, namely 64x64x64 *voxels* (1.77x1.77x1.77mm^3), 75% overlap. The vector pitch is then 0.44mm. The cross-correlation process is performed with an efficient algorithm based on sparse matrices and minimization of redundant calculations when using overlapping windows (Discetti and Astarita, 2012a). For the sake of understanding, an overview of the previously defined data is given in Table 4.1.

	P-PIV	SET-A	SET-B
Imaged area (d)	3x11.5	1.5x1.5x0.45	0.35x3x1.3
Digital resolution (pix/mm)	10.5	50	36
Reconstruction algorithm	None	MTE-MART	MTE-MART
Volume depth (vox)	None	450	260
Interrogation window size (vox)	24x24	48x48x48	64x64x64
Vector pitch (mm)	0.57	0.24	0.44

Table 4.1: Experimental and processing parameters.

4.1.2 Uncertainty analysis

An estimate of the measurement error can be given in the Tomo-PIV case from a physical argument. Indeed, it can be observed that the working flow régime is incompressible thus the divergence of the velocity field should be zero. The standard deviation of the divergence distribution over the entire measurement domain can be used as a statistical estimate of the error made on the evaluation of the velocity gradient. This value computed on the raw velocity field is equal to $0.03 voxels/voxel$ and it can be normalized with respect typical values of the vorticity within the jet shear layer (about $0.2 voxels/voxel$), thus obtaining a measurement error of about 15%. This uncertainty can be reduced down to 9% by applying a low-pass Gaussian filter on a kernel 3x3x3 with standard deviation equal to 1 to the raw velocity fields.

This method is not applicable in the P-PIV case. So, basing an estimate on the widely accepted figure of merit of 0.1 pixels (Adrian and Westerweel, 2011), this would turn into an uncertainty of about 1.5% of the maximum velocity.

4.1.3 Grid insert description

A sketch of the fractal insert is reported in Figure 4.3. The insert is made of a $0.5mm$ thick aluminium foil; the fractal structure is shaped

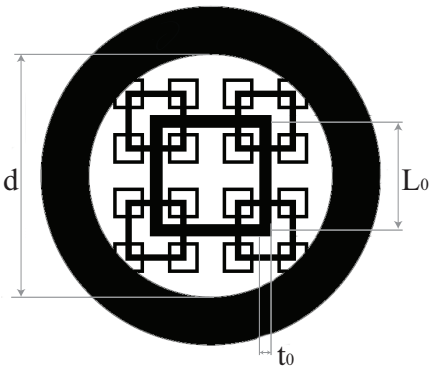

Figure 4.3: Fractal grid insert representation.

by laser cutting. The square pattern is repeated at three different scales (referred to as iterations). The length L_0 and the thickness t_0 of the first iteration are equal to $9mm$ and $1mm$, respectively. At each iteration j the length L_j and the thickness t_j are halved, i.e. $L_j = L_0 R_L^j$and $t_j = t_0 R_t^j$, with $R_L = R_t = 1/2$. For this grid the ratio between the largest and the smallest bar thickness (i.e. the thickness ratio t_r, identified as a significant scaling parameter by Hurst and Vassilicos, 2007) is equal to 4. The blockage ratio of the grid is equal to 0.32.

4.2 P-PIV Results

4.2.1 Statistical flow field features

The contour representations of the mean radial (a-c) and axial (d-f) velocity obtained by averaging 2,000 PIV samples are reported in Figure 4.4. From this point on when referring to the analysis in the plane aligned with the X axis direction the FG abbreviation is used; whilst FG-45 indicates the plane tilted of 45 deg with respect to the X axis (see Figure 4.1c).

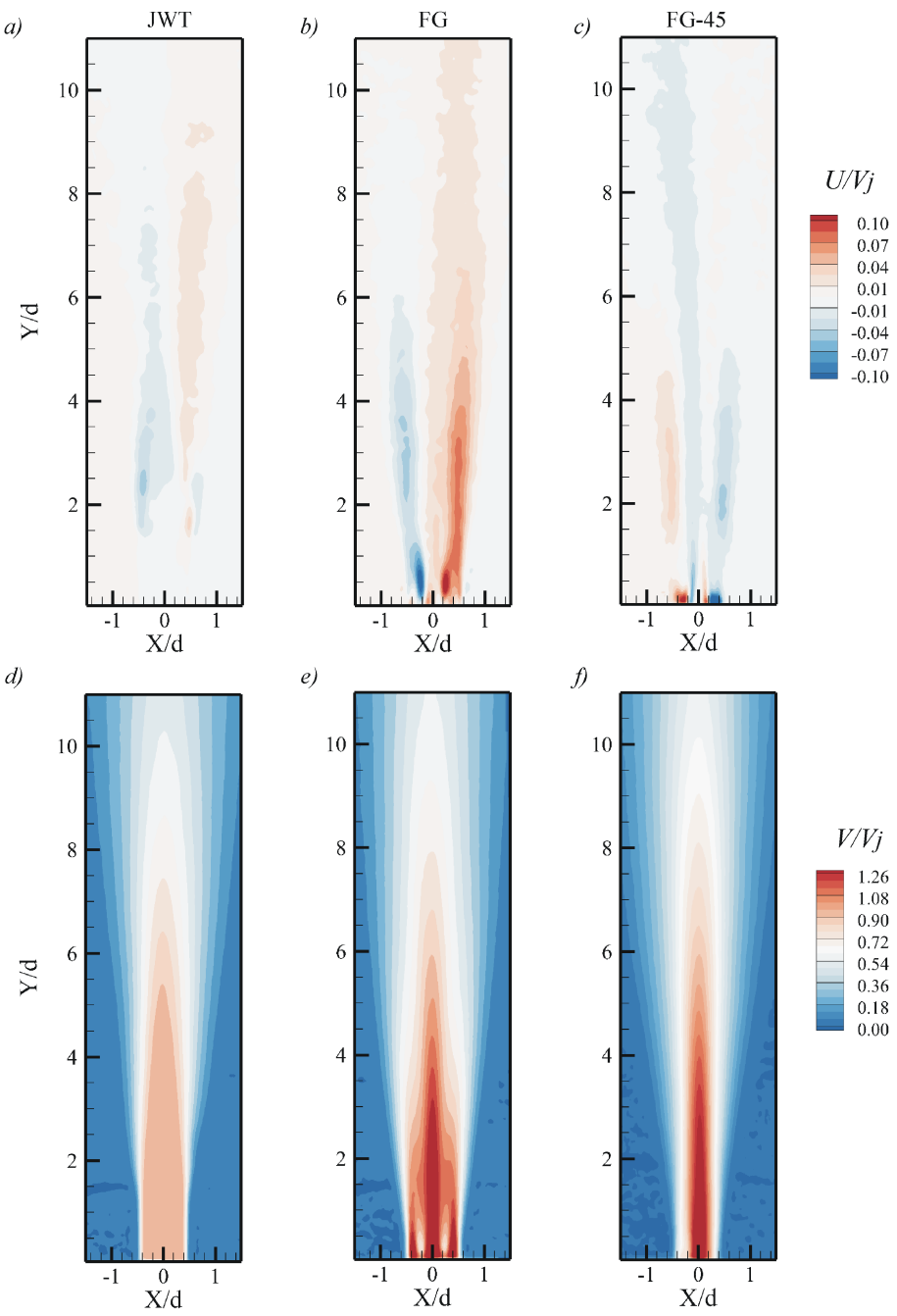

Figure 4.4: Mean radial (a, b and c) and axial (d, e and f) velocity contour representation for the JWT case (left) FG case (center) and FG-45 case (right).

The round jet without turbulator is characterized by an initial region which extends up to $Y/d = 1.5$ where the fluid issued through the nozzle is still developing. In this region the shearing effect of the surrounding air is still limited and the shear layer thickness, considered as the region where the axial velocity profile normalized with respect to the local maximum velocity attains values between 0.01 and 0.99, is approximately constant. However, the azimuthal disturbances are growing in amplitude and they reach their maximum at $Y/d = 1.5$ (Bradshaw et al., 1964; Becker and Massaro, 1968), where the shear layer becomes unstable and starts to spread (see Crow and Champagne, 1971; Grinstein, 2001), as can also be inferred looking at the radial velocity contour map representation (see Figure 4.4a). Beyond that point, the jet spreads almost linearly entraining fluid from the surrounding quiescent ambient.

In good agreement with what shown by other authors (see Abramovich, 1963; Crow and Champagne, 1971 among the others), along the jet centerline the velocity remains equal to the exit one for a region that penetrates for about $4.5d$, typically referred to as *potential core* (see also Figure 4.5). It is important to point out that, since the radial velocity distributions are much smaller in intensity than the axial ones, the maps are evidently more affected by both systematic and random errors (for example due to non-perfect alignment of the laser with the mean plane of the jet, as well as non-perfectly uniform magnification). These sources of uncertainty might sum up and lead to the slight asymmetries observed in the maps, which cannot be explained otherwise with physical arguments.

The FG case is instead characterized by three regions of large values of the axial velocity respectively located in correspondence of the central (and largest) iteration (region A, Figure 4.6) and of the *holes* between the grid bars and the edges of the grid (regions B and C, Figure 4.6). Moreover, the presence of the grid is also reflected into two regions of defect of velocity located in correspondence of the wake of the central iterations grid bars (under the regions D and E, Figure 4.6). The hornet-shape is soon lost due to turbulent diffusion beyond $Y/d = 2$, where the lateral jets merge

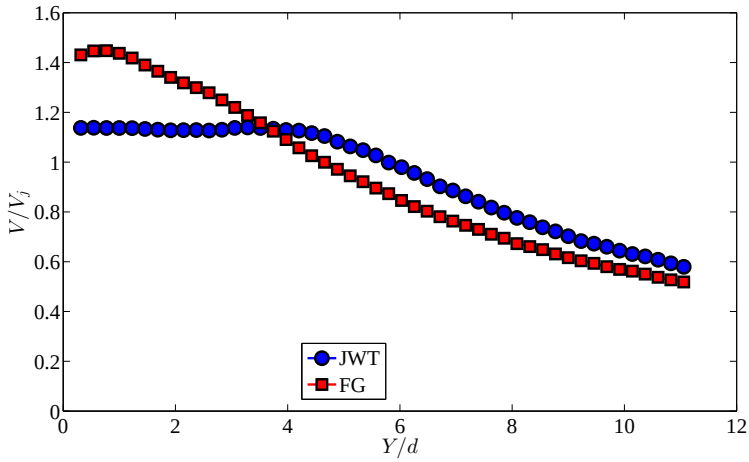

Figure 4.5: Axial velocity decay along the nozzle centerline for the JWT and FG cases.

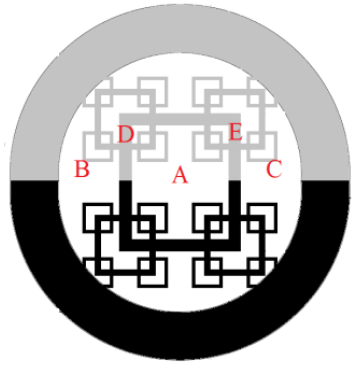

Figure 4.6: Identification of the main regions in the FG case.

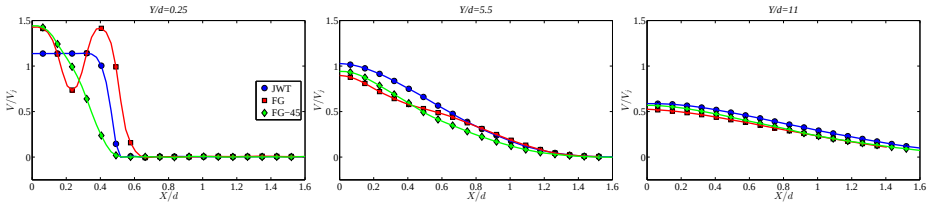

Figure 4.7: Axial velocity profiles for the JWT, FG and FG-45 cases at $Y/d = 0.25$ (left), $Y/d = 5.5$ (center) and $Y/d = 11$ (right).

into the inner one. Beyond $Y/d = 4$, the effect of the two outer jets cannot be perceived on the mean velocity profile.

The radial velocity profile is instead characterized at short distances from the nozzle by non zero values due to the momentum diffusion of the central jet towards the outer ones. Beyond $Y/d = 2$, this effect is smeared out and only the effect associated to the jet spreading can be identified.

In the FG case, the jet spreading starts immediately beyond the grid, differently from what observed in the JWT case. This effect has to be addressed to the blockage imposed by the wakes of the largest iteration of the fractal grid on the two lateral jets.

The FG-45 case presents a very strong central jet, whose radial extension is reduced with respect to the FG case due to the effect of the secondary iterations of the grid. The radial velocity is instead characterized by a strong entrainment of fluid from the quiescent ambient towards the jet axis; in addition to that, a smaller component of the radial velocity is also present that must be addressed to the central jet spreading (as it is clear looking at Figure 4.4, at small Y/d). At sufficiently large distances from the nozzle exit section, the effect of the grid on the mean velocity is negligible and the FG and FG-45 cases match.

These aspects can be further investigated looking at the axial velocity profiles (Figure 4.7) extracted at different streamwise locations ($Y/d = \{0.25, 5.5, 11\}$). The velocity profiles are normalized with respect to the

bulk velocity V_j as already outlined in the previous sections. The JWT case must then be compared to an average of the two cases with the grid insert, since the presence of the fractal turbulator unsettles the axial symmetry of the jet. At large distances from the nozzle exit section, it is possible to see how the three profiles are merging, suggesting that the effect of the fractal grid insert is being smeared out.

Figure 4.8 represents the root mean square (rms) of the axial v' and radial u' velocity fluctuations along with the in-plane Reynolds stress $u'v'$ for the three investigated cases at three different locations along the nozzle axis ($Y/d = \{0.25, 5.5, 11\}$). Striking differences emerge between the JWT case and FG, FG-45 cases, especially near the nozzle exit section.

At $Y/d = 0.25$ the effect of the fractal grid reflects in the presence of an intense peak in both the axial and radial velocity fluctuations in the lee of the largest grid bar iteration ($X/d \approx 0.25$); furthermore, a second maximum can be detected in correspondence of the jet shear layer, $X/d = 0.5$. It is interesting to notice that for the FG-45 case the effect of the merging wakes that detach from the grid iterations is combined to the one related to the shear layer, whose width is significantly broader than the FG case.

The JWT case is characterized by a peak located in correspondence of the jet shear layer for the axial fluctuation, whilst it is quite flat in the radial direction.

The in-plane component of the Reynolds stress highlights even more the differences between the three cases. The shear produced by the largest grid iteration causes a very intense minimum in the $u'v'$ distribution. This is indicative of negative radial fluctuations (inward flow) systematically coupled with positive axial fluctuations (ejections in the bars wake) and vice-versa, which is consistent with the picture of a spreading wake from the largest grid iteration.

Moving farther downstream, the FGs cases are slowly adjusting to the JWT case, losing memory of the presence of the grid. However, this effect is quicker in the FG-45 case; this must be addressed to the fact that the

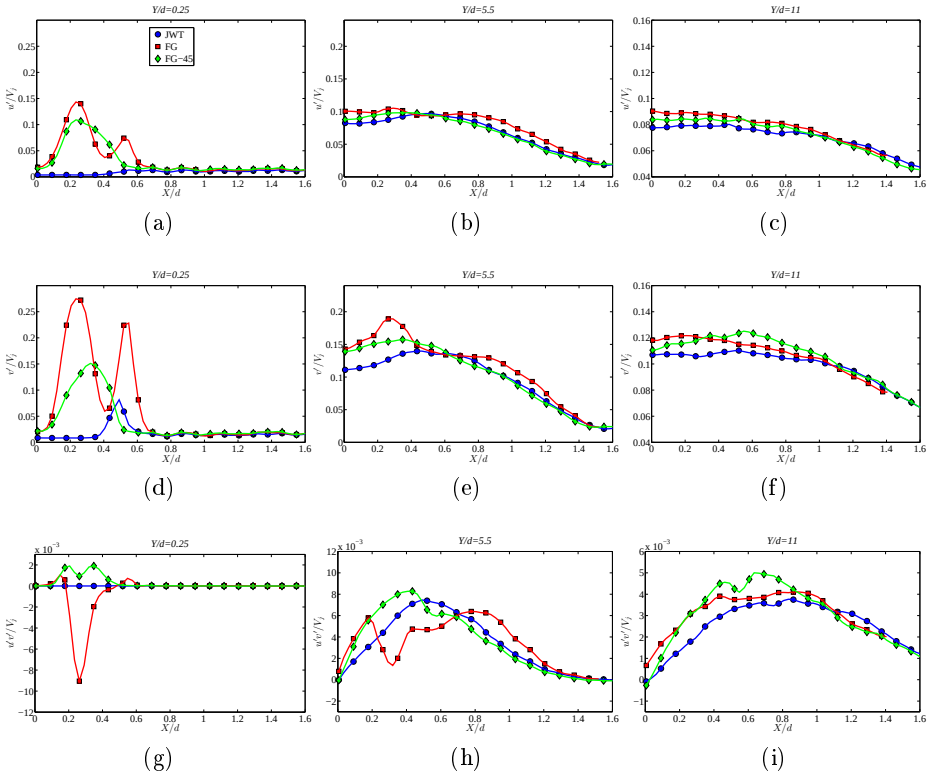

Figure 4.8: Radial (first row) and axial (second row) rms fluctuations and in-plane Reynolds stress (third row) for the JWT, FG and FG-45 cases at $Y/d = 0.25$ (left), $Y/d = 5.5$ (center) and $Y/d = 11$ (right).

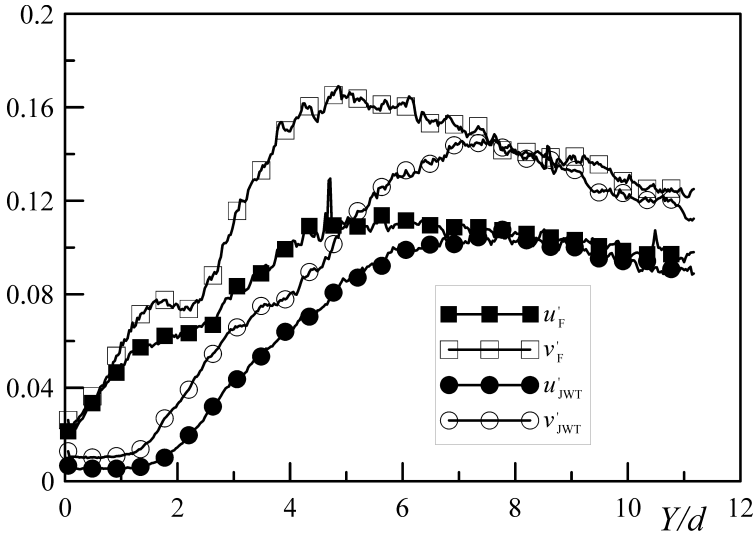

Figure 4.9: Axial and radial velocity fluctuations profiles along the jet centerline for the JWT and FG cases.

flow field in this case results to be strongly influenced by the blockage of the secondary iterations of the grid only in the very vicinity of the nozzle exit section. Due to the large momentum difference between the central jet and the jets issuing through the holes of the secondary iterations it was foreseeable that the jets interactions would be concentrated and resolved in few diameters beyond the grid.

Figure 4.9 underlines the main differences between the axial and radial velocity fluctuations produced in the JWT and FG cases along the jet centreline. The JWT case is characterized both in the axial and radial components, respectively identified with blue and black circles in Figure 4.9, by an initial plateau that extends for about $1.5d$; beyond that point, where the shear layer widens and start to penetrate towards the jet centreline, the presence of larger values of both the axial and radial velocity fluctuations can be perceived. In proximity of $Y/d \approx 8$ both components attain a maximum, and start to decrease in amplitude.

The FG case presents a turbulence production region immediately past the grid. Indeed, due to the inherent multi-scale structure of the fractal grid, the wakes that detach from the grid iterations will meet at different longitudinal distances. This behaviour is clearly at odds with the one typical of regular grids (Cafiero et al., 2016), where the single scale behaviour reflects in the fact that all the wakes will meet at the same longitudinal distance, thus producing a strong and rather immediate peak in the velocity fluctuations. In the fractal grid case, instead, the turbulence intensity level progressively builds up, attaining a maximum at a larger streamwise distance.

According to Mazellier and Vassilicos (2010) in the case of free-shear wake of a fractal grid a local maximum should be identified at about $0.45L_0^2/t_0$ in the axial velocity fluctuations v'. For the used grid, this would turn into a streamwise distance of about $1.82d$. Beyond that point, in their investigation a steep turbulent energy decay was spotted, which led to the controversial discussion on whether it is exponential or modelled by the classical power law of the regular grids, or an hybrid between the two solutions (George, 1992; Hurst and Vassilicos, 2007; Valente and Vassilicos, 2011).

Differently from the case investigated by Mazellier and Vassilicos (2010) the local maximum at $Y/d = 1.6$ in the turbulent kinetic energy profile is followed by another production region up to $Y/d = 4.5$ due to the penetrating shear layer. In fact, moving further downstream, the latter effect sums up to the production due to the fractal grid. The observed plateau for $1.6 < Y/d < 2$ can be addressed to this interaction. Indeed, the turbulence injected by the shear layer balances out the decaying turbulence produced by the grid. In addition to this, the local maximum of the turbulent kinetic energy anticipates the one predicted by Mazellier and Vassilicos (2010) in a free-shear case. This aspect must be addressed to the growing external shear layer that *pushes* the wakes towards the nozzle axis, causing an anticipated merging of the wakes of the main iteration. Even though this heuristic argument does support the view of an anticipated peak, a word

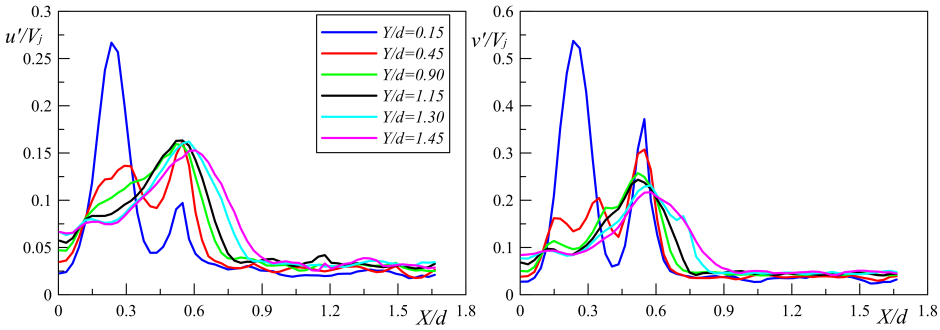

Figure 4.10: Radial (left) and axial (right) velocity fluctuations for the FG case at $Y/d = \{0.15, 0.45, 0.9, 1.15, 1.3, 1.45\}$.

of warning comes from using the correlation provided by Mazellier and Vassilicos (2010) on a grid with significantly different blockage ratio (0.25 in the study by Mazellier and Vassilicos, 2010 instead of the currently used 0.32).

It is also interesting to notice how, at sufficiently large distances from the nozzle exit section, the radial and axial components of the FG and JWT cases collapses into the same values. This represents a further evidence of the fact that the flow field beyond $Y/d \approx 8$ is not significantly affected by the presence of the grid.

Looking at the rms of the radial u' and axial v' velocity fluctuations in the near vicinity of the nozzle exit section (for $Y/d < 1.45$), reported in Figure 4.10, it can be seen that the shear layer rapidly broadens interacting with the growing wake. In particular, towards the jet edge the radial fluctuation u' rapidly increases as Y/d increases, causing the penetration of the external shear layer towards the jet centreline and, as a consequence, interacting with the growing wake generated from the grid bar.

In order to support this assertion the spreading of the wakes of the first iteration has been investigated. In general, it has been shown by Symes and Fink (1977) and Wygnanski et al. (1986) that the wake profile varies

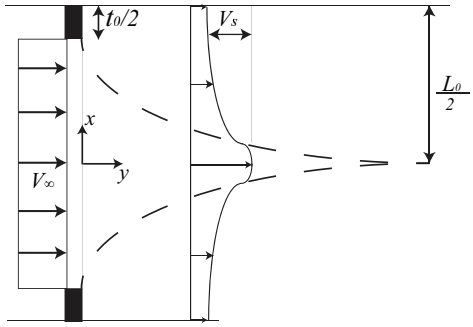

Figure 4.11: Schematic representation of the two dimensional wake due to the largest grid iteration.

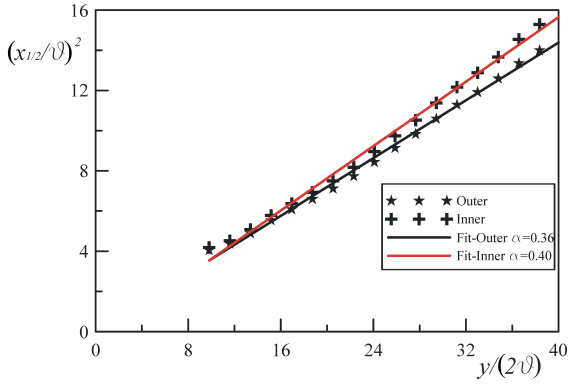

Figure 4.12: Wake half-width $\left(\frac{x_{1/2}}{\theta}\right)^2$ as a function of the location downstream $y/(2\theta)$.

as (schematically represented by the dashed line in Figure 4.11):

$$\left(\frac{x_{1/2}}{\theta}\right)^2 = \alpha\left(\frac{y - y_0}{2\theta}\right) \tag{4.1}$$

where $x_{1/2}$ is the wake half-width, i.e. the location where the velocity profile attains its half value with respect to the velocity V_∞ (calculated in correspondence on the nozzle exit section, at $x/d = 0$), y_0 is the virtual origin, and θ the momentum thickness and:

$$\left(\frac{V_\infty}{V_S}\right)^2 \propto \left(\frac{y - y_0}{2\theta}\right) \tag{4.2}$$

being V_S the maximum value of the self-similar small-deficit velocity profile (see Figure 4.11). As the growing external shear layer interacts with the wake which detaches from the largest grid bar iterations, it may be argued that the spreading rates of the inner (towards the nozzle centerline) and outer (towards the shear layer) wakes are different.

Computing the self-similar velocity deficit, it is possible to demonstrate how the wake spreading results to be asymmetric: in particular Figure 4.11 shows that the spreading towards the centerline is faster than the one towards the external shear layer. Moreover, comparing these results to those obtained by Gomes-Fernandes et al. (2012) who found a spreading rate of $\alpha = 0.287$, it is possible to see that in the present case the spreading rate α is about 40% higher than in the case of a free-shear flow. The faster and asymmetric spreading rate is consistent with the picture of differential effects of internal and external shear layers growing, which can be responsible of the anticipation of the turbulence peak on the centreline.

4.2.2 Mean Entrainment rate

As the entrainment rate is directly related to the scalar transfer of a jet (see Grinstein, 2001; Liepmann and Gharib, 1992) it is of paramount importance to compare the entrainment associated to the JWT with the one obtained using a FG. In Figure 4.13 the streamwise evolution of the

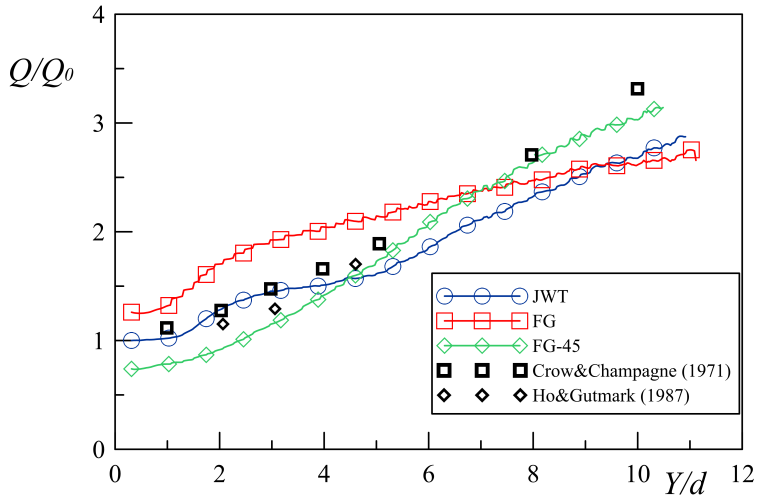

Figure 4.13: Mean entrainment rate for the JWT, FG and FG-45 cases.

mean volumetric flow rate Q with respect to its value at the inlet section Q_0 is depicted for the three studied cases. The flow rate Q is defined as:

$$Q = \int_0^{2\pi} \int_0^r rV \, \mathrm{d}r\mathrm{d}\theta = 2\pi \int_0^r Vr \, \mathrm{d}r \tag{4.3}$$

in the assumption of axial symmetry of the jet, being r the radial distance from the nozzle axis. While this can be reasonably asserted for the JWT case, this definition is not rigorous for the FG case, where the presence of the grid disrupts the symmetry of the flow field. However, computing Q/Q_0 per unit angle in the two limit cases of FG and FG-45, it is possible to define the upper and lower boundaries of the mean entrainment.

First, it is interesting to notice that for the JWT the entrainment rate, as already outlined into the literature, increases starting from $Y/d \approx 2$.

The increment of the volumetric flow rate is due to the growth of azimuthal instabilities within the jet shear layer, and the generation of ring vortices that engulf fluid from the quiescent ambient. Beyond $Y/d \approx 6$ the vortex pairing occurs and the JWT becomes self-similar leading to a

linear growth of Q/Q_0. As a further evidence, in Figure 4.13 the data relative to the experiments of Crow and Champagne (1971) and Ho and Gutmark (1987) are reported. These data are relative to rather different inlet conditions, (respectively an orifice and a small aspect ratio elliptic nozzle), thus the attained show some discrepancies with those obtained in this work for the JWT case. However, it is important to point out that in all the cases the entrainment rate increases nearly linearly with the longitudinal coordinate.

The jet half-width b (Figure 4.14) at a given streamwise location Y/d is computed considering the region where the axial velocity normalized with respect to its local maximum attains values higher than 0.01. It is possible to see how, the JWT case presents a jet half-width b nearly constant for about $1.5d$. At the end of the potential core, for $Y/d > 5$, it is possible to spot a clear linear spreading of the jet half width. The jet spreading rate $S = \mathrm{d}b/\mathrm{d}y$ is in the present case 0.075, which results to be in good agreement to the values reported by Pope (2000) between 0.07-0.1.

In the presence of the grid, a rather different behaviour is visible. Indeed, in the FG case the jet spreading starts immediately past the grid, due to the effect of the streamwise vorticity generated by the grid. At short Y/d locations, it is possible to see how the FG-45 case presents a significantly smaller value of the jet half-width, due to the effect of the secondary grid iterations. However, for $Y/d > 4$, the spreading rate is particularly large, attaining then values similar to those of the FG case for $Y/d \approx 8$. This is evidently due to the fact that the flow field is not affected by the initial condition imposed by the grid.

4.2.3 Instantaneous flow field organization

An instantaneous realization of the axial velocity V/V_j for the JWT, FG and FG-45 cases is reported in Figure 4.15. As already outlined in Sec. 4.2.1 presenting the mean flow field, in the JWT case beyond $Y/d = 1.5$ the shear layer becomes unstable due to the growth of the Kelvin-Helmholtz

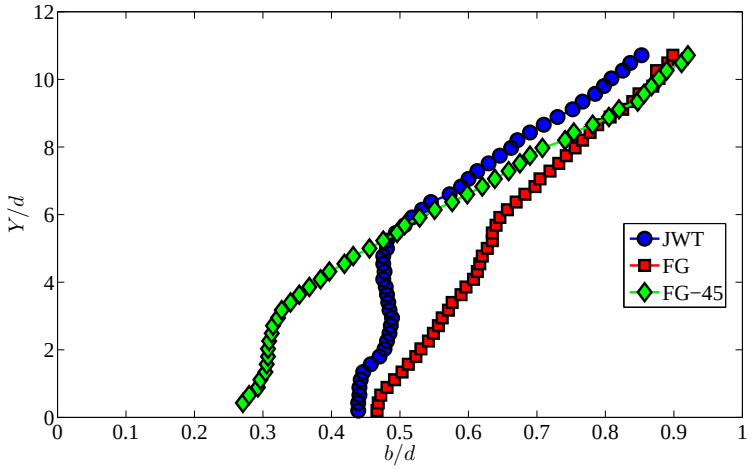

Figure 4.14: Jet half-width for the JWT, FG and FG-45 cases.

instabilities. This turns into an oscillating behaviour of the axial velocity that attains lower values in correspondence of the regions where there is the formation of a toroidal vortex. This behaviour is kept up to $Y/d \approx 6$, where the pairing of the toroidal structures occur and the flow field becomes fully three dimensional (see Violato and Scarano, 2011 for a more detailed discussion of this phenomenon).

The FG case in the vicinity of the nozzle exit section is characterized by a hornet shape due to the fluid issuing through regions A, B, C (see Figure 4.6). The two outer jets are rapidly dissipated within the first two diameters. Beyond that point, the central jet exhibits a meandering whose amplitude increases as Y/d increases. This behavior is typical of two dimensional jet flows (Landel et al., 2012a). In the vicinity of the nozzle exit section, a limited jet oscillation can be experienced, as in the present case. However, this mechanism has to be addressed to the presence of eddies which arise because of the interaction of the jet with the quiescent ambient air. These vortices grow in size almost linearly as the streamwise distance increases. In the present case, where the issuing jet is not two dimensional, the meandering has most likely to be addressed to the presence

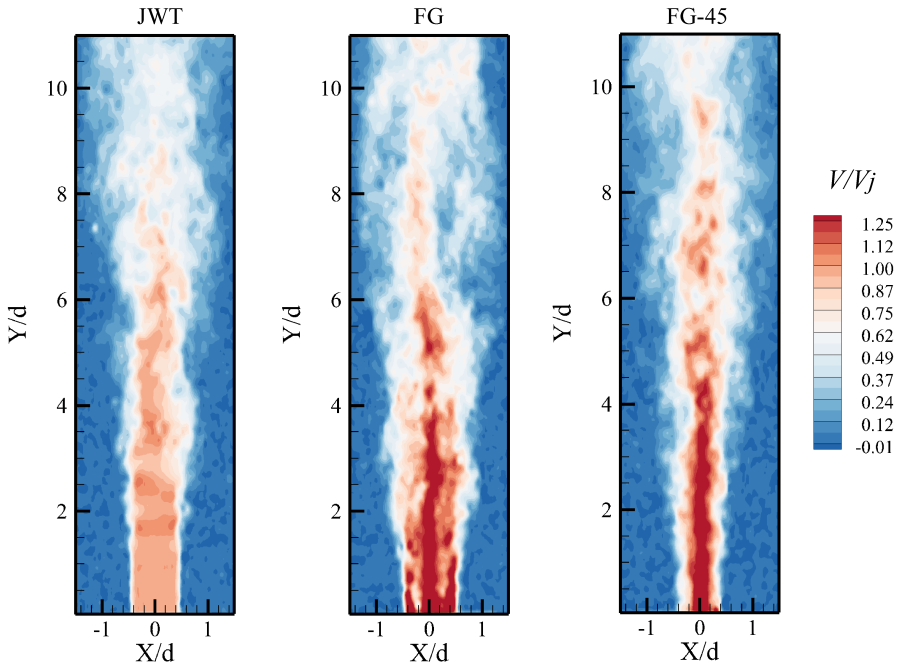

Figure 4.15: Instantaneous realization of the axial velocity contour representation for the JWT case (left) FG case (center) and FG-45 case (right).

of a helical structure that embraces the jet, thus requiring a 3D flow field characterization. This aspect will be addressed in paragraph 4.3.2. Due to the high local blockage ratio introduced by the secondary grid iterations, the FG-45 case does not present any lateral jets. Beyond $Y/d \approx 2$ the FG-45 case exhibits an oscillating behavior similar to that described for the FG case.

4.3 Volumetric PIV results

4.3.1 Mean flow field features

Due to the strong 3D features of the flow field, targeted 3D experiments can shade some light on the organization of the coherent structures that characterize the flow field. The mean flow field organization, calculated over 1,000 samples for the FG (a) and JWT (b) case is reported in Figure 4.16. For the FG case (a), the hornet shaped axial velocity profile as highlighted in the P-PIV experiments reflects into a cross-shaped iso-surface of $V/V_j = 1$ (color-coded in translucent grey) which embraces the central jet. As already outlined when presenting the P-PIV results, this peculiar shape must be addressed to the jets issuing through the regions B, C, B' and C', as indicated in Figure 4.16a in correspondence of the grid. Moreover, the iso-surface of axial velocity $V/V_j = 1.6$ is reported in dark orange to underline the central jet (corresponding to region A). In terms of turbulence production, besides the effect of the shear layer due to the interaction of the quiescent air with the issuing jet, for the FG case the turbulence generated by the grid deserves consideration. The iso-surface of turbulent kinetic energy (tke) normalized with respect to the bulk velocity of the jet V_j is also reported in Figure 4.16a (cyan, $tke/V_j^2 = 0.074$). The four structures indicated in cyan are associated to the turbulence produced by the bars of the first iteration (labelled as D, E, D' and E' in Figure 4.16). As already mentioned, the turbulence produced by the grid, along with the larger axial velocity values of the jets issuing through the grid iterations, were responsible of the strong gap between the FG and JWT in terms of scalar transfer efficiency when using impinging jets equipped with fractal grids. The turbulent kinetic energy distribution is consistent with this picture. However, a key-role is also played by the production of streamwise vortices. In fact, further evidence can be extracted by observing the iso-surfaces of normalized axial vorticity $\omega_y d/V_j$ reported in Figure 4.16a, which reveal the presence of couples of counter-rotating

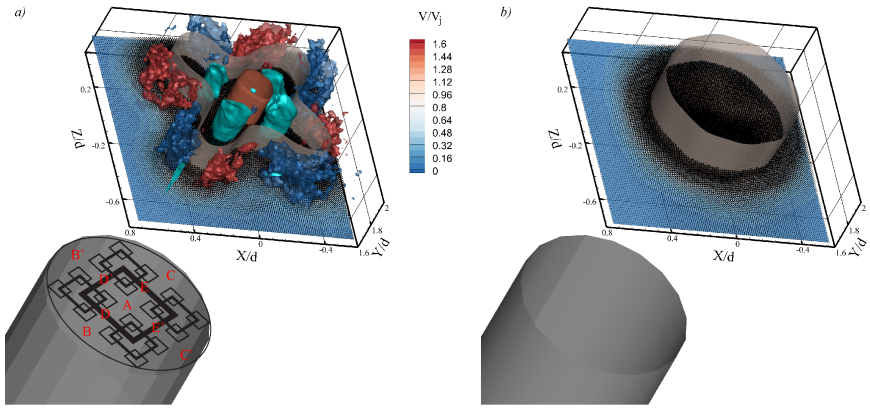

Figure 4.16: Mean flow field features for the SET-A. a) FG: Iso-surfaces of axial velocity $V/V_j = 1.6$ (orange) and $V/V_j = 1$ (translucent grey); Iso-surfaces of axial vorticity $\omega_y d/V_j = 0.65$ (red) $\omega_y d/V_j = -0.65$ (blue); Iso-surface of $tke/V_j = 0.074$ (cyan). Contour representation of the axial velocity in the XZ plane along with vector plot. b) JWT: Iso-surface of axial velocity $V/V_j = 1$ (translucent grey); contour representation of the axial velocity in the XZ plane along with vector plot.

vortices that evolve in the streamwise direction. They must be addressed to the interaction of the fluid issuing through the regions B, B', C and C' with the grid iterations. The production of these energy containing structures which evolve in the streamwise direction are responsible of the increment of the entrainment rate as already shown by Grinstein (2001) and reported in Figure 4.13. As these coherent structures are generated immediately past the grid, the entrainment rate increases starting from $Y/d = 0$ as outlined in paragraph 4.2.2. This is not true in the JWT case, where the entrainment is associated to the jet shear layer instability and the growth of toroidal vortices, which occurs starting from $Y/d \approx 1.5$. These streamwise structures have larger penetration and spatial lifetime than the vortex rings generated in the shear layer, and might be largely responsible of the heat transfer enhancement that will be shown in the next chapter in the case of impinging fractal jets.

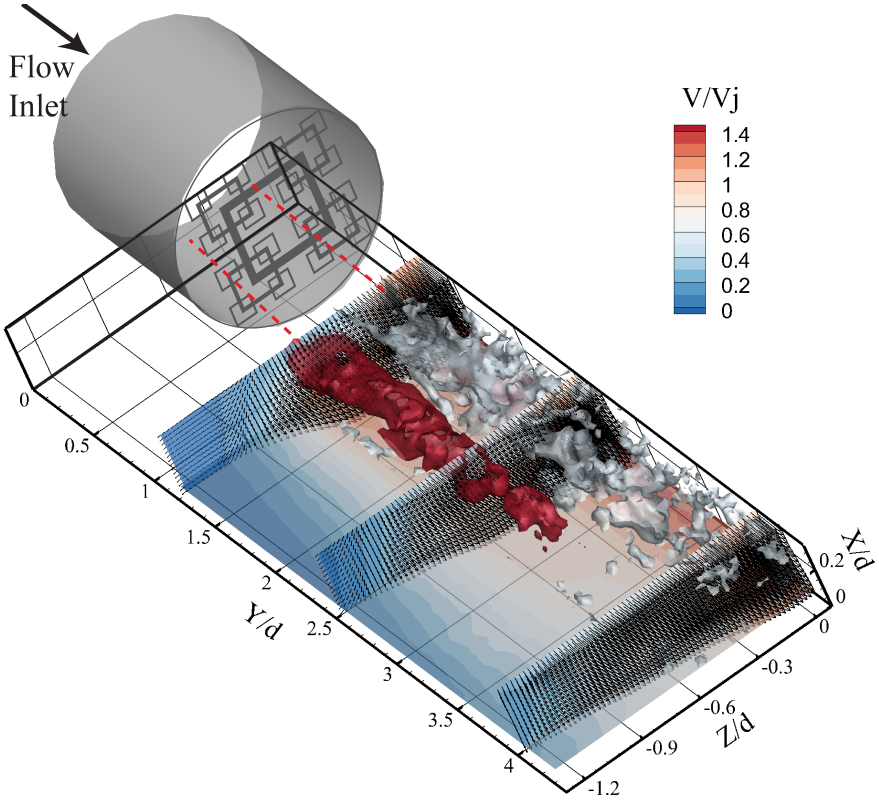

Figure 4.17: Mean flow field features for the SET-B; iso-surface of axial vorticity $\omega_y d/V_j = 0.65$ (red) and $\omega_y d/V_j = -0.15$ (grey). Contour representation of the axial velocity both onto the YZ $(X/d = 0)$ and XZ $(Y/d = \{1.2, 2.5, 4\})$ planes.

The SET-B of experiments, in this sense, can add some useful information on the penetration of the streamwise vorticity along the centreline. Additionally, it provides further insight in the interaction between primary and secondary iterations. The ensemble averaged flow field for the SET-B is reported in Figure 4.17. The contour representation of the axial velocity is illustrated in the $X/d = 0$ and $Y/d = \{1.2, 2.5, 4\}$ planes. Striking differences can be spotted with respect to the flow field organization of the JWT case (see Violato and Scarano, 2011, 2013). The normalized axial vorticity iso-surface $\omega_y d/V_j = 0.65$ corresponds to the one represented in Figure 4.16a, i.e. to the vortex generated because of the interaction of the flow with the grid in correspondence of region B. However, it may be argued that as fractal grids cover inherently multiple scales, as a function of the scale of the grid iteration the flow can be characterized by the presence of different structures. Indeed, the interaction of the central jet with the secondary grid iterations produces another streamwise vortex, which rotates in the opposite direction with respect to the previous one ($\omega_y d/V_j = -0.15$).

It must be noticed that, for a symmetry argument, another vortex characterized by an opposite value of axial vorticity ($\omega_y d/V_j = 0.15$) will be generated. This turns into the consideration that a total of eight different streamwise counter-rotating vortices are shed by the fractal grid due to the interaction of the air issuing through region A and the secondary grid iterations.

4.3.2 Further insights in the instantaneous flow field organization: 3D vortical structures

The analysis of an instantaneous realization of the flow field for the SET-B is documented in Figure 4.18. The iso-surfaces of axial velocity V/V_j and $Q_{vv} > 0$, being Q_{vv} the second invariant of the velocity gradient tensor (see Jeong and Hussain, 1995) are reported along with the contour representation of the axial velocity in the plane $X/d = 0$. A he-

lical structure that embraces the central jet (region A, see Figure 4.16a) is highlighted using black dashed lines. It is important to explicitly notice that, as the jet core is not totally contained within the investigated region, only a portion of the helix is measured. This structure is most likely responsible for the streamwise meandering of the central jet as illustrated in the P-PIV results (see paragraph 4.2.3).

In the first $2.5d$ the helix appears to be quite coherent, keeping a spacing that is nearly uniformly equal to about $0.2d$. However, the P-PIV measurements (Figure 4.15), which cover a larger streamwise distance, would suggest that the pitch of the helix is an increasing function of Y/d, although this aspect cannot be explored through the present 3D measurements due to the limited size of the investigated volume.

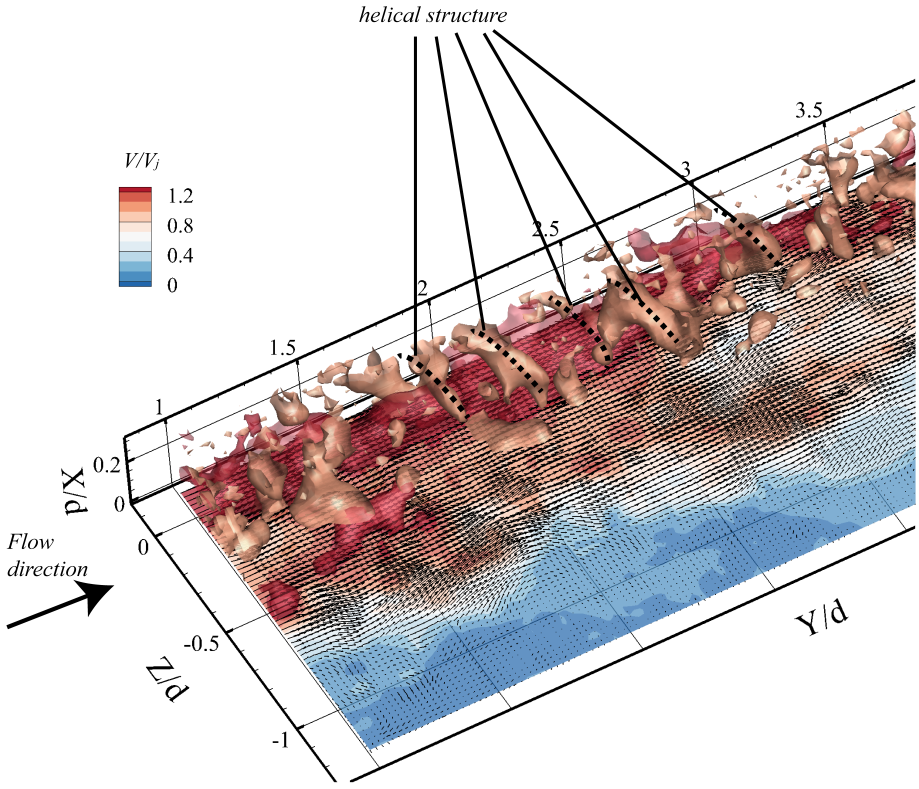

Figure 4.18: Instantaneous realization of the flow field for the SET-B; iso-surface of axial velocity $V/V_j = 1.2$ (red) and of $Q_{vv} > 0$ (orange). Q_{vv} values are blanked for $Z/d < -0.3$, in order to identify the helical structure. Contour representation of the axial velocity in the YZ plane with tangent vector representation.

CHAPTER 5

Heat transfer enhancement of impinging jets with fractal-generated turbulence

In this chapter, a comparison of the convective heat transfer coefficient properties of an impinging jet equipped with a regular grid (RG), a square fractal grid (SFG) and without any turbulence promoter is carried out. The RG and SFG are opportunely designed such that the blockage ratio is the same ($\sigma = 0.32$). In order to perform a fair validation of the capabilities of the SFG with respect to the RG and JWT cases, the experiments are carried out under the same power input, i.e. the same product of the volumetric flow rate times the pressure drop between the stagnation chamber and the ambient. The effect of the position of the grid with respect to the nozzle exit section is assessed by locating the insert at three different positions: in correspondence of the nozzle exit section (of a round nozzle having diameter d), 0.5 d and 1d upstream the nozzle exit section. Furthermore, the effect of the Reynolds number is taken into account by considering two different power inputs (defined as above).

5.1 Experimental apparatus

The experimental setup is sketched in Figure 5.1a. The air provided by a fan is conditioned in temperature with a heat exchanger and then the mass flow rate is measured with a Venturi tube. The cooling air passes through a plenum chamber (in which the total pressure is measured), a straight pipe, whose length is $6d$ (where d is the exit diameter, equal to 20 mm) and, if present, through the insert and a terminating cap (which may, eventually, increase the total length of the pipe up to $7d$).

The air impinges normally on a thin constantan foil (200 mm long, 450 mm wide, 50 μm thick), whose flatness is ensured by a stiffening frame. The separation (indicated with the symbol Y) of the nozzle exit section from the target plate is adjusted by using a precision translation stage to move the jet plenum chamber along its own axis perpendicular to the heated surface. The target plate is heated by an electric current and cooled by the jet impinging on it.

The grid insert is placed within a small cavity shaped into a cap that is attached to the straight pipe (see Figure 5.1b-d for the graphical representation). The depth of the cavity is equal to the grid thickness, i.e. 0.5 mm. Three caps with a total height of 0.5, 10.5 and 20.5 mm have been used, thus corresponding to $z = 0.5$, 10 and 20 mm respectively. The smallest cap is knife-edged close to the grid location (with angle of 45^o) to reduce its influence and reproduce the condition of grid placed at the nozzle exit. It is helpful to explicitly notice that the grid is always placed at the end of the straight pipe for all the values of z. More specifically, this results in the condition that the grid is practically in correspondence of the nozzle exit when the smallest cap is used (i.e. $z/d = 0$), whilst it is upstream of the nozzle exit in the other cases (i.e. $z/d = 0.5, 1$), thus with a total pipe length of $6.5d$ and $7d$ respectively. When testing the JWT the terminating cap is not used, thus the obtained results are relative to the case of outflow from a straight pipe with $6d$ length.

The temperature of the foil is measured by an InfraRed (IR) camera

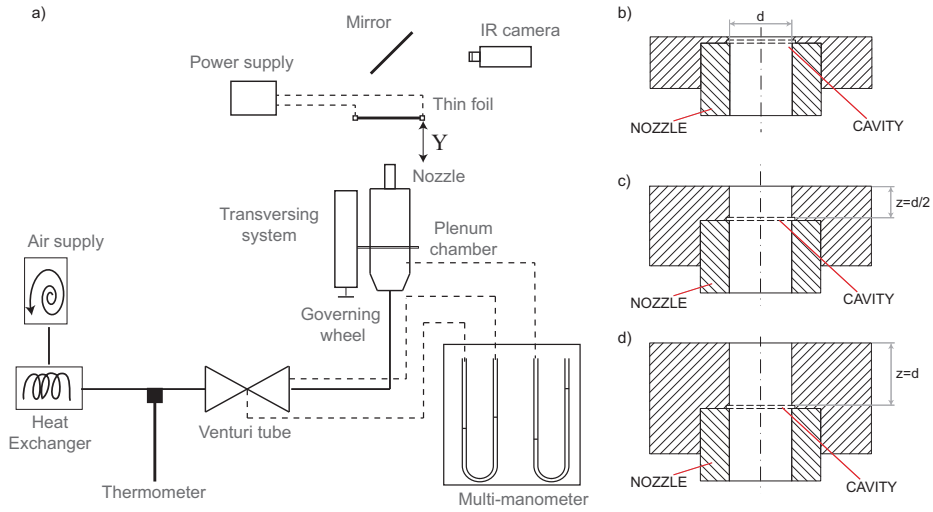

Figure 5.1: Schematic description of the experimental setup with a detail of the three caps (a-c) used.

FLIR SC6000 (focal plane array with 640 x 512 pixels working in the 8 -12 μm band). The camera is placed at the opposite side to that of impingement; this is acceptable being the Biot number ($Bi = hs/k_f$, where s is the foil thickness, k_f is the thermal conductivity of the foil and h is the convective heat transfer coefficient) lower than 0.01 for the entire set of experiments, so that the temperature can be considered uniform across the foil thickness with good approximation. The back side of the foil (i.e. the one opposite to the impingement area) is covered with high emissivity paint ($\epsilon = 0.95$) in order to increase the signal/noise ratio with respect to the radiation coming from the surrounding ambient.

The temperature map is discretized with a resolution of $3.2 pix/mm$, thus corresponding to $64 pix/d$. The convective heat transfer coefficient is evaluated via the heated thin foil steady state heat flux sensor (Astarita and Carlomagno, 2013, see chapter 3.4). It must be explicitly noticed that the natural convection heat flux in this case never exceeds the 7% of the forced convective heat flux (Incropera et al., 2011; McAdams, 1954).

Each temperature map is obtained by averaging 1000 recorded images at a frame rate of 30 Hz. The integral timescale is well below the time separation between the frames (in the worst case the jet bulk velocity is $12m/s$, thus considering that the nozzle diameter is $20mm$ it leads to a timescale equal to $1.6ms$, against $33.3ms$ between two consecutive frames), thus the samples can be considered statistically independent. Only time-averaged results are reported since the thermal inertia of the foil does not allow to accurately follow the turbulent fluctuations in the instantaneous realizations. Indeed, considering the foil thickness as the reference length across which the heat is transferred by conduction, the characteristic time obtained by setting the Fourier number equal to 1 is $0.45ms$, while the estimated Taylor and Kolmogorov timescales are respectively $100\mu s$ and $8\mu s$.

The convective heat transfer coefficient values are presented in non-dimensional form in terms of the Nusselt number spatial distribution and area averaged profiles $\overline{Nu}(r)$, where:

$$\overline{Nu}(r) = \frac{1}{\pi r^2} \int_0^r \int_0^{2\pi} \xi \cdot Nu(\xi, \theta)\, \mathrm{d}\theta \mathrm{d}\xi \tag{5.1}$$

$$Nu_r(r) = \frac{1}{2\pi} \int_0^{2\pi} Nu(r, \theta)\, \mathrm{d}\theta \tag{5.2}$$

The two parameters give a direct grasp on the local mean value and the integral of the convective heat transfer over a considered area, respectively.

An uncertainty analysis on the values measured by the Eq. 3.16 is conducted with the procedure suggested by Moffat (1988). The Nusselt number distribution is recalculated perturbing of the related uncertainty (listed in Table 5.1) each of the following quantities: the foil thickness, the emissivity of the black paint, the measured ambient, adiabatic wall and foil temperature, the input current and voltage, the nozzle diameter. The analysis leads to a $\pm 4.6\%$ range of uncertainty for the local Nusselt number. In Table 5.1 the typical values and the uncertainty associated

to each parameter that has been taken into account for the Nusselt number computation together with the effective percentage of uncertainty on the final measure are reported. It can be concluded that the main effect on the Nusselt number estimate is related to the foil and adiabatic wall temperature measurements. The total error is then estimated as the root sum square of the single errors. Besides the errors listed in Table 5.1, there is also the one related to the pressure measurement (estimated to be about 2% of reading), which has not a direct effect on the Nusselt number definition.

The experiments are performed by varying both the nozzle-to-plate distance ($Y/d = \{1, 2, 3, 4\}$) and the position of the grid with respect to the nozzle exit ($z/d = \{0, 0.5, 1\}$). Only relatively short nozzle-to-plate distances are considered; indeed, in this scenario the effect of the enhanced turbulence within the potential core is dominating. For larger separations the large-scale disturbances generated within the shear layer are expected to have an overwhelming impact on the heat transfer properties, while the grid-generated turbulence in the potential core is smeared out by turbulent diffusion.

5.1.1 Grid inserts description and tests configuration

A sketch of the grids used for the experiments is reported in Figure 5.2. The grids are shaped by laser cutting a 0.5 mm thick aluminium foil. The fractal grid is the one already presented and tested in Chapter 4. Using the scaling relations proposed by Hurst and Vassilicos (2007), an equivalent regular grid is designed (i.e. with the same blockage ratio σ and effective meshlength M_{eff}):

$$M_{eff} = \frac{\pi d^2}{P}\sqrt{1-\sigma} \tag{5.3}$$

$$\sigma = \frac{b}{M_{eff}}\left(2 - \frac{b}{M_{eff}}\right) \tag{5.4}$$

	Typical value	Uncertainty	$\left(\frac{\partial R_i}{\partial X_i}\frac{\partial X_i}{\partial Nu}\right)\cdot 100$
T_w	310 K	0.2 K	2.8
T_{aw}	293 K	0.2 K	2.7
T_a	293 K	0.1 K	1.4
I	63 A	1 % of reading	1.0
V	1.4 V	1 % of reading	1.0
ϵ	0.95	0.01	0.03
d	0.02 m	1 %	0.02
s	50 μm	1 %	10^{-5}
$\dot{q_{nc}}$	140 $\frac{W}{m^2}$	20 %	1.4
Error %			4.6

Table 5.1: Uncertainty analysis.

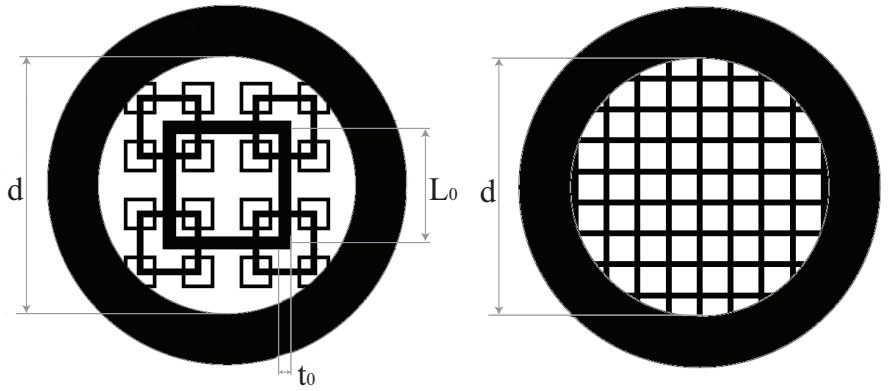

Figure 5.2: Sketch of the fractal insert (left) and of the regular grid (right).

with P and b being the grid perimeter's length and the bar thickness, respectively. The meshlength of the regular grid is equal to $2.4mm$, while the bar thickness is $0.4mm$.

The experiments are carried out at nominal Reynolds numbers equal to 16,000 and 28,700 (using the following expression based on the flow rate, $Re = \frac{4\dot{m}}{\pi\mu d}$). Considering that the presence of the insert and its position with respect to the nozzle exit have a significant influence on the pressure drop, the tests are conducted with the same power input, i.e. the product of the pressure drop and the volumetric flow rate is kept constant ($0.9mW$ and $4.6mW$ for the two cases, respectively). For this reason, the test Reynolds number is related to the reference case of fractal grid located at the exit section, i.e. $z = 0$ (referred to as nominal Reynolds number in the following), which corresponds to the case with the largest pressure drop and, consequently, the lowest flow rate within the data set of each test Reynolds number.

From this point on, comparison will always be performed at the same power input, i.e. same nominal Reynolds number, but the effective Reynolds number based on the flow rate and the jet diameter will be different. The effective Reynolds numbers of all the test cases are reported in the Tables 5.2, 5.3.

Table 5.2: Mass flow rate, pressure drop and Reynolds number for the test case with power input of $0.9mW$.

	JWT			Regular Grid			Fractal Grid		
	$\dot{m}(g/s)$	$\Delta p(N/m^2)$	Re	$\dot{m}(g/s)$	$\Delta p(N/m^2)$	Re	$\dot{m}(g/s)$	$\Delta p(N/m^2)$	Re
z/d=0	6.3	178	23,200	4.8	229	17,900	4.3	237	16,000
z/d=0.5				4.9	220	18,000	4.9	229	18,000
z/d=1				4.9	220	18,000	5.0	220	18,600

Table 5.3: Mass flow rate, pressure drop and Reynolds number for the test case with power input of $4.6mW$.

	JWT			Regular Grid			Fractal Grid		
	$\dot{m}(g/s)$	$\Delta p(N/m^2)$	Re	$\dot{m}(g/s)$	$\Delta p(N/m^2)$	Re	$\dot{m}(g/s)$	$\Delta p(N/m^2)$	Re
z/d=0	10.4	535	38,500	7.9	697	29,400	7.7	713	28,700
z/d=0.5				8.8	628	32,800	7.9	697	29,500
z/d=1				8.8	628	32,800	8.1	679	30,100

5.2 Results

5.2.1 Nusselt number distributions

In Figure 5.3 the convective heat transfer coefficient distributions, for the jet without turbulator (JWT), the Regular Grid (RG) and the Fractal Grid (FG) cases, are reported in non-dimensional form for power input of 4.6 mW, i.e. nominal Reynolds number equal to 28,700 (refer to Table 5.3 for the effective Reynolds number of the other cases).

The contour plots for the JWT are reported in Figure 5.3(a-c) for three nozzle-to-plate distances. The maps reveal a double-peak shape of the radial distribution of the Nusselt number, i.e. the convective heat transfer rate reaches a local minimum at the stagnation point; then it increases with the radial distance up to $r/d \approx 1$; again, the heat transfer rate decreases with the radial separation and reaches a second local minimum at $r/d \approx 1.5$. Beyond that point, it increases up to $r/d \approx 2$, where the Nusselt number achieves a local maximum; then, for larger radial separation, the heat transfer rate decreases monotonically. This pattern is a well-known feature for small nozzle-to-plate distances, and it is commonly addressed to the formation of ring vortices within the jet shear layer due to the entrainment in correspondence of the nozzle exit section. By looking at the Nusselt number values at the stagnation point reported in Figure 5.4 for an easier identification, an improvement in the heat transfer rate can be detected as the nozzle-to-plate distance increases. This effect should be visible up to distances of $Y/d = 7.5$ (see Viskanta, 1993, Jambunathan et al., 1992, O'Donovan and Murray, 2007), where the effect of turbulence enhancement is no longer capable to compensate for the decay of the jet velocity and, consequently, the Nusselt number in the stagnation point falls down rapidly.

The Nusselt number maps for the RG case are reported in the second row of Figure 5.3 (d-f). The axial symmetry in the heat transfer rate is perturbed by the regular insert, which acts similarly to a multi-channel.

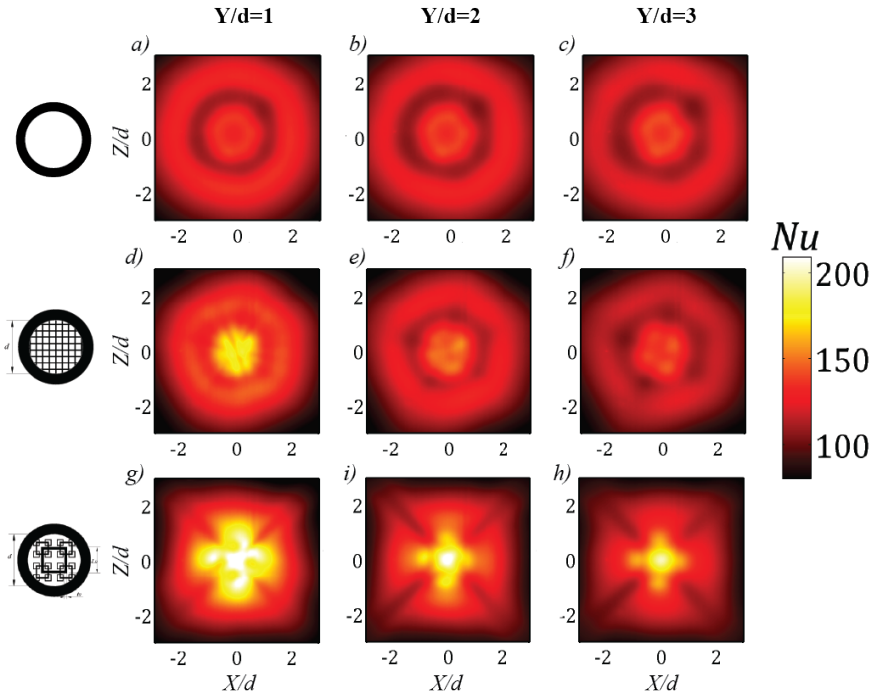

Figure 5.3: Nusselt number maps for the jet without turbulators (JWT, a to c), the regular grid (RG, d to f) and the fractal grid (FG, g to i). The test conditions are: nominal Reynolds number 28,700, grid located at the nozzle exit ($z/d = 0$). For the effective Reynolds number of JWT and RG please refer to Table 5.3.

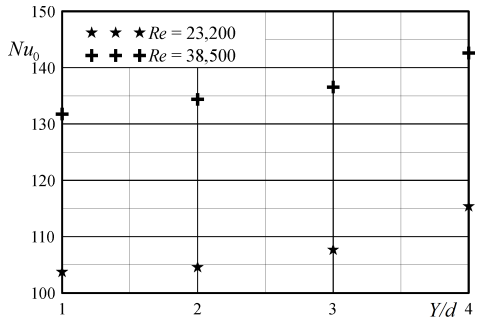

Figure 5.4: Nusselt number values at $r/d = 0$ for the JWT case.

The mesh print on the impinging surface can be envisaged on the maps. Moreover, the Nusselt number does not decrease as the radial distance increases; in fact, similarly to what observed in the JWT case, for small Y/d values at radial separation from the axis equal to about $r/d \approx 2$ the Nusselt number increases again attaining a second local maximum. On the other side, the behaviour result to be different from the JWT case as Y/d increases; the heat transfer rate result to be monotonically decreasing, as it will be shown in the next section, up to $Y/d = 3$.

The third row in Figure 5.3 (g-i) reports the Nusselt number maps for the FG case. The phenomenology is completely different from the previous cases. The contour plot reports a maximum value of the heat transfer rate located at the stagnation point that is much larger than the other cases; interestingly enough, the improvement in the heat transfer rate is mainly related to the central zone of the jet, whilst for larger radial separations from the jet axis, the Nusselt number values are quite similar to those of the JWT and RG cases. Furthermore, as already outlined for the RG case, local maxima are also present at a distance from the nozzle axis of about $1d$. However, the remarkable gap in the absolute heat transfer rate (even though the test Reynolds number of the RG is larger than that of the FG) spotlights relevant dissimilarities.

The striking difference might be addressed to the different turbulence-generation mechanism of fractal and regular grids. As already outlined in the numerical simulations by Laizet and Vassilicos (2011), the fractal generated turbulence enhances the scalar transfer according to a space-scale unfolding (SSU) mechanism, i.e. the wakes with different size generated by the fractal stirrer meet at different downstream locations. In this scenario an individual fluid particle might jump into a larger wake and experience an eddy turnover time larger than that of the original wake (see Laizet and Vassilicos, 2011 for a more exhausting treatment). This mechanism is absent in regular grids, where all the wakes have similar size and meet immediately beyond the grid; this yields to a more intense turbulence production in a short region confined in proximity of the grid, and a subsequent

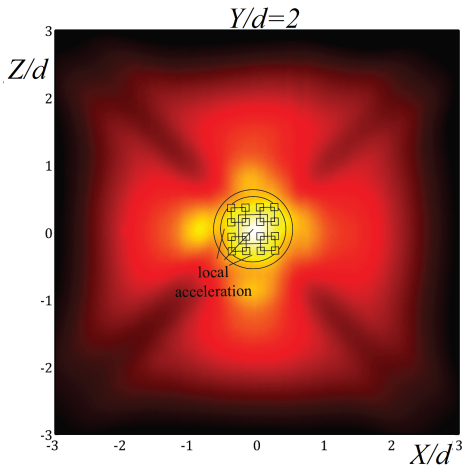

Figure 5.5: Qualitative representation of the effect of the fractal grid geometry on the Nusselt number distribution.

rapid decay. The strong confinement of the high turbulence intensity region of regular grids obstructs its usage for application purposes, while the geometry of fractal grids can be tuned to relocate the turbulence intensity peak, thus enabling its exploitation. The SSU would explain the high persistence of enhanced turbulent diffusion downstream of the grid, and, consequently, the higher heat transfer rate.

The qualitative sketch reported in Figure 5.5, in which the fractal grid is superimposed to the Nu map, might be helpful to highlight some interesting features of the Nusselt number distribution for the case of the jet with fractal insert. The stagnation region Nusselt number peak is related to the acceleration of the fluid issued through the largest square of the grid (i.e. the first fractal iteration). The jet velocity increases (as it experiences a sudden contraction) as well as the effective local Reynolds number, causing an improvement in the convective heat transfer efficiency. In the cited figure, this zone is identified by the tag local acceleration. This phenomenon is also present in correspondence of the holes between the squares of the second and third fractal iteration and the external skeleton of the insert,

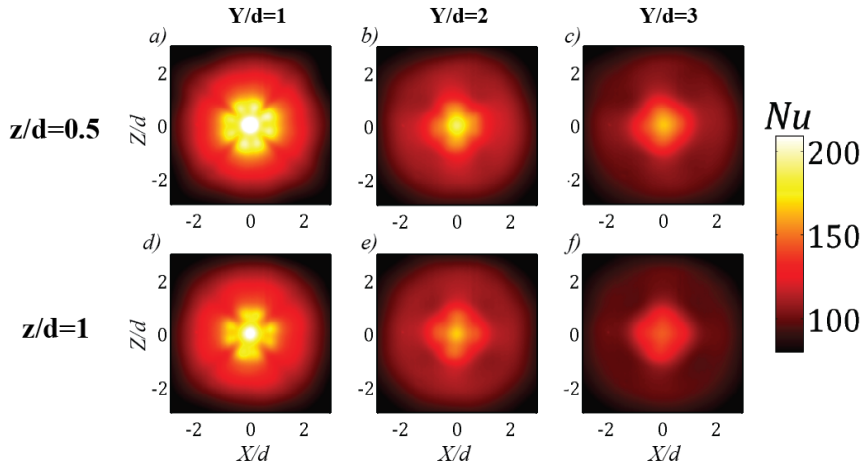

Figure 5.6: Nusselt number maps for the fractal grid (FG). The test conditions are: nominal Reynolds number 28,700, grid located at $0.5d$ (a, b, c) and $1d$ (d, e, f) from the nozzle exit section. For the effective Reynolds number of the test cases please refer to Table 5.3.

as indicated in the figure where other local maxima are present. In the wake of the smallest iterations, the heat transfer rate achieves lower values due to the locally higher blockage ratio. As the nozzle-to-plate distance increases (in Figure 5.3 at $Y/d = 3$) the outer peaks merge with the central maximum in the stagnation region, determining a cross-shaped Nu distribution. This interaction might be addressed to the turbulent diffusion, which at a sufficient streamwise distance is expected to smear out the wakes of the fractal iterations and the central jet.

In order to highlight the effect of the position of the grid insert with respect to the nozzle exit section, the Nusselt number distributions for inflow conditions with a nominal Reynolds number Re = 28,700 keeping the power constant input are reported in Figure 5.6 in the cases of grid located at $z = 0.5d$ and $z = 1d$ (see Table 5.3 for the corresponding values of the effective Reynolds number). The phenomenology sensibly varies as the insert is moved upstream in the nozzle. Indeed, the presence of the

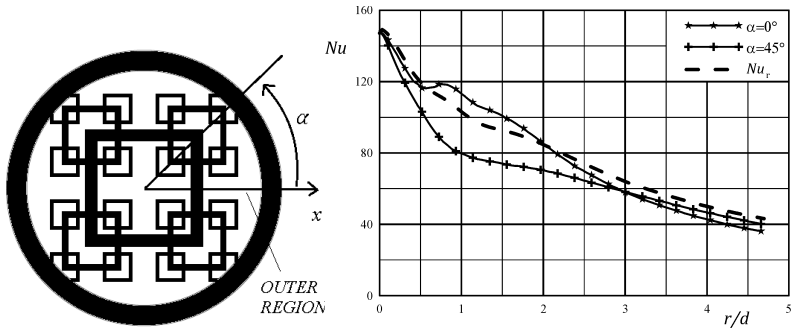

(a) (b)

Figure 5.7: Polar reference system (left) and Nusselt number distribution (right) for the FG case; Re = 28,700, $z/d = 0$, $Y/d = 2$. The dashed line represents the azimuthal average.

straight tube mitigates the efficiency of the grid in producing turbulence. In particular, two effects are clearly visible looking at the maps of Figure 5.3 and 5.6: first, as it will be better illustrated in paragraph 5.2.2, for small nozzle to plate separations, the Nusselt number in the stagnation region is quite similar for the three cases (see Figure 5.3g and Figure 5.6a and d). This feature might be addressed to the progressive enhancement of the heat transfer rate that may be achieved as the nozzle-to-plate distance approaches the distance where the turbulence generated by the fractal stirrer would be at a maximum in free shear conditions (see paragraph 5.2.2 for further details). This element is even more interesting considering that the pressure drop due to the presence of the fractal insert progressively decreases as the grid is moved within the nozzle (see Tables 5.2, 5.3). Moreover, although the nozzle exit section to plate distance does not vary with respect to the case of a grid set at the nozzle exit section, differently from the case of Figure 5.3 (g-i), the mixing of the stagnation region with the outer maxima occurs at lower values of Y/d (in both cases, $Y/d < 2$).

In order to better illustrate the feature of the non-axial-symmetric Nusselt number distribution of jets with fractal grids, the Nusselt num-

ber profiles at $\alpha = 0^o, 45^o$(where α is the angle between one of the two axis of symmetry directed as the square sides of the FG, named X axis, and the generic direction in a polar system) obtained by averaging the 1000 realizations over time (solid lines) are reported in Figure 5.7; the azimuthal average (Nu_r, dashed line) of the Nusselt number distribution is also plotted for clarity. It is evident that the second maximum in the Nusselt number distribution is only present along the $\alpha = 0^o$ direction. This region corresponds to the one contained between the outer iterations and the external circle (labelled as outer region in Figure 5.7, left), where the issuing jet experiences a sudden acceleration. Along the $\alpha = 45^o$ direction the profile results to be monotonically decreasing and this reflects also in the azimuthal average, where the effect of the acceleration through the external regions is smeared out by the average operation.

5.2.2 Nusselt number profiles

In this section, the effect of the main parameters influencing the convective heat transfer rate will be analysed in terms of $\overline{Nu}(r)$. The following parameters will be considered as reference conditions:

- $Y/d = 2$;
- Nominal $Re = 28,700$;
- $z/d = 0$

In each subsection the effect of each single item will be discussed in order to isolate the respective influence on the Nusselt number distribution, while the other two parameters will be kept constant at the reference condition.

Effect of the nozzle to plate distance (Y/d)

In Figure 5.8 the profiles of the spatially averaged Nusselt number (Eq. 5.1) are plotted as a function of the radial distance; plots are reported for $Y/d = \{1, 2, 3, 4\}$. The behaviour of the fractal insert is quite different from

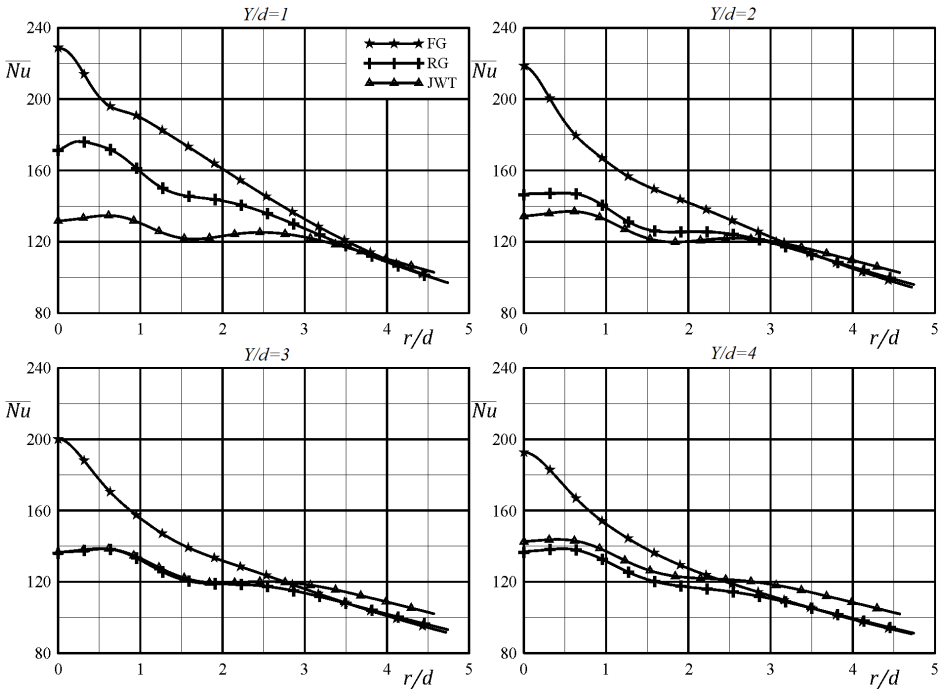

Figure 5.8: Nusselt number distribution for nominal Reynolds number, Re= 28,700; $z/d = 0$, $Y/d = \{1, 2, 3, 4\}$ and constant value of the power input equal to $4.6mW$ (see Table 5.3 for the effective Reynolds number values).

both the JWT and the regular grid. Indeed, for the FG case the convective heat transfer rate at the stagnation point monotonically decreases with the nozzle to plate distance. This is not true in the case of the JWT: as already outlined in paragraph 5.2.1 (see Figure 5.4). For the RG, especially for larger nozzle-exit to plate distances, there is the clear presence of a maximum in the radial distribution at $r/d \approx 0.4$ for $z/d = 0$. Actually, as outlined in Figure 5.6, a double-peak shape can be observed also in some Nusselt number radial profiles for the case of the fractal grids; however, this effect occurs at small radial separation from the jet axis ($r/D \approx 0.75$), and it has reasonably addressed by the defect of velocity in the wake of the largest fractal iteration. Furthermore, when integrated over an area, as in Figure 5.8, this effect is on average deleted.

Interestingly enough, the gap between the FG and the other elements decreases as Y/d increases; in other words, the fractal insert is more efficient in the case of small distances. One possible interpretation of this aspect might be addressed to the peculiar features of the mechanism of turbulence generation and decay of fractal grids. In fact, looking at Figure 4.9 it is possible to see that in the case of free (i.e. without impinging plate) submerged jet, the turbulence intensity level builds up until $Y/d \approx 1.6$. Beyond that point, a nearly constant value of the turbulence intensity level can be found, up to $Y/d \approx 2.2$, where the penetrating shear layer causes a further increment in the turbulence intensity level on the jet centreline.

Up to this streamwise distance, the combined effect of high axial velocity and turbulence intensity level causes the strong enhancement of convective heat transfer rate. However, beyond $Y/d \approx 3$ the increment in terms of convective heat transfer experienced using the FG drops down, due to the fact that the turbulence intensity is not capable to compensate the reduction in the impinging velocity.

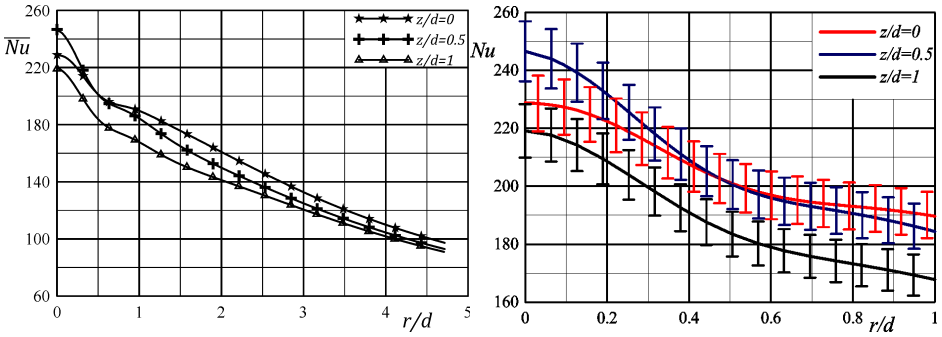

(a) (b)

Figure 5.9: Nusselt number distribution for the FG case at three locations of the grid within the nozzle $z/d = \{0, 0.5, 1\}$ (left) and zoom up to $r/d = 1$(right) with error bars; the nozzle exit-section to plate distance is set to $h/d = 1$; the nominal Reynolds number is 28,700 (see Table 5.3 for the effective Reynolds number values of the other cases).

Effect of the position of the grid insert within the nozzle (z/d)

The spatially averaged Nusselt number profiles are illustrated in Figure 5.9 for the three tested locations of the insert within the nozzle. For the same value of the power input, the highest value of the heat transfer rate can be detected at the stagnation region when the grid is located at $z/d = 0.5$. As remarked before, this effect might be due to the fact that the maximum turbulence intensity is achieved for $(Y + z)/d \approx 1.5$ for the present case of impinging jet.

When this distance increases, the turbulence produced by the grid is lower and consequently the heat transfer efficiency decreases as well. However, it has to be pointed out that this effect is characteristic of the stagnation region; in fact, for $r/d > 1$, although very similar values are measured, the configuration with the grid set at the nozzle exit section reveals it to be the most efficient. Finally, the Nusselt number profiles for $z/d = 0.5, 1$ result practically coincident for $r/d > 3.5$, i.e. in the wall jet region.

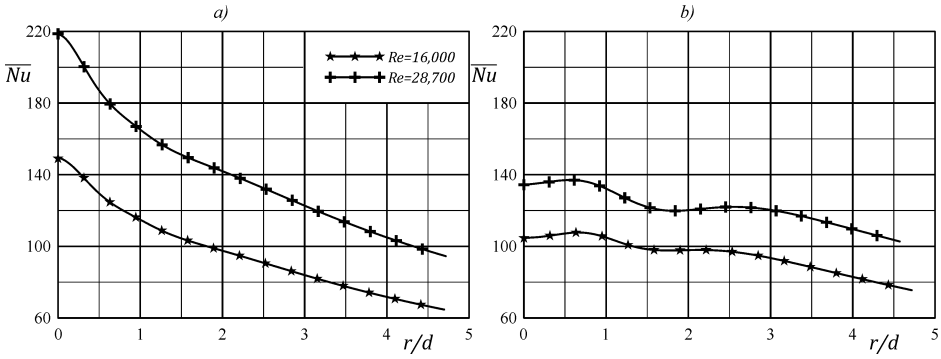

Figure 5.10: Nusselt number distribution for the FG (a) and JWT (b) cases at two different nominal Reynolds numbers: Re = 16,000, 28,700 (for the JWT the effective Reynolds numbers are Re = 23,200, 38,500) and constant values of the power input equal to 0.9mW and $4.6mW$.

Considering that in the case of $z/d = 0.5$ the achievable heat transfer rate is larger than the other cases at least for small nozzle to plate separations, it can be speculated that the enhancement due to fractal stirrers could mainly be addressed to the higher turbulence intensity rather than the more intense local peaks in the jet velocity profile (which are expected to be stronger in the case of $z/d = 0$).

Effect of the Reynolds number (Re)

As already outlined in the previous sections, two different nominal Reynolds number have been tested. Figure 5.10a (left) reports the Nusselt number profiles for the FG case with $Y/d = 2$ and $z/d = 0$ (grid placed at the nozzle exit). The increment that is expected as a consequence of the higher upstream Reynolds number reflects on the Nusselt number profiles; in fact, concerning the local maxima, which occur in correspondence of the jet axis, a significant increment can be detected. Considering the correlations available in the literature (see Meola et al., 1996 for a review), an increment of the stagnation point Nusselt number of about 42% would

Table 5.4: Mean Nusselt number increment of the FG and RG cases with respect to the JWT case at four different nozzle to plate distances and three different radial locations; the test conditions are: nominal $Re = 28,700$ and $z/d = 0$ (for the effective Reynolds number see Table 5.3).

Y/d	Grid	$\Delta\overline{Nu}(r/d=0)\%$	$\Delta\overline{Nu}(r/d=1)\%$	$\Delta\overline{Nu}(r/d=2)\%$
1	FG	74	45	33
	RG	29	23	17
2	FG	63	25	19
	RG	9	6	5
3	FG	46	17	11
	RG	-1	-1	-1
4	FG	35	11	5
	RG	-4	-4	-4

be expectable. An improvement of 48% is measured, thus leading to the conclusion that the dependence of the Nusselt number on the Reynolds number is, taking into account also the measurement error, at least equal to the one reported in the literature. On the other hand, by analyzing the profiles for the JWT case (Figure 5.10b, right), for an expected improvement of about 35% (considering that the corresponding Reynolds numbers for the JWT cases are respectively 23,200 and 38,500), an enhancement of about 31% is measured.

In conclusion, the FG results to be more efficient than the JWT for both the tested power input conditions. In both cases, the effect of injecting turbulence within the jet shear layer causes an heat transfer that is much more efficient than the one achievable with a jet without turbulence generator.

5.3 Global considerations

The percentage increments in the Nusselt number obtained for the FG and RG cases with respect to the JWT under the same power input are

Table 5.5: Heat transfer rate enhancement at three radial locations $\left(r/d = \{0, 1, 2\}\right)$ using the fractal insert at three different locations within the nozzle $z/d = \{0, 0.5, 1\}$; data in the brackets refer to a different nominal Reynolds number ($Re = 16,800$).

Y/d	z/d	$\Delta\overline{Nu}(r/d = 0)\%$	$\Delta\overline{Nu}(r/d = 1)\%$	$\Delta\overline{Nu}(r/d = 2)\%$
1	0	74 (48)	45 (22)	33 (7)
	0.5	87 (56)	41 (18)	22 (-1)
	1	66 (50)	23 (12)	15 (-4)
2	0	63 (42)	25 (10)	19 (0.3)
	0.5	41 (31)	14 (2)	5 (-10)
	1	24 (26)	8 (2)	1 (-10)
3	0	46 (28)	17 (3)	11 (-4)
	0.5	21 (11)	5 (-7)	-2 (-14)
	1	6 (7)	-3 (-6)	-8 (-13)
4	0	35 (16)	11 (-3)	5 (-7)
	0.5	8 (-3)	-3 (-12)	-9 (-16)
	1	3 (-7)	-9 (-13)	-13 (-20)

reported in Table 5.4 ($Re = 28,700$, insert placed at the exit section, thus $z/d = 0$).

The fractal inserts are extremely efficient turbulence promoters at small nozzle-to-plate distance. Indeed, for $Y/d = 2$ the improvement in the stagnation region is always greater than 63%, while the regular grid never achieves value beyond 9%. The heat transfer enhancement of the fractal grid drops down significantly for larger nozzle-to-plate distances, but it is still quite appealing (35% at the stagnation region for $Y/d = 4$, while for the regular grid the performances are even worse than the JWT under the same power input). The heat transfer rate decay might be addressed both to the fast decay of the turbulent kinetic energy generated by the fractal stirrer and to the spreading of the jet, which smears out the jet velocity peaks generated by the uneven distributed blockage ratio.

From the local heat transfer enhancement standpoint, fractal grids are extremely promising. On the other hand, the area-averaged heat transfer rate significantly reduces with the radial distance from the jet. However, for $Y/d \geq 3$, the heat transfer rate achieved with a regular insert is always equal or less than that of the JWT under the same power input, while the advantage of using a fractal grid still persists for the shown radial distances.

In Table 5.5 the effects of the Reynolds number and of the position of the fractal grid on the heat transfer enhancement are revised. At small distances, it is very interesting to notice that in the stagnation region an improvement in the heat transfer rate is detectable when the grid is set at $z/d = 1$. However, as either the radial distance or the separation between the nozzle exit section and the plate increases, placing the grid inside the nozzle reduces significantly the enhancement. As expected, the rapid drop due to the fast turbulence intensity decay is already very significant at $Y/d \geq 2$ when the insert is at $z/d = 1$. This is due to the larger distance of the turbulator with respect to the plate. Furthermore, when $z/d = 1$ the flow passes through a short pipe segment, which contributes in smearing out the velocity gradients and consequently the local accelerations that

might be responsible for the heat transfer enhancement.

A lower Reynolds number (data in brackets in Table 5.5) significantly reduces the stagnation point heat transfer enhancement at small nozzle-to-plate distances. This might be related to the different size of the wakes of the fractal iterations and/or the size of the turbulent eddies contained within them.

The outcome of the present analysis is that within the inspected range of Reynolds numbers, the fractal insert is more efficient than the JWT under the same power input. Moreover, when the interest relies in the local enhancement of the heat transfer, positioning the grid within the nozzle carries two benefits: an improvement in the maximum heat transfer and a lower pressure drop. Nevertheless, this aspect exasperates the non-uniformity of the radial distribution of the Nusselt number.

CHAPTER 6

Flow field topology of a fractal impinging jet

In the previous Chapter the astonishing performances of the fractal grids in terms of convective heat transfer enhancement have been presented. Here, the fluid dynamic mechanism that leads to such a behaviour is investigated by means of tomographic PIV in the case of relatively short nozzle to plate distance ($Y/d = 2$). Furthermore the effect of the presence of the impinging plate onto the flow field organization is discussed by comparison with the case presented in Chapter 4.

6.1 Experimental apparatus

The experiments are carried out in the air jet facility at the University of Naples Federico II already described in Chapter 4. To avoid redundancy in the description, only the main differences will be spotted here, with the support of the sketch reported in Figure 6.1a-b.

A glass square impinging plate is located at a fixed distance $Y = 2d$ from the nozzle exit section. The size of the glass plate ($15d$ x $15d$) is chosen so that boundary effects on the flow field are negligible. The correct

positioning of the impinging plate is regulated by means of the traversing system, which ensures an accuracy of $1/20d$.

The flow is seeded with olive oil particles (about $1\mu m$ diameter) generated by a Laskin nozzle. The mixing between the working fluid and the seeding particles occurs in a reservoir located upstream of the stagnation chamber.

The light source is a Quantel Evergreen laser ($532nm$ wavelength, $200mJ/pulse$, $< 10ns$ pulse duration) with an exit beam diameter of about $5mm$. The laser beam is enlarged using a bi-concave lens with negative focal length ($-50mm$); it is then adjusted in thickness using a second bi-convex lens with positive focal length ($200mm$), in order to ensure a uniform illumination across the volume; a pinhole is used in order to cut the peripheral regions of the laser beam. Finally a cylindrical lens (focal length $100mm$) enlarges the laser in the plane orthogonal to the optical axis of the camera. The correct illuminated volume dimension is set by means of a knife edged mask. The Tomo-PIV imaging system is made of four Andor Zyla sCMOS 5.5Mpixels cameras, placed as schematically represented in Figure 6.1. The angle between the outer cameras, namely between 1 and 4, is about 60 deg. The cameras are equipped with 100mm Tokina objectives, with focal aperture set to $f_{\#} = 16$. Home-made mounts are used to set the objective so that the Scheimpflug condition is respected.

Owing to the high spatial/dynamic range required by the challenging flow field, three different Tomographic PIV experiments are performed. Two of them are devoted to the characterization of the streamwise organization of the flow field; the imaged area is about equal to $2d$ in the axial direction (Y), $2.5d$ in the X direction and $0.45d$ in the Z direction. With this configuration, two different volumes are investigated: the first one is oriented such that the grid symmetry plane ($Z/d = 0$) is in the center of the illuminated region; a second one is obtained by rotating the grid within the cap of an angle equal to 45 deg. In this configuration the laser volume is shifted by $0.2d$ with respect to the grid diagonal in the Z_{45} direction. In the following, these two sets of experiments will be referred

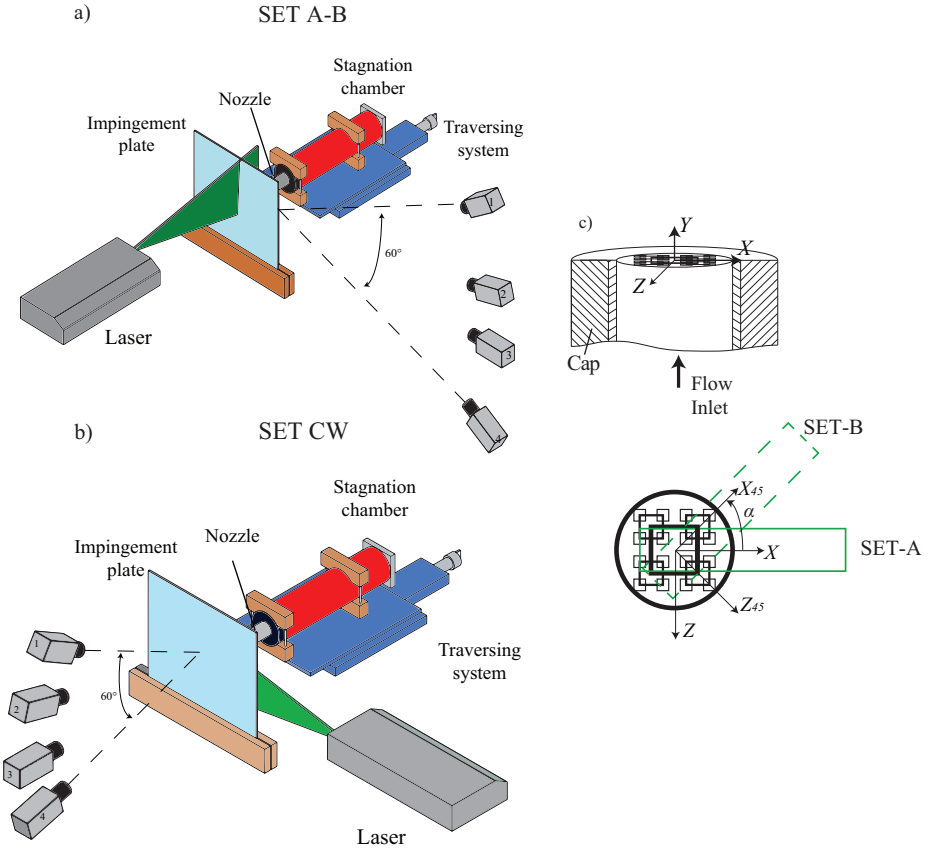

Figure 6.1: Schematic description of the experimental apparatus for the SET A-B a) and the SET CW b). Detail of the grid located at the nozzle exit section with indication of the measurement volume for the SET A-B cases c).

to as SET-A and SET-B respectively. The last Tomo-PIV experiment is instead devoted to the analysis of the near wall behaviour of the flow field. In this case the imaged area is about $2d$ x $0.45d$ x $2d$, covering a region that goes in the axial direction between $1.55 < Y/d < 2$.

The acquisition frequency is set to 15 Hz. The flow rate is regulated using the rotameter in order to obtain a Reynolds number (based on the nozzle exit section diameter d) equal to $Re = 15,000$. The resulting bulk velocity is then $V_j = 10.5m/s$. This will be the value used to normalize all the quantities in the following.

Similarly to what already done in Chapter 4, the calibration procedure is performed by recording images of a target (black dots on white background, $5mm$ pitch) moved through the measurement volume; the span of the measurement volume is operated by means of a micrometric stage. The target images are taken in correspondence of seven equally spaced locations along the direction orthogonal to the target plane. The mapping function is obtained using the pinhole camera model, as suggested by Tsai (1987). The resulting maximum calibration error is of the order of 0.5 pixels. A self-calibration procedure (Wieneke, 2008, Discetti and Astarita, 2014) is then carried out in order to further correct the location of the laser volume using the scattering particles and to reduce reciprocal misalignments of the cameras. This leads to a reduction of the calibration error down to 0.03 pixels.

A pre-processing is applied to the raw images in order to reduce the background noise. The pre-processing consists in: temporal minimum image subtraction, in order to limit the effect of laser reflections within the flow field (especially associated to the presence of the impinged plate); a sliding minimum subtraction over a kernel of [7 x 7] pixels.

The reconstruction algorithm used for all the three experiments is the same. The 3D volume is reconstructed from the pre-processed images using four C-SMART iterations on a binned volume (Discetti and Astarita, 2012b), three C-SMART iterations on the full volume, one MTE iteration (Novara et al., 2010) aimed to detect and remove the ghost particles gen-

erated during the reconstruction process, 3 further C-SMART iterations on the full volume, and finally one SMART iteration. During the iterative reconstruction with C-SMART, a non-isotropic Gaussian smoothing is applied on a [3 x 3 x 1] kernel (Spatial filtering improved tomography, Discetti et al., 2013) in order to reduce the artifacts of the reconstruction due to particles' elongation along the depth direction in the reconstructed volumes. In order to check the quality of the reconstruction, the signal to noise ratio defined as the reconstructed particles intensity inside the illuminated region (true particles + ghost particles) versus that reconstructed outside (ghost particles) is calculated. In the present experiment, the intensity of the laser is uniformly distributed across the volume which extends in depth in the SET-A/B for about 400 voxels whilst 450 voxels for the SET-CW. The S/N ratio results to be larger than 2.5, which is a typical value for a good reconstruction (Scarano, 2013).

In the SET A-B, the reconstructed volume is interrogated using a 3D cross-correlation algorithm based on a final interrogation volume of 64 x 64 x 64 voxels (1.6 x 1.6 x 1.6 mm^3), 75% overlap. The resulting vector pitch is $0.4mm$. In the SET-CW, being the digital resolution slightly better than the former cases, the same interrogation volume is used, then corresponding to a 1.32 x 1.32 x 1.32 mm^3 spot and a vector pitch of 0.32 mm. The cross correlation process is performed with an efficient algorithm based on sparse matrices and minimization of redundant calculations when using overlapping windows (Discetti and Astarita, 2012a).

6.2 Flow field topology

6.2.1 Mean Flow field

The mean flow field obtained by averaging 1000 instantaneous realizations for the SET A-B (see section 6.1, Figure 6.1) is reported in Figure 6.2. The iso-surface of axial velocity $V/V_j = 1.2$ is reported in orange. The introduction of the grid strongly affects the flow field with respect to

the widely studied round jet without turbulator (JWT) case. Five jets issue through the grid iterations' holes (referring to the insert in Figure 6.2, regions A, B-B' and C-C'), thus leading to a multichannel behaviour of the jet. It is worth to explicitly notice that, since the measured region is comprehensive of only a portion of the nozzle cross section, only the jets issuing through region A and B are detected and illustrated in Figure 6.2. Furthermore, a weaker jet issuing through the secondary grid iterations, labelled as secondary jet, can be also seen. Beyond $Y/d \approx 1$, the presence of the impinged plate causes a strong reduction in the jet axial velocity. In addition to that, the outer jets spread as they progressively approach the wall. This behaviour has already been argued in Chapter 5: indeed, the scalar transfer is strongly dependent on the velocity module near the impinged plate. The five impinging jets cause the presence of the five maxima in the Nusselt number distribution, previously defined as local accelerations (see Figure 6.3), respectively in correspondence of the wall print of the regions A, B, B', C and C' as reported in the insert of Figure 6.2.

Near the impinged wall, the module of the radial velocity $V_r = \sqrt{U^2 + W^2} = 0.5$ normalized with respect to the bulk velocity is also reported in Figure 6.2 along with the representation of the velocity profiles in the developing region of the wall jet. It is interesting to notice that the developing wall jet thickness is different depending on the azimuthal coordinate α. Indeed, in a similar fashion to what happens for cross-shaped jets (Rau et al., 2014), along the diagonals of the central iteration the wall jet is thicker, whilst there is a defect of mass along the other directions. In order to give a direct grasp of the dependence of the flow rate on the azimuthal coordinate α, in Figure 6.4 are reported the normalized Q profiles (per unit angle) in the FG and FG-45 cases calculated as:

$$Q = \frac{1}{(\alpha_2 - \alpha_1)} \int_0^{y/d} \int_{\alpha_1}^{\alpha_2} r \cdot V_r / V_j \, \mathrm{d}\alpha' \mathrm{d}y' \tag{6.1}$$

The integration area A is the cross section having normal X in the FG case,

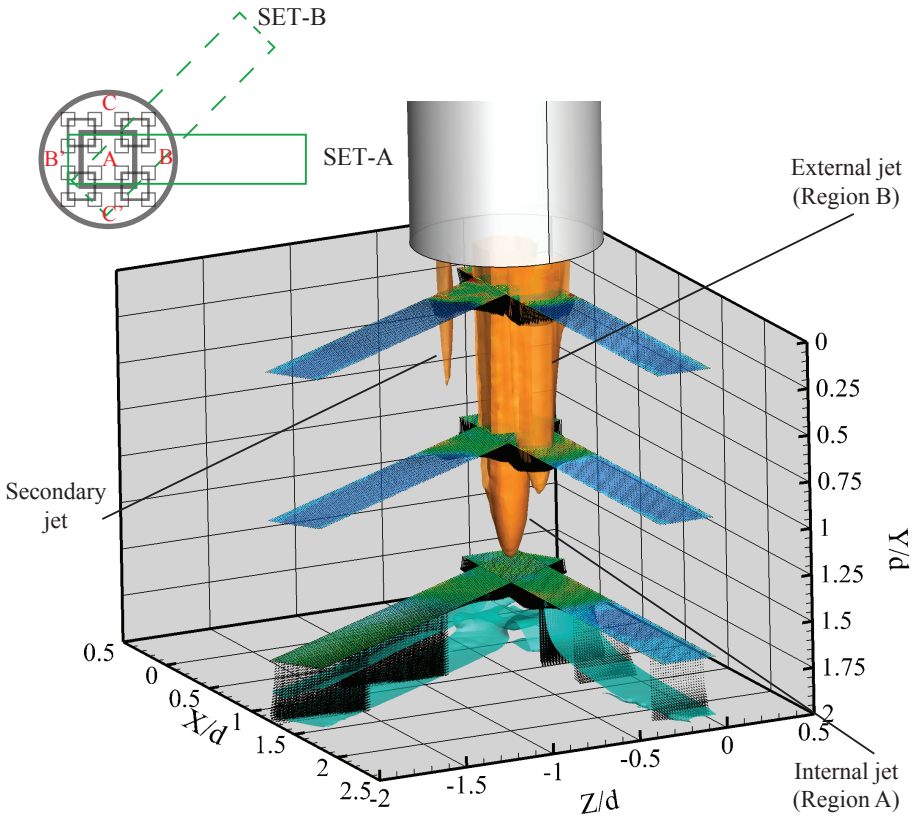

Figure 6.2: Isosurface of axial velocity $V/V_j = 1.2$ (in orange); isosurface of the velocity module in the XZ plane $V_r/V_j = 0.5$ (cyan); Contour representation of the axial velocity fluctuations at $Y/d = \{0.2; 1; 1.75\}$; vector representation in the wall jet region along the directions $\alpha = 0$ and $\alpha = 45$.

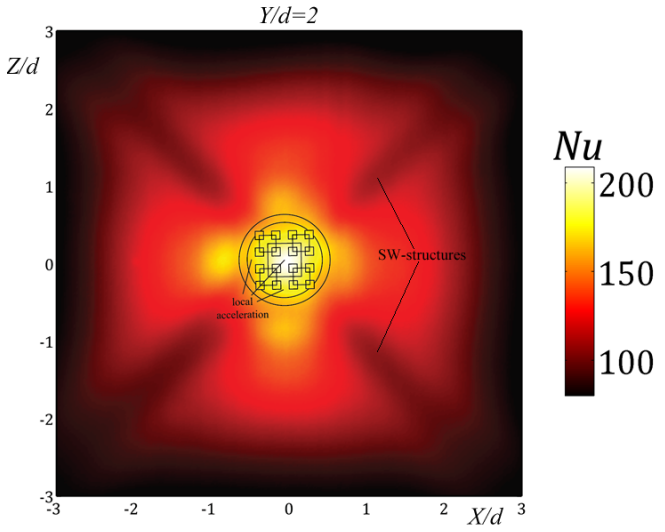

Figure 6.3: Nusselt number distribution at $Y/d = 2$ and $Re = 16,000$. Data from Figure 5.5.

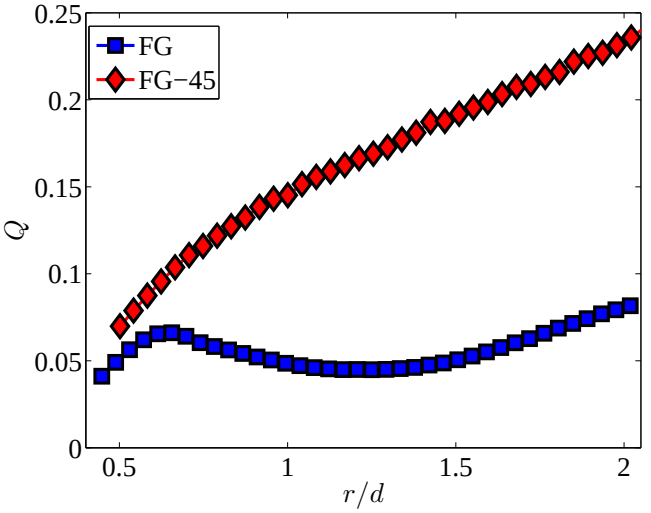

Figure 6.4: Mean flow rate in the developing wall jet region ($r/d > 0.4$) as a function of the radial coordinate $r = \sqrt{X^2 + Z^2}$ in the FG and FG-45 cases.

whilst X_{45} in the FG-45 case and it is chosen such that the subtended area is the same in both cases; V_r is representative of the radial velocity component. However, looking at the Nusselt number contour representations reported in Figure 6.3, a striking difference can be spotted with respect to the cross jet case. In fact, in the present case, along the $\alpha = \pm 45$ directions, the map presents a region of minimum. Thus, although the defect of mass produced in the vicinity of the nozzle exit section by the grid iterations leads to an increment of the mass flux along the X_{45} direction, this is not followed by an increment of the convective heat transfer rate. This element must be addressed to the generation of couples of counter-rotating vortices that cause an upwash in these regions and a corresponding reduction of the scalar transfer.

In order to better describe the mean flow field features, the velocity profiles extracted in the planes $Z/d = 0$ and $Z_{45}/d = 0$, which will be referred to as FG and FG-45 in the following, are reported in Figure 6.5. For the sake of understanding, it is here recalled that the non-dimensional axial coordinate Y/d runs from the nozzle exit section up to the impinged plate (at $Y/d = 2$).

As already qualitatively observed, at short distances from the nozzle exit section, it is possible to notice that the jet behaves in a multichannel fashion. In fact, a strong jet is issuing both through the central iteration and the outer grid iterations, namely regions A and B as indicated in the schematic representation reported in Figure 6.2. This feature is still present in the FG case at $Y/d = 1$, whilst the effect of the turbulent diffusion has already smeared out the smaller jets in the FG-45 case. Up to this location, the flow field is practically identical to the one presented in Chapter 4 in the case of free submerged jet. It is also possible to see that, both in the FG and FG-45 cases, non-zero values of radial and azimuthal velocity can also be detected at short nozzle to plate distances. This element is mainly related to the presence of quasi-steady streamwise vortices generated by the local curvature of the jet shear layer (Grinstein and DeVore, 2014), which introduce a local swirl component onto the mean flow field.

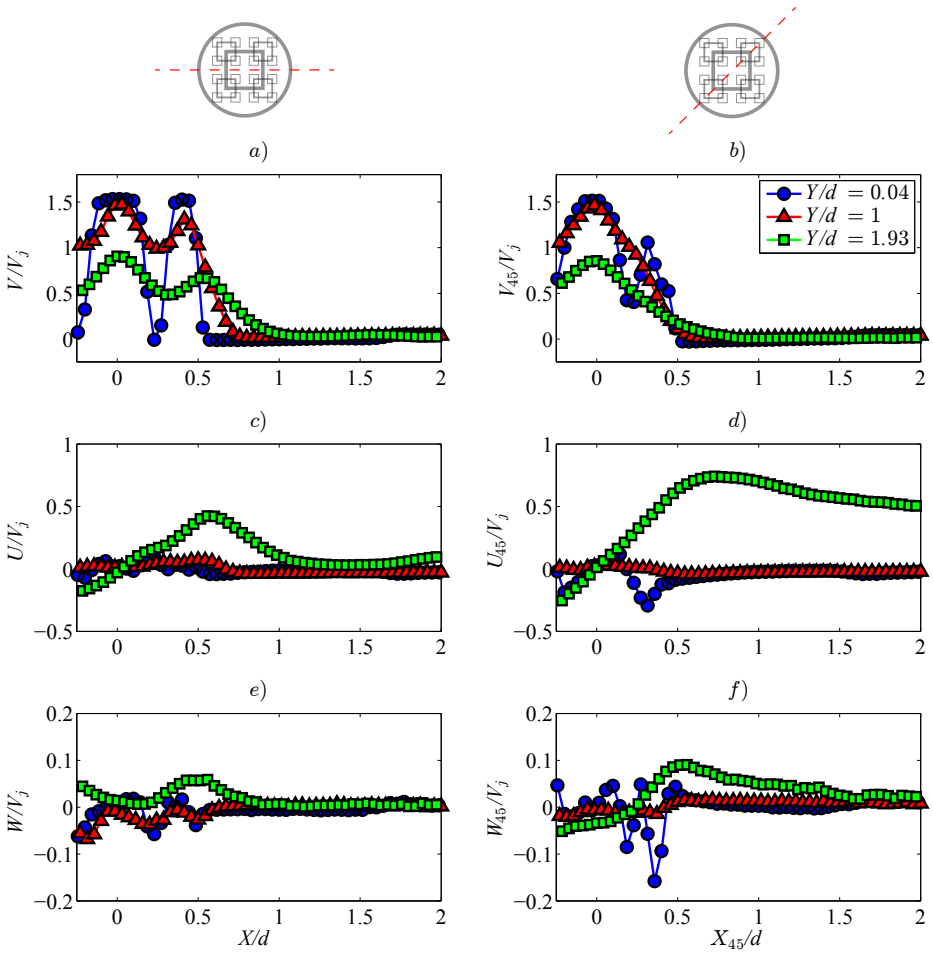

Figure 6.5: Axial V/V_j, radial U/V_j (U_{45}/V_j) and azimuthal W/V_j (W_{45}/V_j) velocity components in the FG (a, c, e) (FG-45 (b, d, f)) case. Markers are plotted every 3 measured points.

Beyond $Y/d \approx 1$, the effect of the adverse pressure gradient caused by the presence of the impinged plate turns into a strong reduction of the axial velocity. As the fluid approaches the impinged wall the momentum is transferred from the axial to the radial component (see Figure 6.5 c-e). Interestingly enough, at the same distance from the impinged plate, $Y/d = 1.93$, the values of radial velocity are quite different for the FG and FG-45 cases. This element, as already qualitatively presented when discussing Figure 6.2, is due to the fact that, when approaching the impinged plate, the jet experiences an axis-switching like behaviour, as characteristic for cross-shaped jets (Rau et al., 2014); a larger momentum is in fact convected along the FG-45 direction, thus leading to a thicker wall jet in this region than in the FG direction.

In the vicinity of the target plate, the presence of non-zero values of the azimuthal velocity component along the X_{45} direction can be retrieved. This element must be addressed to the presence of counter rotating wall vortices that generate along this direction, differently from what happens along the X direction where the W values are nearly zero.

The root mean square (rms) of the axial, radial and azimuthal velocity fluctuations respectively for the FG (a, c, e) and FG-45 (b, d, f) cases are plotted in Figure 6.6 as a function of the radial position for three different streamwise locations $Y/d = \{0.04; 1; 1.93\}$. Regarding the axial and radial components, in the vicinity of the nozzle exit section along the FG direction, the flow is dominated by the spreading wake that detaches from the central grid bar iteration. Indeed, the presence of a maximum at $X/d \approx 0.25$ can be detected. The w profile is also characterized by a maximum in correspondence of the central grid bar; however, it arises as a consequence of the presence of streamwise vortices that introduce a fluctuating azimuthal component into the flow field.

In the FG-45 case, the behaviour is quite similar. The extent of the region interested by a high value of the rms velocity results to be larger since in this case, they must be addressed to the concurrent effect also of the second and third grid iteration onto the flow field. In fact, the passage

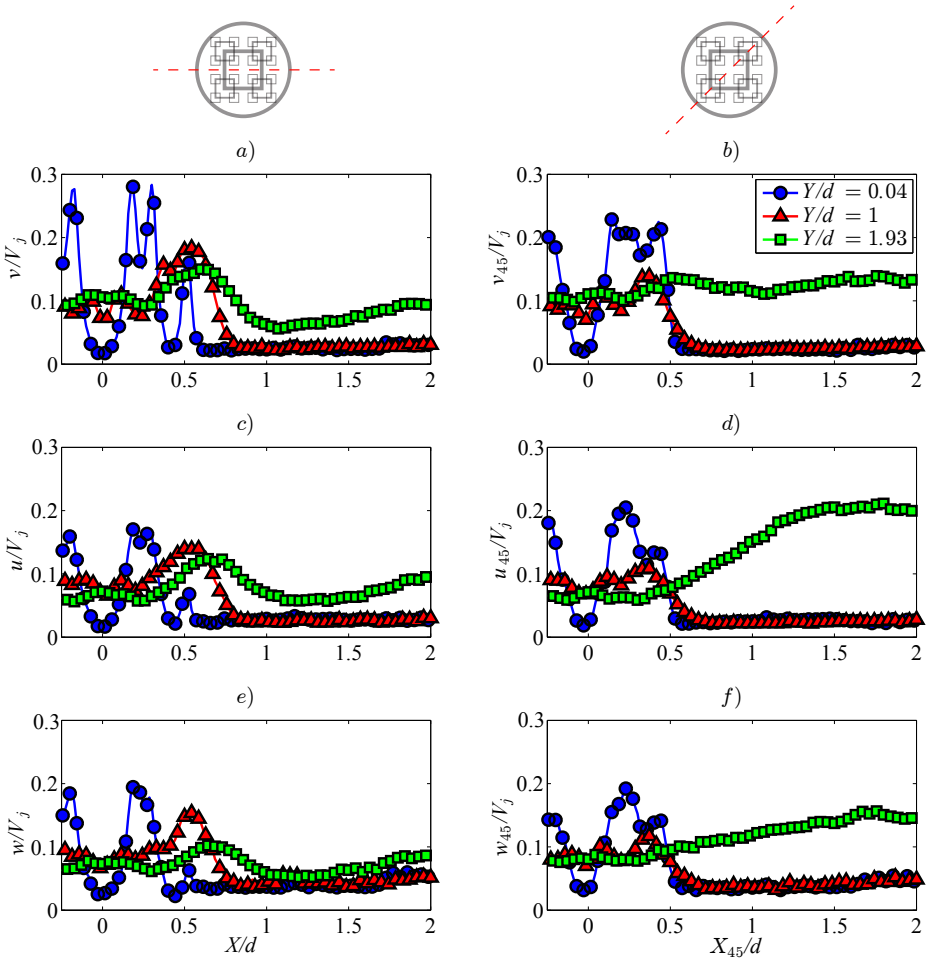

Figure 6.6: Axial v/V_j, radial u/V_j (u_{45}/V_j) and azimuthal w/V_j (w_{45}/V_j) rms velocity fluctuations in the FG (a, c, e) (FG-45 (b, d, f)) case. Markers are plotted every 3 measured points.

area of these iterations is small enough to create a blockage for the fluid issuing through the nozzle, thus leading to a wake-like behaviour also in this plane. However, a local minimum can be retrieved at $X_{45}/d \approx 0.45$, which must be associated to the presence of a region of high axial velocity issuing through the second grid iteration (secondary jet, see Figure 6.2).

Moving farther from the nozzle exit section, the effect of the growing shear layer on the wake spreading can be detected. In fact, at $Y/d = 1$, the axial and radial velocity rms fluctuations are characterized by large values in correspondence of the penetrating shear layer at $X/d = 0.55$ and then progressively reduce as X/d decreases. This effect is more limited along the FG-45 direction, although a small asymmetry can be still appreciated.

Beyond $Y/d = 1$ the effect of the impinged plate introduces strong variations in the flow field. Indeed, owing to the pressure gradient introduced by the plate, the axial velocity progressively decreases down to zero in correspondence of the nozzle axis, at $X/d = 0$. In the near vicinity of this point, a quasi-stagnation region is present, where the flow from one side is decelerated and from the other transmits the axial momentum in its radial component. As a consequence, this region is characterized by relatively high values of the rms velocity fluctuations. Moving farther from the nozzle axis, but still in the quasi stagnation region (Carlomagno and Ianiro, 2014), a second maximum can be detected at $X/d \approx 0.6$, which must be addressed to the impinging jet shear layer. When approaching the developing wall jet region, the boundary layer of the wall jet starts to spread in width, thus for $X/d \approx 2$, an increase in the rms velocity fluctuations is experienced. Along the FG-45 direction, most of the already outlined features can be retrieved. However, it is interesting to notice that this region is characterized by larger fluctuations values. This aspect has to be addressed to the passage of quasi-ring vortices that are generated within the jet shear layer. Although these structures are present both along the FG and FG-45 directions, the larger fluctuation values in the latter case are associated to the fact that the average distance of the vortex from the wall is larger than the former case.

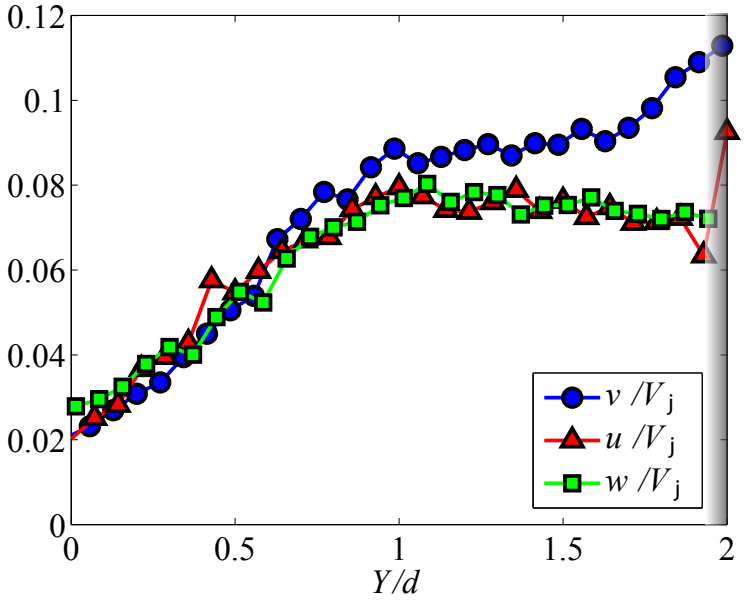

Figure 6.7: Streamwise organization of u/V_j, v/V_j and w/V_j along the nozzle axis. Data in the shadowed region (from Y/d=1.95 up to the impinged wall) are affected by larger uncertainties due to the glass reflection. Markers are plotted every 3 measured points.

The streamwise organization of u/V_j, v/V_j and w/V_j rms velocity fluctuations components along the jet centreline is reported in Figure 6.7. The profiles resemble those widely described into the literature (Hurst and Vassilicos, 2007; Mazellier and Vassilicos, 2010; Gomes-Fernandes et al., 2012) in the case of wind tunnel experiments and reported in Chapter 4. An elongated production region can be detected up to a streamwise distance $Y/d \approx 0.8$; beyond that point, differently from what occurs in the case of wind tunnel experiments, the decay of the grid generated turbulence is balanced out by the penetrating jet shear layer, thus leading to a plateau in the u/V_j and w/V_j. On the other hand, the axial component is instead interested by a further increment with a different slope, as in addition to the effect of the shear layer, the adverse pressure gradient imposed by the plate leads to a further increase in its magnitude. It is also interesting to notice that the upward shift of the peak in the velocity fluctuation, already experienced in the free jet case, results to be even more stressed in the impinging jet configuration. In fact, by identifying x_{peak} as the streamwise location where an appreciable change in the curve slope occurs, thus suggesting that the grid-production region is over, it is possible to see that in the present case $x_{peak} \approx 0.8d$ with respect to the submerged free jet case where the peak occurs at $x_{peak} \approx 1.6d$.

6.2.2 Vortical features

As already pointed out before, the presence of the grid unsettles the axial symmetry of the round jet owing to the uneven blockage ratio. The two shear regions, produced in correspondence of the spreading wake originating from the largest grid bar iteration, are characterized by a non-uniform curvature. As observed by other authors in the past (Gutmark and Grinstein, 1999; El-Hassan et al., 2011), a local curvature of the jet shear layer promotes the generation of streamwise vorticity. It can then be argued that the presence of the grid *pumps* streamwise vorticity into the flow field. It is well-known that streamwise vorticity is beneficial for the convective heat

transfer rate (Liepmann and Gharib, 1992), since it enhances the entrainment rate of quiescent air from the surrounding ambient. This motivates the significant heat transfer enhancement of FGs with respect to the JWT observed in Chapter 5. Figure 6.8 is representative of the time-averaged vortical flow field in the vicinity of the grid (up to $Y/d = 1.25$). The axial vorticity iso-surfaces $\omega_Y d/V_j = \pm 0.5$ reveal the presence of two couples of counter-rotating streamwise vortices that are generated in correspondence of the inner shear layer (i.e. the shear region towards the central jet) and two streamwise vortices that are instead produced in the outer shear layer (i.e. towards the jets issuing through region B-B', C-C'). By a symmetry argument, the complete vortical flow field can be then reconstructed. In correspondence of the largest grid bar, two couples of streamwise vortices are produced, respectively in the inner shear layer and in the outer shear layer. This aspect, as already discussed in the free jet configuration, has a direct effect on the jet entrainment rate. Indeed, differently from the case of a round jet, the transfer of vorticity from the azimuthal to the axial component leads to an enhancement of the spreading rate and, as a direct consequence, of the entrainment rate. Besides that, being the streamwise vortices triggered by the local curvature of the jet shear layer, their effect arise immediately past the grid (i.e. the jet spreading starts immediately). Differently from what happens in the free jet case, beyond $Y/d \approx 1.2$ the streamwise structures are dissipated, whilst in the free jet configuration are still present up to $Y/d \approx 4$. The vorticity field is then strongly perturbed by the presence of the impinged plate.

Figure 6.9 shows a detail of the flow field in the vicinity of the impingement plate along the X_{45} direction. It is worth to explicitly recall that the measurement volume is not symmetric with respect to the $\alpha = 45\,\mathrm{deg}$ direction. A symmetry argument has been then posed in order to fully visualize the vortical field in the FG-45 case; thus, the measured flow field is mirrored with respect to the plane $Z_{45}/d = 0$. The iso-surfaces of radial vorticity $\omega_{X_{45}} d/V_j = \pm 0.66$ are reported respectively in red/blue. In cyan, the iso-surface of the module of radial velocity $V_r/V_j = 0.35$ is reported.

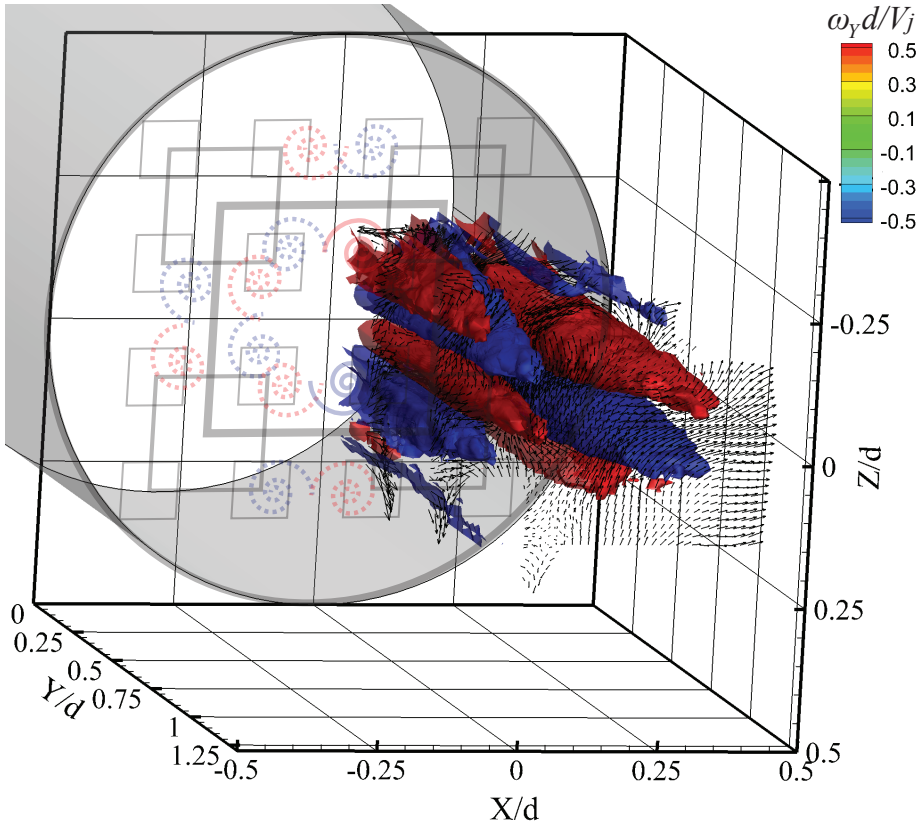

Figure 6.8: Iso-surfaces of axial vorticity $\frac{\omega_Y d}{V_j} = \pm 0.5$ (respectively in red/blue); in correspondence of the grid iterations a schematic representation of the expected vorticity field is reported. The vortices that are outside of the measured region and/or blanked for the sake of understanding, are reported with dashed lines. Vectors are reported in the XZ planes at $Y/d = \{0.2d, 0.5d, 1.2d\}$.

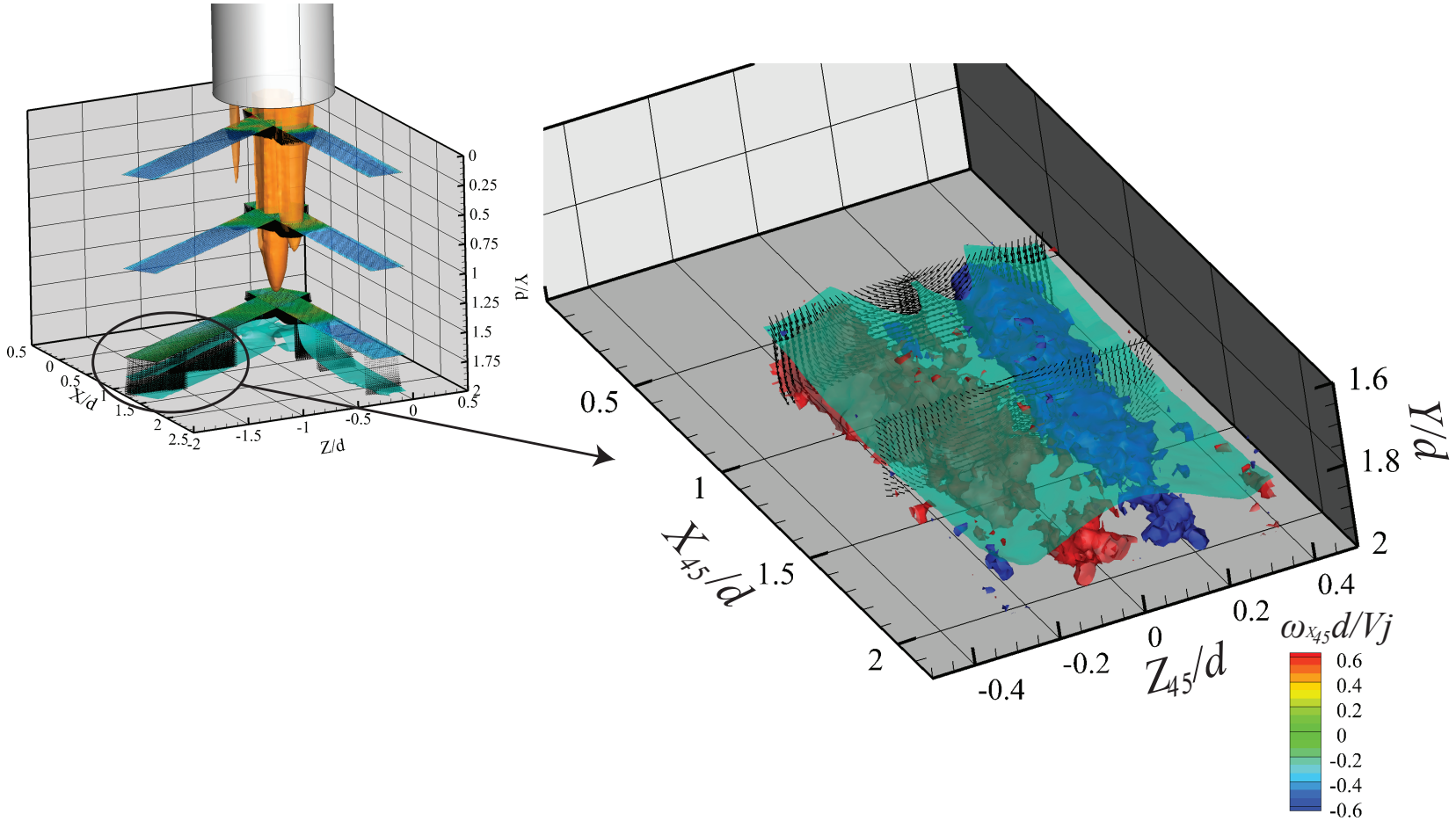

Figure 6.9: Iso-surfaces of radial vorticity $\frac{\omega_r d}{V_j} = \pm 0.66$ (respectively in red/blue); iso-surface of the velocity magnitude in the XZ plane (in cyan) normalized with respect to the bulk velocity $V_r/V_j = 0.35$. In plane vector representation at $X_{45}/d = \{1, 1.5\}$. For the sake of understanding, the measured flow field is mirrored with respect to the $Z_{45} = 0$ plane.

As already described in the previous section, along the X_{45} direction the wall jet becomes thicker. Alongside the already discussed higher mass flux that interests this region, a second effect is related to the two structures aligned with the X_{45} direction that cause a local upwash of the wall jet. This aspect has a direct impact on the scalar transfer of the fractal impinging jet (see Figure 6.3). Indeed, in Chapter 5 it has been shown that along the X_{45} direction a region of minimum in the heat transfer rate is present. Although counter-intuitive, since a higher flow rate is convected in this direction, the presence of the two counter-rotating structures causes a detrainment of fluid from the wall, thus a lower local convective heat transfer coefficient. With this conclusion, the scalar transfer topology in the stagnation region vicinity can be fully characterized: the five maxima that are detected in correspondence of the mesh print are associated to concurrent effect of the large axial momentum of the impinging jet and to the turbulent fluctuations introduced by the grid. Along the X and Z directions, a progressive decay of the convective heat transfer coefficient can be experienced, as characteristic of the developing wall jet region (Carlomagno and Ianiro, 2014). The production of counter-rotating wall vortices is then responsible for the region of minima along the X_{45} and Z_{45} directions.

6.2.3 Instantaneous flow field

The instantaneous organization of the flow field in the vicinity of the nozzle exit section is described in Figure 6.10. When issuing through region A of the grid, as already observed in the free jet case, the central jet experiences a meandering. In particular, in a similar fashion to what occurs in a case of a planar jet (Landel et al., 2012a,b), it oscillates within the $X-Y$, $Z-Y$ planes. In Figure 6.10 the iso-surface of axial velocity $V/V_j = 1.3$ is reported in translucent red along with the contour representation of the axial velocity within the $Z/d = 0$ plane. In gray, the iso-surface of the second invariant of the velocity gradient tensor $Q_{vv} > 0$ (Jeong and Hussain, 1995) is reported to underline the presence of coherent structures

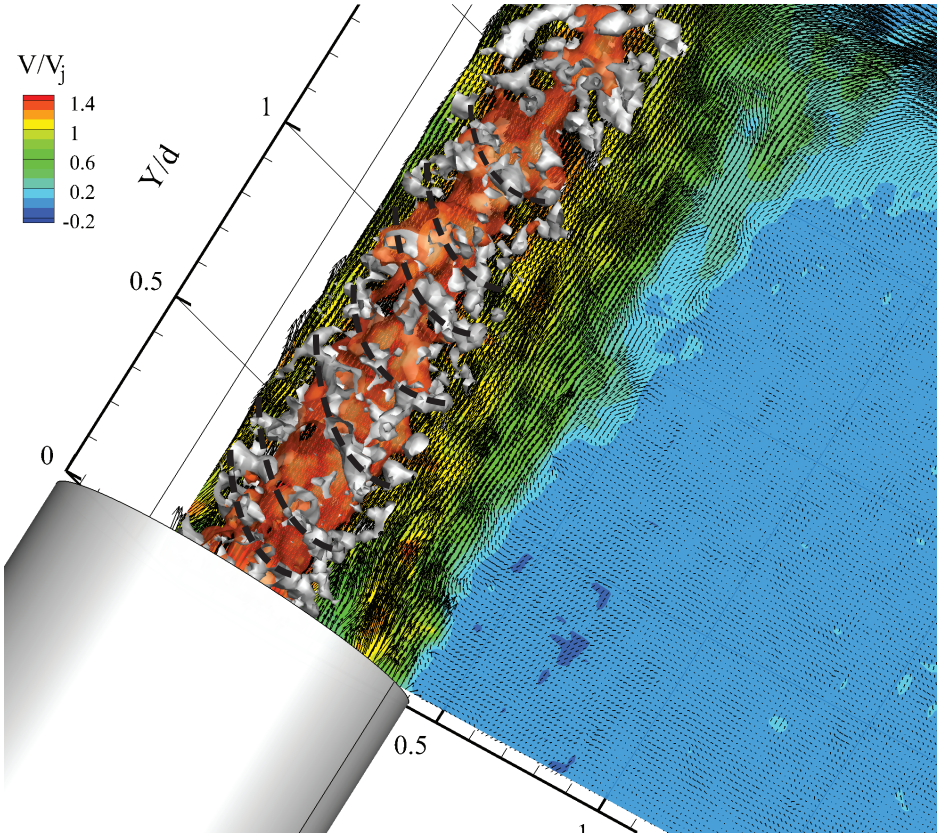

Figure 6.10: Iso-surfaces of axial velocity $V/V_j = 1.3$ (translucent red), $Q_{vv} > 0$ iso-surface (in gray). Contour representation of the axial velocity in the plane $Z/d = 0$; the iso-surfaces values are blanked for $X/d > 0.25$

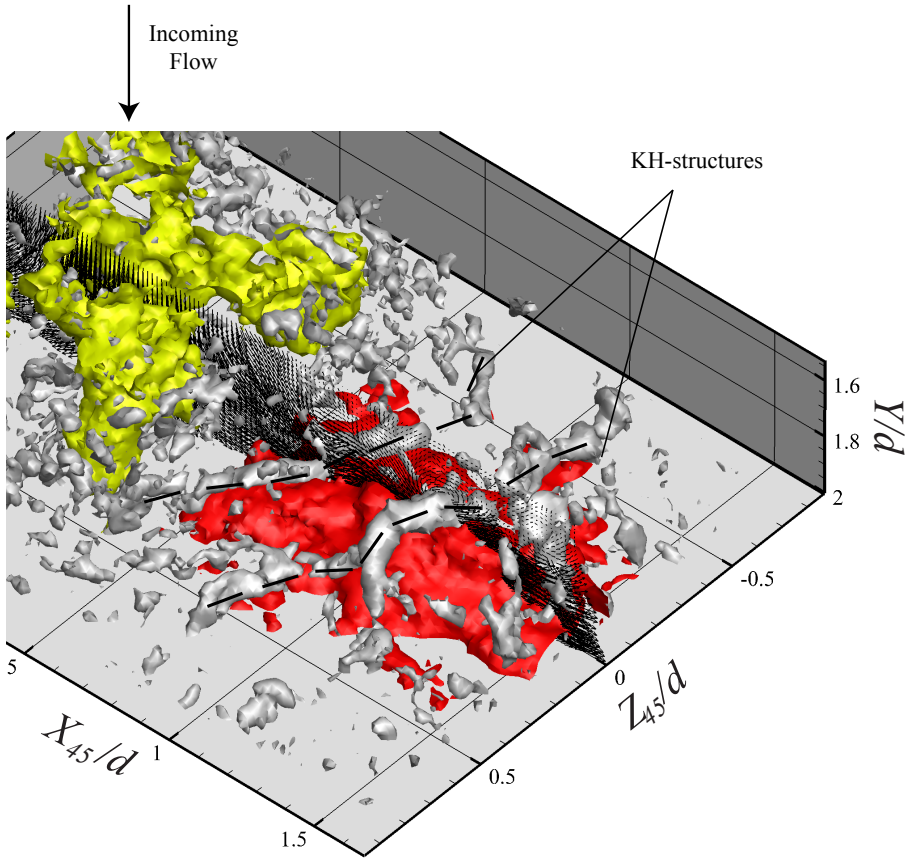

Figure 6.11: Iso-surfaces of axial velocity $V/V_j = 1$ (light green), $Q_{vv} > 0$ (in gray) and $U_{45}/V_j = 1$ (in red). Vector plot in the plane $Z_{45}/d = 0$

within the flow field. It can be seen how there is the presence of an helical vortex that embraces the central jet. This structure, which is highlighted for the sake of clarity with a dashed black line, is most likely responsible for the jet meandering.

In order to better exploit the features of the impingement region, a dedicated experiment is carried out, as reported in the experimental setup description (SET-CW sec. 6.1, Figure 6.1). An instantaneous realization of the SET-CW is reported in Figure 6.11. The iso-surfaces of $Q_{vv} > 0$ are depicted in gray; the impinging jet is underlined with the axial velocity iso-surface $V/V_j = 1$ (light green). In red, the radial velocity iso-surface $U_{45}/V_j = 1$ is also reported. In a similar fashion to what occurs in the case of a circular jet without any turbulence promoter, the presence of azimuthally coherent structures can be detected. These structures are generated within the jet shear layer, due to Kelvin-Helmholtz instabilities. In similar conditions, studying the flow field issuing through a square nozzle, Grinstein and DeVore (2014) found that the ring vortices that characterizes the round jet shear layer are still present, although their shape is deformed. In the present case, these structures are convected towards the impinging plate and are still present in the developing wall jet region. However, differently from what occurs in the case of JWT, the presence of the grid unsettles the flow symmetry. In Figure 6.11 two different structures enveloping the radial velocity iso-surface can be distinguished (in Figure 6.11 underlined with a black dashed line); as the velocity distribution is not constant along the azimuthal coordinate α, these structures will not be characterized by a uniform distance from the impinged plate. Indeed, moving farther from the $Z_{45}/d = 0$ plane, the structure progressively approaches the impinging plate. This is due to the upwash induced by the counter-rotating vortices outlined in paragraph. 6.2.2. Additionally, the structure is stretched along the streamwise direction due to the different advection velocity along the diagonal of the on-plate imprint of the grid.

CHAPTER 7

Effect of the grid geometric parameters on the convective heat transfer of impinging jets

From the literature survey presented in Chapter 1 and the results discussed in Chapter 4, 6, it is clear that the fractal geometry has an overwhelmingly larger impact on the jet flow with respect to the regular grid case. In Chapter 5, it has been shown that these differences reflect also in a more efficient convective heat transfer rate of the multi-scale grid. In this Chapter, the effect of the grid geometry on the convective heat transfer rate of impinging jet is explored in more detail by means of IR Thermography. The study concerns three main elements: the grid thickness ratio, the effect of the secondary grid iterations and the effect of the initial pattern. Furthermore, as it is often required also uniformity in the convective heat transfer rate, the effect of the aforementioned parameters on this element is also assessed.

7.1 Experimental apparatus

The experimental setup is similar to that described in Chapter 5.1. As a consequence, here only a description of the main differences is reported, with the aid of the schematic representation in Figure 7.1. The camera used for the experiments is different from the one employed in Chapter 5.1. Indeed, the sensitive area of the thin foil is imaged using a CEDIP Jade III MW-IR camera with a digital resolution of about 1.5 pix/mm (30 pix/d).

The convective heat transfer coefficient (h) is evaluated using the steady state *heated thin foil* heat flux sensor, as suggested by Astarita and Carlomagno (2013) and presented in Chapter 3.

Thirteen different nozzle to plate distances ($1 < Y/d < 7$ with $0.5d$ step) are investigated, in order to better understand the convective heat transfer behaviour at relatively short nozzle to plate distances. For each nozzle to plate distance 1000 images are collected at a frame rate of $100Hz$. The temporal separation between subsequent frames ($10ms$) is sufficiently large to consider the samples as statistically independent. In fact, the jet bulk velocity is, in the worst case scenario, about $14m/s$, which would correspond to an integral timescale of $1.43ms$, thus reasonably below the frame separation.

The convective heat transfer coefficient values are presented in non-dimensional form in terms of the Nusselt number spatial distribution and area averaged profiles $\overline{Nu}(r)$, where:

$$\overline{Nu}(r) = \frac{1}{\pi r^2} \int_0^r \int_0^{2\pi} \xi \cdot Nu(\xi, \theta)\, \mathrm{d}\theta \mathrm{d}\xi \tag{7.1}$$

Furthermore, similarly to what already done in Ianiro and Cardone (2012), in order to assess the effect of the geometric parameters on the uniformity of the convective heat transfer rate the spatial variance of the

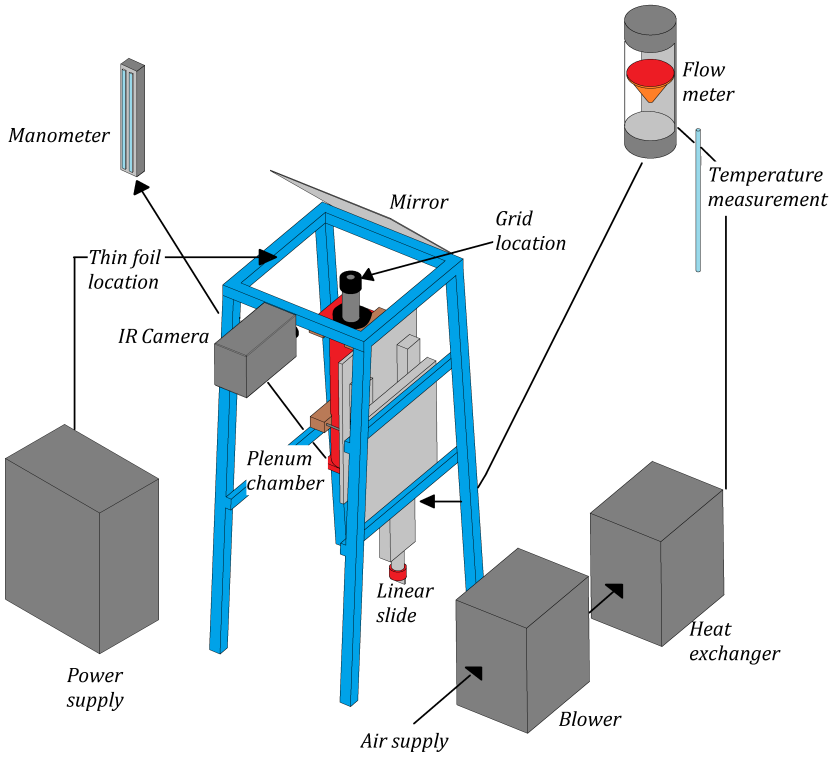

(a)

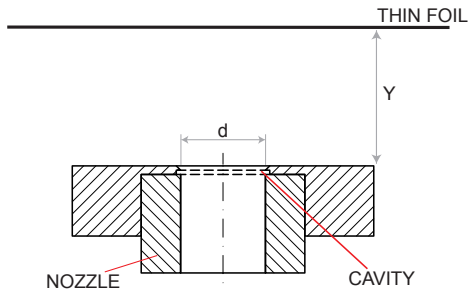

(b)

Figure 7.1: Schematic representation of the experimental apparatus used for the experiments (a) and detail of the cap used for allocating the grid insert in correspondence of the nozzle exit section.

	Typical value	Uncertainty	$\left(\frac{\partial R_i}{\partial X_i}\frac{\partial X_i}{\partial Nu}\right)\cdot 100$
T_w	310 K	0.2 K	2.8
T_{aw}	293 K	0.2 K	2.7
T_a	293 K	0.1 K	1.05
I	90 A	1 % of reading	1.1
V	1.9 V	1 % of reading	1.1
ϵ	0.95	0.01	0.03
d	0.02 m	1 %	0.02
s	50 μm	1 %	10^{-5}
$\dot{q}_{nc}$	210 $\frac{W}{m^2}$	20 %	2.8
Error %			5.2

Table 7.1: Uncertainty analysis.

Nusselt number $\sigma_{Nu}(r)$ defined as:

$$\sigma_{Nu}(r) = \frac{\sqrt{\frac{1}{\pi r^2}\int_0^r\int_0^{2\pi}\left(Nu(\xi,\theta)-\overline{Nu}(\xi)\right)^2 \mathrm{d}\theta\mathrm{d}\xi}}{\overline{Nu}(r)}\cdot 100 \qquad (7.2)$$

An uncertainty analysis of the values calculated using equation 3.16 is carried out as suggested by Moffat Moffat (1988). Each one of the terms involved in the equation are perturbed and its effect on the convective heat transfer coefficient values is reported in table 7.1. The resulting measurement error is $\pm 5.2\%$ and it is taken as the cut-off value to consider reliable an experiment when repeating it.

7.1.1 Grid insert description

The inserts used for the experiments are made of a $0.5mm$ thick stainless steel foil. The shape is cut by electrical discharge machining (EDM). In order to carry out the parametric study, three types of grids are considered:

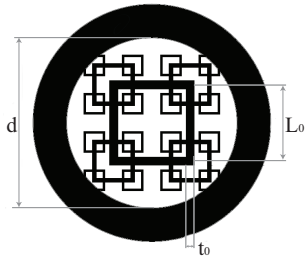

Figure 7.2: Schematic representation of a square fractal grid geometric parameters.

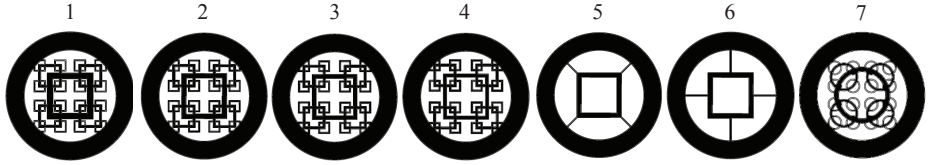

Figure 7.3: Schematic representation of the grids used in the experiments. See Table 7.2 for the corresponding geometric details.

- Square fractal grids;
- Single square grids;
- Circular fractal grid.

For both the square and the circular fractal grids, the initial pattern is repeated at three different scales (referred to as iterations). The square fractal grids characteristic parameters are presented in Chapter 4.1.3. The geometric parameters of the four square fractal grids used for the experiments are listed in table 7.2 (#1-4). Here and in the following the grid #2 ($L_r = t_r = 4$), also used for the measurements of Chapter 4, will be considered as a reference for the comparisons.

The effects of the secondary grid iterations are assessed by comparing the performances of the reference SFG with those of two square grids (SGs)

#	$L_0(mm)$	$t_0(mm)$	L_r	t_r	x^*/d
1	8.77	1.23	4.00	6.25	3.13
2	**9.00**	**1.00**	**4.00**	**4.00**	**4.05**
3	9.18	0.82	4.00	2.77	5.10
4	9.31	0.69	4.00	2.04	6.23
5 (SG1)	9.00	1.00	-	-	4.05
6 (SG2)	9.00	1.00	-	-	4.05
7 (CFG1)	11.46	1.00	4.00	4.00	6.56

Table 7.2: Geometric details of the grids. The reference grid is the #2, indicated in bold face.

#	Re	$\dot{m}[g/s]$	$\Delta p_0[Pa]$
1-4	**15000**	**5.1**	**320**
5-6	18800	6.2	260
7	15000	5.1	320

Table 7.3: Experimental conditions: the reference conditions are reported in bold face.

(#5, 6 in table 7.2 and Figure 7.3). These grids are obtained from the reference one by removing the second and third iterations and keeping the same first iteration (i.e. the central square), thus resulting in a significantly smaller blockage ratio (about 1/3). This difference is accounted for in the experiments carrying out the comparison between SFG and SGs under the same power input (similarly to what already done in Chapter 5 when comparing the SFG with a regular grid and a jet without turbulence promoter), i.e. the same product of the volumetric flow rate times the pressure drop across the grid; this turns into a larger effective Reynolds number for the SGs cases (see Table 7.3). Two different holding bars configurations are investigated in order to take into account any possible influence of those elements onto the convective heat transfer rate as shown in Figure 7.3.

Finally, the effect of the fractal pattern is assessed by comparing the reference grid with a circular fractal grid (CFG). The CFG is obtained from the SFG by centring the *j-th* annulus in correspondence of the centre of the *j-th* square, but keeping the same values of L_r and t_r of the reference SFG.

7.2 Results and discussion

7.2.1 Heat transfer spatial distribution: main features

The Nusselt number spatial distribution for the four square fractal grids as a function of the grid bar thickness t_r is reported in Figure 7.4. The comparison is carried out at three different nozzle to plate distances, namely $Y/d = \{2, 4, 7\}$. The qualitative behaviour in all the presented cases is similar: at short nozzle to plate distances, $Y/d = 2$, the grid print onto the impinged plate is reflected into five region of maxima, which must be addressed to the five jets issuing through the fractal grid iterations. Along the grid diagonals, four region of local minima can be detected, which reflects the asymmetry triggered by the presence of the grid. These regions, must be addressed to the presence of counter rotating wall vortices that

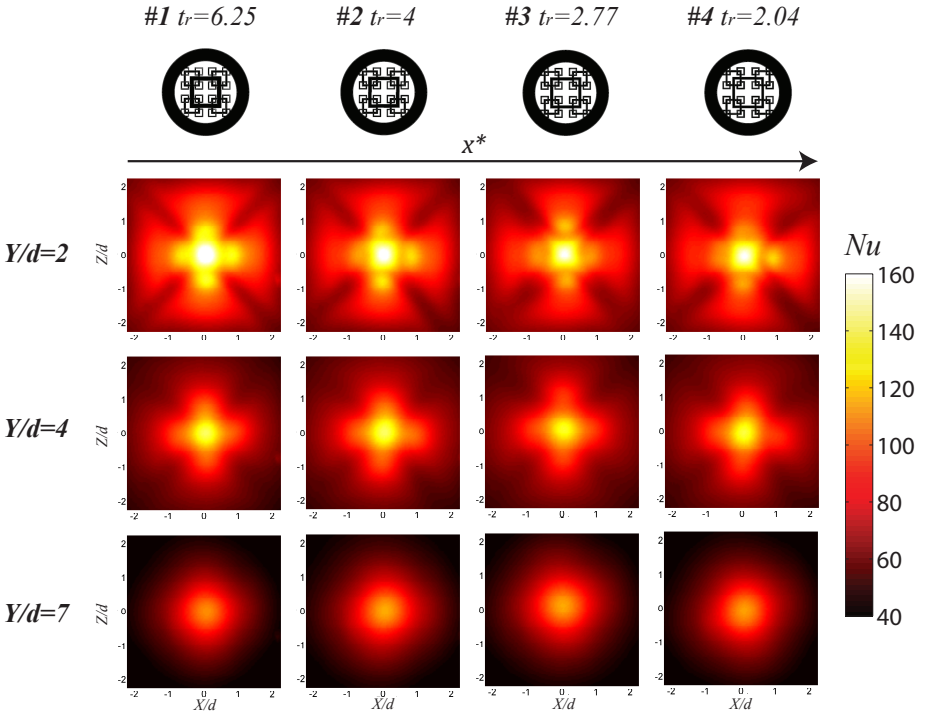

Figure 7.4: Nusselt number spatial distribution as a function of the grid bar thickness ratio $t_r = \{6.25, 4, 2.77, 2.04\}$ at three different nozzle exit section to plate distances $Y/d = \{2, 4, 7\}$.

produce a local upwash to the fluid, thus leading to a low convective heat transfer rate region (see Chapter 6 for a more detailed discussion). As the nozzle exit section to plate distance increases, the grid print is less clearly visible. Indeed, as also shown when discussing the flow field features in Chapter 6, the outer jets are progressively smeared out due to the turbulent diffusion. At $Y/d = 7$ the convective heat transfer rate map looses the asymmetry introduced by the presence of the grid, since it is progressively approaches the JWT behaviour. In Figure 7.5 the Nusselt number distributions of the reference SFG, the single square grid (SG) and the circular fractal grid (CFG) are reported at three different nozzle to plate distances $Y/d = \{2, 4, 7\}$. The first two columns (rounded with a dashed black line) are addressed to exploit the effect on the secondary grid iterations onto the convective heat transfer rate. It is worth recalling that, in order to carry out a fair comparison, the SG is tested under the same power input of the SFG, thus resulting in a larger effective Reynolds number. It is interesting to notice that, despite the absence of the second and third iterations, the convective heat transfer features are relatively similar: the cross-shaped wall print is still present in the SG case, although the maximum obtained in correspondence of the centre of the grid is significantly lower than the one of the SFG. This must be addressed, as will be also discussed later in more detail, to the higher turbulence intensity level that can be achieved using the SFG with respect to the SG. Along the central square diagonals, at short nozzle to plate distances the presence of four region of minima is still clearly visible, thus suggesting that also in this case the near wall flow field is characterized by the presence of counter rotating wall vortices that produce a local upwash. The differences in terms of convective heat transfer rate are completely smeared out at larger nozzle to plate distances; indeed, at $Y/d = 7$ the Nu distribution significantly resemble those of the JWT, thus suggesting that the effect of the grid is over.

The second and third columns in Figure 7.5 (in the red dashed box) are representative of the comparison between the SFG and CFG. At short nozzle to plate distances, also in the CFG case the grid print is clearly visible.

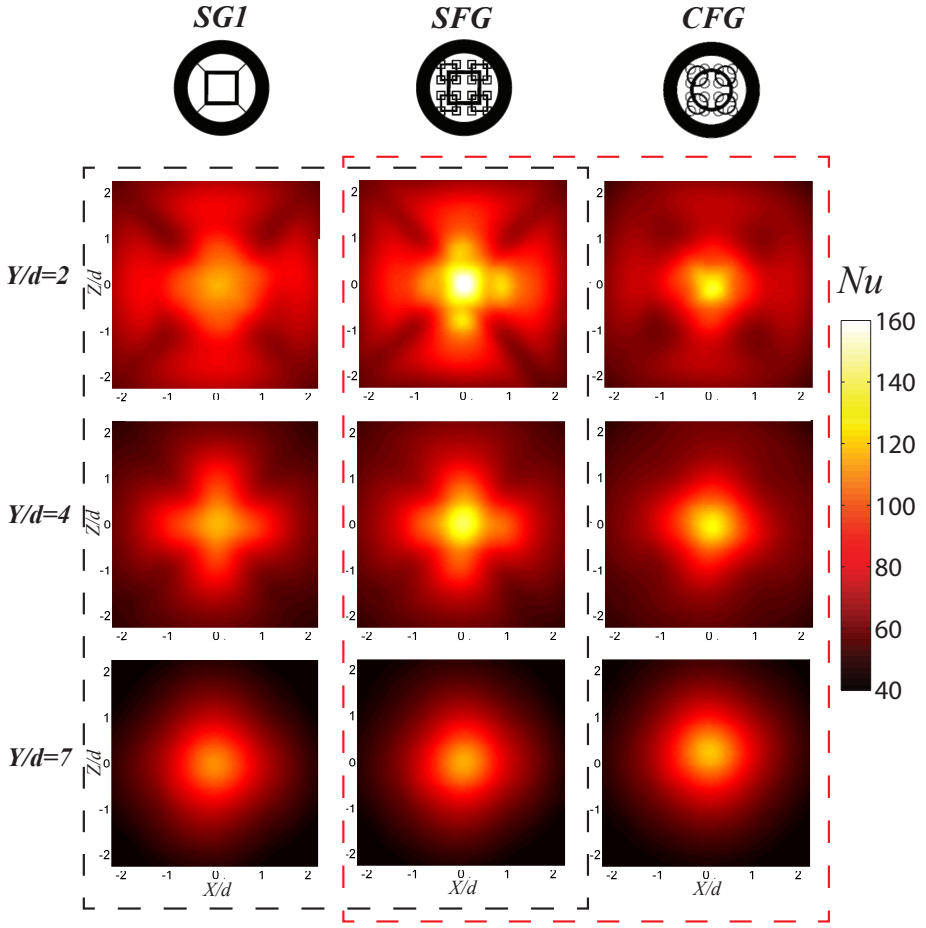

Figure 7.5: Nusselt number spatial distribution for the SG, SFG and CFG at three nozzle exit section to plate distances $Y/d = \{2, 4, 7\}$.

However, it can be clearly noticed that the CFG attains significantly lower values of the convective heat transfer rate. Owing to the wakes of the secondary grid iterations four regions of minima are still detectable, although differently from the SFG case, a more uniform distribution can be detected. Moving farther from the nozzle exit section, at $Y/d = 4$, the flow is less affected by the grid geometry than the SFG case. Owing to their inherent geometry SFGs can be considered as more efficient in the production of streamwise vorticity. This element is twofold: first, the entrainment rate (and as direct consequence the scalar transfer) of a circular jet equipped with a SFG is larger than with a CFG; moreover, the less energetic vortices are dissipated at shorter streamwise distances, thus resulting in a more uniform convective heat transfer distribution. Interestingly enough, at $Y/d = 7$, although the Nu distribution approaches the one typical of a jet without turbulator, the stagnation point Nusselt number attained by the CFG is larger than the SFG. This might be addressed to the larger x^*/d values that characterize the CFG (see table 7.2, although there is no evidence of the fact that the scaling proposed by Mazellier and Vassilicos (2010)) is effective for CFGs), that could suggest a more elongated production region and as a consequence, a larger turbulence intensity level as Y/d increases.

7.2.2 Area averaged Nusselt number profiles and uniformity of the convective heat transfer rate

The area averaged Nusselt number $\overline{Nu}$ profiles along with the spatial variance σ_{Nu} profiles for the four SFGs are reported in Figure 7.6 as a function of the radial position r/d at three nozzle to plate distances $Y/d = \{2, 4, 7\}$. It is clearly visible that the thickness ratio values affect both the stagnation point and the developing wall jet region Nusselt number. Indeed, at short nozzle to plate distances (see figure 7.6a), in the vicinity of the stagnation point (up to $r/d \approx 0.5$), a higher t_r results to be beneficial for the convective heat transfer rate. This is coherent with the fact that

a higher t_r is related to an anticipated turbulence intensity peak, being x^*/d lower (see table 7.2). However, in terms of uniformity (figure 7.6b), a lower t_r is desirable. Indeed, the lowest σ_{Nu} is achieved for the lowest value of t_r. This is directly related to the more uniform distribution of the grid blockage ratio in the case of $t_r = 2.04$: in this case, the flow issuing past the grid results to be more uniform than the case of $t_r = 6.25$, where a strong contraction is imposed to the flow in correspondence of the nozzle axis.

In addition to the higher uniformity, it is very interesting to notice how a lower t_r is more efficient in terms of area averaged Nusselt number when both r/d and the nozzle exit section to plate distance increase. The former consideration must be addressed to the fact that at higher t_r a larger momentum is convected through the central iteration (being the axial velocity larger), thus leading to a momentum deficit at larger r/d. The latter is instead associated to the fact that at lower t_r, as the Y/d values increase, the more elongated turbulence production compensates for the axial velocity decay in the stagnation region.

In order to best exploit the turbulence intensity level onto the convective heat transfer rate, in Figure 7.7 is reported the stagnation point Nusselt number as a function of the nozzle exit section to plate distance. It can be seen how under the same flow rate and blockage ratio, the convective heat transfer rate is strongly affected by the location of the peak in the turbulence intensity profile. Indeed, a larger thickness ratio is representative of a smaller x^*/d value (see Table 7.2), which is directly related to the maximum in the velocity fluctuation. According to the results obtained in the case of free jet in Chapter 4 the location of the turbulence intensity peak is shifted upward with respect to the case of wind tunnel experiments ($\approx 0.45x^*$ in the case of Mazellier and Vassilicos (2010)) due to the effect of the penetrating shear layer onto the spreading wakes. As a consequence, for t_r values equal to 6.25 and 4 the Nusselt number profiles result to be monotonically decreasing, since both the axial velocity and the velocity fluctuations are decaying. On the other hand, the $t_r = 2.04$ case

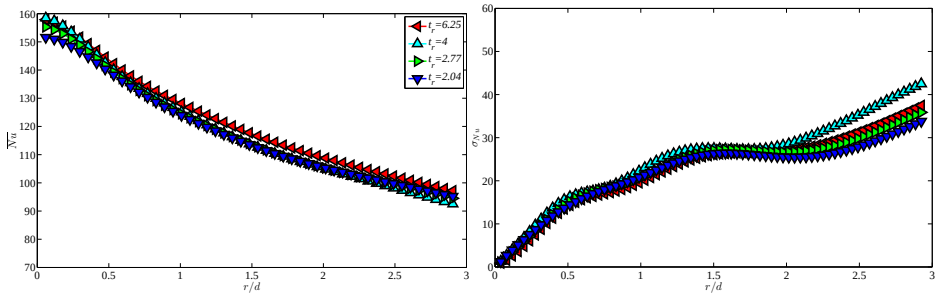

(a) $\overline{Nu}$ at $Y/d = 2$ (b) σ_{Nu} at $Y/d = 2$

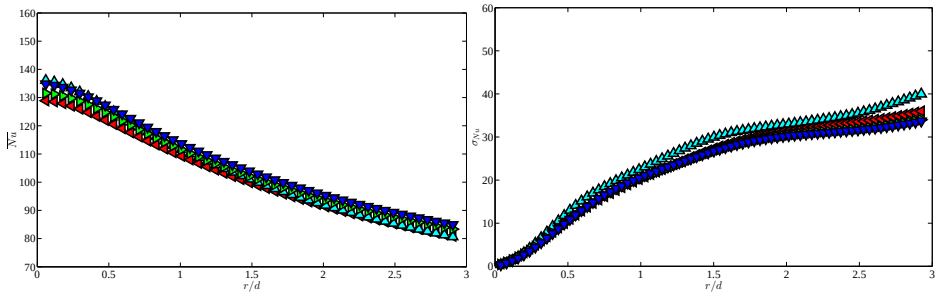

(c) $\overline{Nu}$ at $Y/d = 4$ (d) σ_{Nu} at $Y/d = 4$

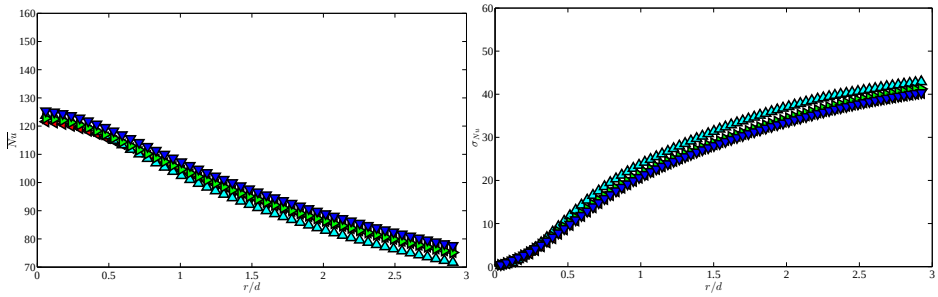

(e) $\overline{Nu}$ at $Y/d = 7$ (f) σ_{Nu} at $Y/d = 7$

Figure 7.6: Area averaged Nusselt number profiles (a, c, e) and spatial variance of the Nusselt number (b, d, f) as a function of the radial position at three nozzle to plate distances $Y/d = \{2, 4, 7\}$ for the SFGs $t_r = \{6.25, 4, 2.77, 2.04\}$.

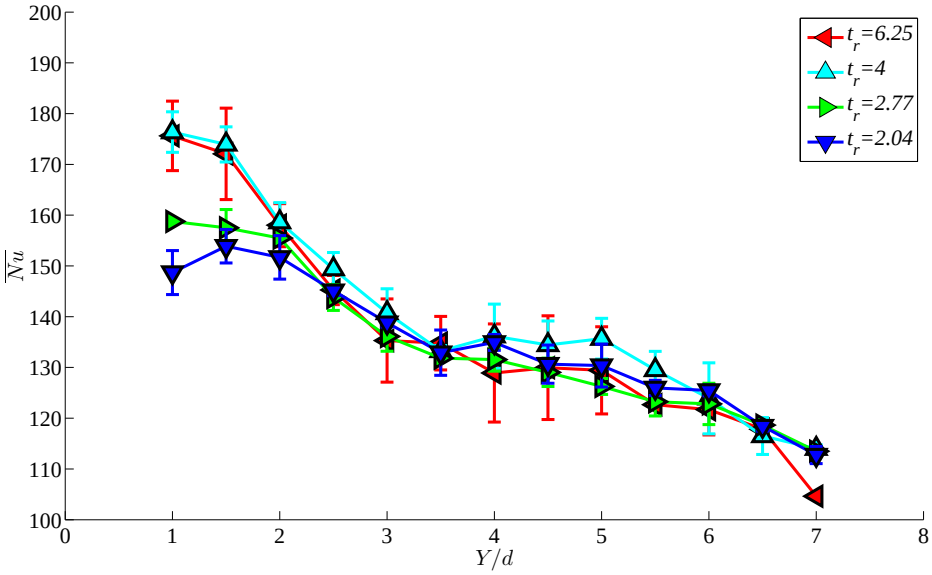

Figure 7.7: Stagnation point Nusselt number profiles as a function of the nozzle to plate distance Y/d for the four grid bar thickness ratio $t_r = \{6.25, 4, 2.77, 2.04\}$.

is characterized by an increment of $\overline{Nu}$ up to $Y/d \approx 1.5$, as the turbulence production compensates for the decay in the axial velocity. Beyond that point, both the velocity fluctuations and the axial velocity are decaying, thus leading to the detected monotonic decrease in the Nusselt number profile.

The dependence on the t_r is visible up to $Y/d \approx 2.5$; in fact, beyond that point all the cases present a similar behaviour. It is interesting to notice that the profiles present a plateau in the region between $3.5 < Y/d < 5.5$. This must be addressed to the effect of the further increment in the velocity fluctuation related to the penetrating shear layer towards the jet centreline, which compensates for the grid turbulence decay. Finally, for $Y/d > 5.5$ the effect of the shear layer is not efficient enough to compensate for the axial velocity decay, causing a further change in the $\overline{Nu}$ slope, which progressively approaches the power law decay as characteristic of the JWT case (Viskanta, 1993). In figure 7.8 the effect of the secondary grid iterations on the convective heat transfer rate and its uniformity is investigated comparing the reference SFG with two SGs with different holding bars configurations (see Figure 7.3) as a function of the radial position and at different nozzle exit section to plate distances $Y/d = \{2, 4, 7\}$. It is useful to recall that, since the SGs grids are characterized by a significantly lower blockage ratio, in order to carry out a fair comparison the test Reynolds number is set such that the power input is kept as constant between the SFG and SGs cases (see table 7.3). Looking at the σ_{Nu} profiles it is possible to see that the two SGs cases agree quite well, thus suggesting that there is no effect of the holding bars onto the convective heat transfer rate distribution. In proximity of the stagnation point, independently on the nozzle to plate distance the SFG attains larger values of the $\overline{Nu}$. Particularly sensitive is the enhancement that the use of the SFG provides at $Y/d = 2$, as it attains values about 40% larger than those of the SGs. This must be addressed from one side to the larger turbulence intensity level that SFGs may achieve with respect to SGs; moreover, the fractal grid is responsible for the production of streamwise vorticity (see

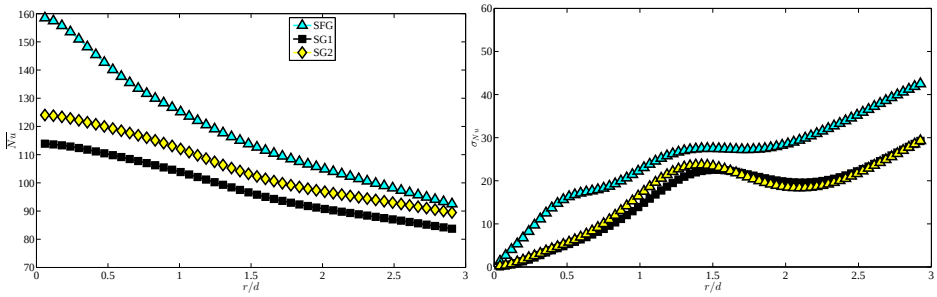

(a) $\overline{Nu}$ at $Y/d = 2$ (b) σ_{Nu} at $Y/d = 2$

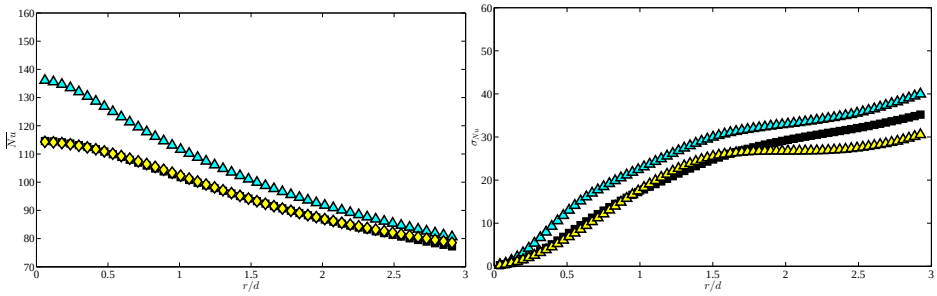

(c) $\overline{Nu}$ at $Y/d = 4$ (d) σ_{Nu} at $Y/d = 4$

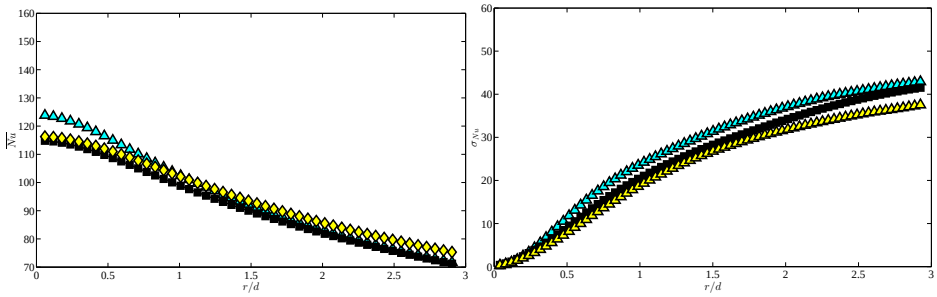

(e) $\overline{Nu}$ at $Y/d = 7$ (f) σ_{Nu} at $Y/d = 7$

Figure 7.8: Area averaged Nusselt number profiles (a, c, e) and spatial variance of the Nusselt number (b, d, f) as a function of the radial position at three nozzle to plate distances $Y/d = \{2, 4, 7\}$ for the reference SFG and the SGs.

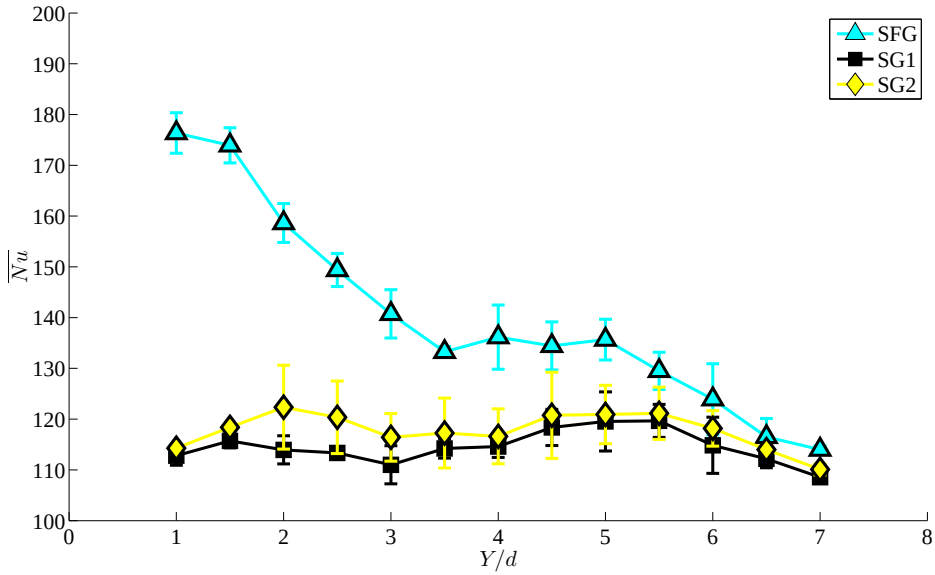

Figure 7.9: Stagnation point Nusselt number profiles as a function of the nozzle to plate distance Y/d for the reference SFG and the SGs.

Chapter 4), which leads to a strong enhancement of the entrainment rate and as consequence of the scalar transfer Liepmann and Gharib (1992). As the nozzle to plate distance Y/d increases, the differences are progressively smeared out; in particular, at $Y/d = 7$ (see Figure 7.8e), when integrating over a circle of radius $2.5d$ the SGs are practically equivalent to the SFG case. However, in terms of uniformity the SGs perform better than SFGs, independently on the Y/d location.

In Figure 7.9 a detail of the effect of the nozzle to plate distance on the stagnation point Nusselt number for the reference SFG and the SGs is reported. It is possible to notice that the secondary grid iterations play a key-role in the heat transfer enhancement process. Indeed, in the SG1 and SG2 cases the $\overline{Nu}$ profiles are nearly constant up to $Y/d = 6$. Similarly to what occurs to the SFG cases, between $3.5 < Y/d < 6$ the penetrating shear layer has a direct effect on the convective heat transfer rate, leading

for larger values of Y/d to a progressive approach of the square grids cases to the SFG one.

In Figure 7.10 the effect of the fractal pattern is investigated by comparing the reference SFG with an equivalent CFG (see section 7.1) as a function of the radial position and at different nozzle exit section to plate distances (namely $Y/d = \{2, 4, 7\}$). At small distances from the impinged plate, the SFG outperforms the CFG case. This element, as already qualitatively observed when discussing the Nusselt number spatial distribution, must be addressed to the higher capability of the SFG in producing streamwise vorticity. Indeed, similarly to the case of SGs, this leads to a higher entrainment rate and, as a direct consequence, to a higher convective heat transfer rate. However, at larger nozzle to plate distances and radial distances from the stagnation point, the gap between the two cases is strongly reduced. In terms of uniformity the two cases are very close, attaining similar values independently on the axial distance.

The $\overline{Nu}$ in correspondence of the stagnation point for the reference SFG and CFG are plotted as a function of the nozzle to plate distance Y/d in figure 7.11. As already mentioned when discussing figure 7.10, the gap between the SFG and CFG progressively reduces as Y/d increases. Owing to the larger value of x^*/d, the CFG is characterized by a more elongated turbulence production region. As a consequence, the CFG will attain the maximum in the turbulence intensity level at larger streamwise distances from the nozzle exit section balancing out the axial velocity decay, whilst in the SFG case both the axial velocity and the turbulence intensity level are decaying. Moreover, similarly to what occurs in the SFG case, the stagnation point Nu in the CFG case is also characterized by a plateau for $3 < Y/d < 6$, owing to the effect of the jet shear layer that penetrates towards the jet centreline, further *pumping* the grid generated turbulence. Beyond $Y/d = 6$, the CFG approaches the values observed in the SFG case, as the effect of the grid is practically lost at that distance.

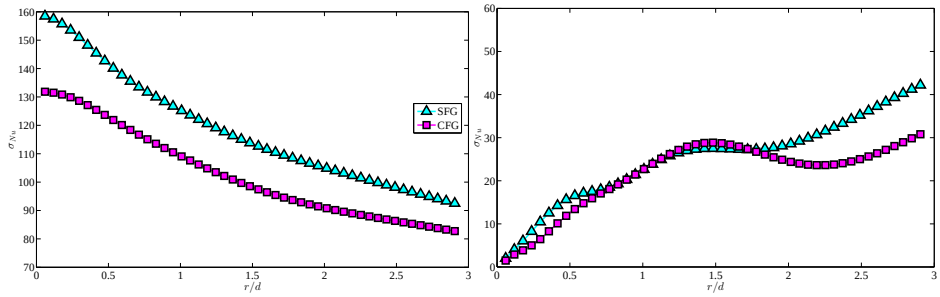

(a) $\overline{Nu}$ at $Y/d = 2$ (b) σ_{Nu} at $Y/d = 2$

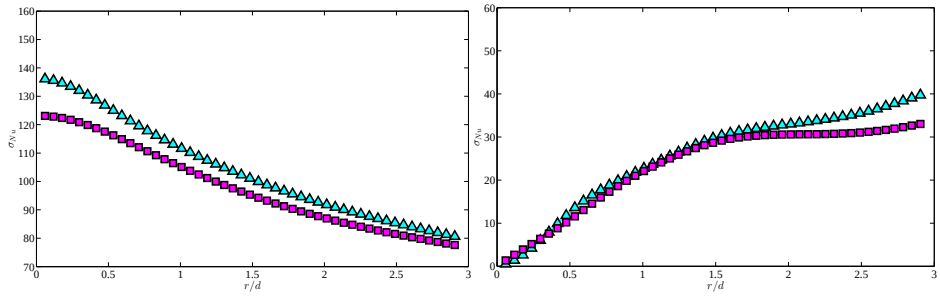

(c) $\overline{Nu}$ at $Y/d = 4$ (d) σ_{Nu} at $Y/d = 4$

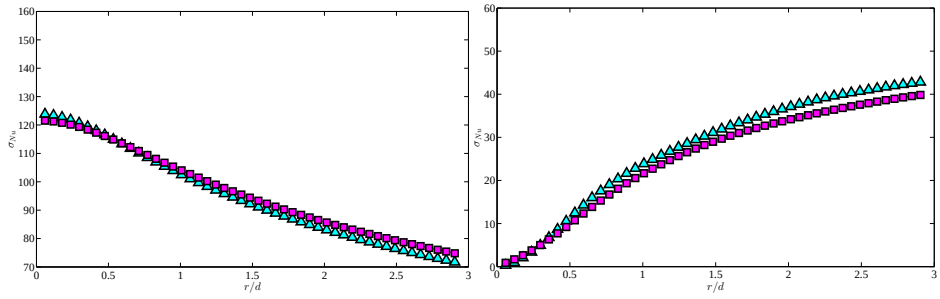

(e) $\overline{Nu}$ at $Y/d = 7$ (f) σ_{Nu} at $Y/d = 7$

Figure 7.10: Area averaged Nusselt number profiles (a, c, e) and spatial variance of the Nusselt number (b, d, f) as a function of the radial position at three nozzle to plate distances $Y/d = \{2, 4, 7\}$ for the reference SFG and the CFG.

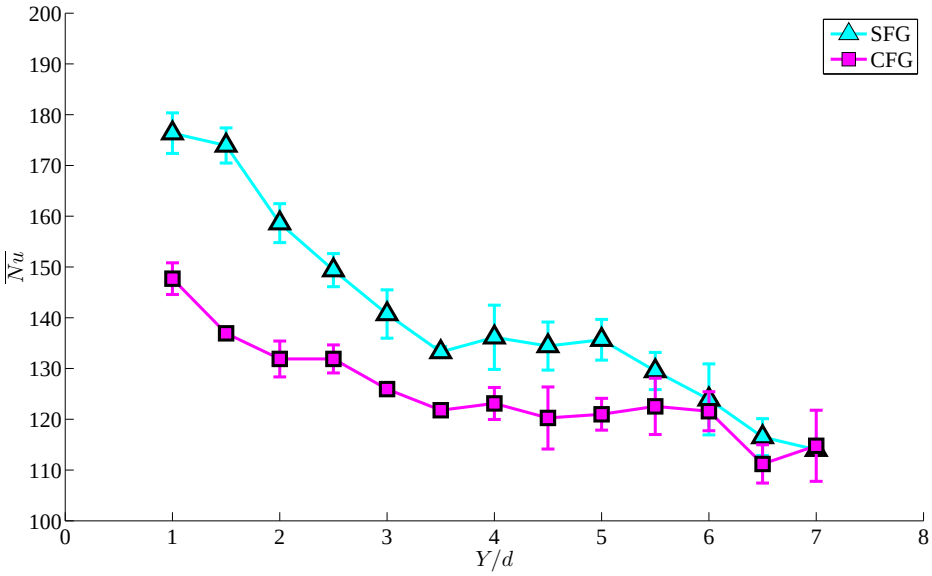

Figure 7.11: Stagnation point Nusselt number profiles as a function of the nozzle to plate distance Y/d for the reference SFG and the CFG.

Conclusions and Future perspectives

In this thesis an experimental analysis of fractal generated turbulence in free and impinging jets is carried out. Two different measurement techniques are applied: Particle Image Velocimetry (both planar and volumetric) for the flow field analysis and IR Thermography for the evaluation of the convective heat transfer rate of fractal impinging jets.

In the free jet case (Chapter 4) the effect of the fractal grid on the flow field organization is shown. Indeed, at short nozzle to plate distances, the jet behaves in a multichannel fashion, due to the uneven distribution of the grid blockage ratio. This effect is progressively smeared out due to turbulent diffusion. The investigation of the turbulence intensity profile along the nozzle axis leads to some interesting differences with respect to the case of free-shear flow; in fact, the location of the peak in the turbulence intensity profile which in the case of free-shear flow should be located at about $Y/d \approx 1.82$ anticipates; this effect must be addressed to the blockage effect of the growing external shear layer which triggers an asymmetry in the spreading of the fractal grid iterations wakes. This finding is particularly relevant for applications where the fractal geometry is tuned to optimize the scalar transfer and mixing at a precise streamwise location. The volumetric PIV measurements provide a clearer view of the large scale organization of the flow field. In particular, a first set of experiments (referred to as SET-A) gives the evidence of the presence of couples of counter-rotating streamwise vortices which embrace the cross-

shaped jet. They are associated to the azimuthal disturbs induced by the fractal grid in a similar fashion to what observed in other non-circular jets such as tabbed and chevron. However, differently from the cited cases, due to the multi-scale topology of the flow field (being the fractal grid inherently multi-scale), the presence of streamwise vortices with different characteristic dimensions is experienced. In particular, different structures are convected down to different streamwise locations along the nozzle axis depending on the dimensions of the source (i.e., the grid bar thickness).

The convective heat transfer rate of the fractal jet is then tested in the impinging configuration and compared to the performances of a jet without turbulence promoter and an equivalent (i.e. with the same blockage ratio) regular grid (Chapter 5, 4). In order to account for the differences in terms of blockage ratio induced by the presence of the grid, a fair comparison is carried out under the same power input conditions, i.e. under the same product of the pressure difference between the stagnation chamber and the ambient times the volumetric flow rate. The achievable increment in terms of localized convective heat transfer rate is astonishing: at short nozzle to plate distances ($Y/d = 2$), at the stagnation point, the jet equipped with a fractal grid outperforms the regular grid about of the 45%. The differences are still significant when integrating over an area having radius of $2d$ (about 20%). The strong heat transfer enhancement is addressed to three main agents (as shown by the results obtained in Chapter 5): first, the uneven distribution of the blockage ratio leads to strong accelerations of the fluid, thus to a significantly larger impinging velocity; second, the presence of streamwise structures, as presented also in the free jet case, are responsible for a significant increment of the jet entrainment rate and as consequence of the scalar transfer of the jet. Last, but not least, the turbulence intensity profile that characterizes fractal grids leads to a sensitive increment of the turbulence intensity level in correspondence of the impinged plate, thus to a larger heat transfer rate. Furthermore, the convective heat transfer rate presents region of minima in correspondence of the diagonals of the central grid iteration. The volumetric results show that they are addressed to the

presence of counter rotating wall vortices that produce a local increment of the wall jet thickness.

Finally, the effect of the grid geometry on the convective heat transfer rate distribution and its uniformity is addressed by means of IR Thermography experiments in Chapter 7. Three main effects are taken into account: the grid thickness ratio, the secondary iterations and the initial pattern shape. The first parameter shows that, at short nozzle to plate distances, the convective heat transfer rate increments accordingly to the location of the peak in the turbulence intensity profile. Indeed, for wind tunnel experiments, it has been show that the higher the thickness ratio, the narrower is the turbulence production region. The effect of the secondary grid iterations, which is assessed by comparing the reference fractal grid with two single square grids under the same power input, highlights striking differences especially at short nozzle to plate distances in terms of convective heat transfer rate. This is a clear indication of the key-role played by the secondary grid iterations (and as a consequence by the effect they have on the turbulence intensity profile) onto the convective heat transfer rate distribution. Finally, the comparison between the square fractal grid and the circular fractal grid indicates that the latter is more efficient in terms of convective heat transfer rate, although the former generated a more uniform distribution. This must be addressed to the fact that square fractal grids are more effective in the production of streamwise vorticity and as already remarked this is favourable from the entrainment rate standpoint.

Although an extensive study of the capabilities of fractal grids when employed as turbulence promoters in jets has been carried out in this thesis, many questions are still open. First, the prediction of the extent of this upstream displacement of the peak of the turbulent kinetic energy profile requires a parametric study on the geometry of the fractal grid. In particular it would be of interest to identify the spreading wake-shear layer interaction that leads to the upward shift of the maximum of the turbulence intensity profile. One lead might be to introduce a parameter

in the x_{peak} correlation that takes into account the effect of the growing shear layer.

The convective heat transfer distribution also leaves several points open: from the topology standpoint, the region of minima are shown to be dependent on the effect of the counter rotating wall vortices that thicken the wall jet. However, the mechanism that leads to their production still requires studies. In terms of heat transfer capabilities number, a more extensive study with a larger number of grids per parameter might lead to the development of a predictive model on the stagnation point heat transfer rate as a function of the thickness ratio. Furthermore, a larger number of parameters might be accounted, as for example the introduction of a larger number of iterations, which may also lead to wider limits to vary parameters as the thickness ratio.

Finally, in order to investigate efficient means to achieve a more uniform convective heat transfer distribution, the analysis of nozzle configurations (i.e. chevron nozzle) that allow a controlled spreading wake-shear layer interaction might be of interest.

Bibliography

Abramovich, G. N., 1963. The Theory of Turbulent Jets. The MIT Press.

Adrian, R., 1991. Particle-imaging techniques for experimental fluid mechanics. Annual Review of Fluid Mechanics 23, 261–304.

Adrian, R., Westerweel, J., 2011. Particle Image Velocimetry. Cambridge University Press.

Adrian, R., Yao, C., 1984. Development of pulsed laser velocimetry (plv) for measurement of fluid flow. In: Proceedings of the 8^{th} Biennial Symposium on Turbulence, Rolla, Missouri (USA). pp. 170–186.

Astarita, T., 2007. Analysis of weighting windows for image deformation methods in piv. Experiments in Fluids 46, 1115–1123.

Astarita, T., Carlomagno, G., 2013. Infrared Thermography for Thermo-Fluid-Dynamics. Springer.

Avallone, F., Ye, Q., Schrijer, F. F. J., Scarano, F., Cardone, G., 2014. Tomographic piv investigation of roughness-induced transition in a hypersonic boundary layer. Experiments in Fluids 55 (1852).

Batchelor, G. K., 1953. The theory of homogeneous turbulence. Cambridge University Press.

Becker, H. A., Massaro, T. A., 1968. Vortex evolution in a round jet. Journal of Fluid Mechanics 31, 435.

Bradshaw, P., Ferriss, D. H., Johnson, R. F., 1964. Turbulence in the noise producing region of a circular jet. Journal of Fluid Mechanics 19, 591.

Cafiero, G., Ceglia, G., Discetti, S., Ianiro, A., Astarita, T., Cardone, G., 2014a. On the three-dimensional precessing jet flow past a sudden expansion. Experiments in Fluids 55, 1677.

Cafiero, G., Discetti, S., Astarita, T., 2014b. Heat transfer enhancement of impinging jets with fractal-generated turbulence. International Journal of Heat and Mass Transfer 75, 173–183.

Cafiero, G., Discetti, S., Astarita, T., 2016. Flow field topology of impinging jets with fractal inserts. In: Progress in Turbulence VI-. Vol. 165. Springer Proceedings in Physics, pp. 243–248.

Carlomagno, G. M., Ianiro, A., 2014. Thermo-fluid-dynamics of submerged jets impinging at short nozzle-to-plate distance: A review. Experimental Thermal and Fluid Science 58, 15–35.

Castro, I. P., 2016. Dissipative distinction. Journal of Fluid Mechanics 788, 1–4.

Crow, S. C., Champagne, F. H., 1971. Orderly structure in jet turbulence. Journal of Fluid Mechanics 48, 547.

Discetti, S., 2013. Tomographic particle image velocimetry. Ph.D. thesis, University of Naples Federico II.

Discetti, S., Astarita, T., 2012a. Fast 3d piv with direct sparse cross-correlations. Experiments in Fluids 53, 1437–1451.

Discetti, S., Astarita, T., 2012b. A fast multi-resolution approach to tomographic piv. Experiments in Fluids 52, 765–777.

Discetti, S., Astarita, T., 2014. The detrimental effect of increasing the number of cameras on self-calibration for tomographic piv. Measurement Science and Technology 25, 084001.

Discetti, S., Natale, A., Astarita, T., 2013. Spatial filtering improved tomographic piv. Experiments in Fluids 54, 1505.

El-Hassan, M., Assoum, H., Martinuzzi, R., Sobolik, V., Abed-Meraim, K., Sakout, A., 2013. Experimental investigation of the wall shear stress in a circular impinging jet. Physics of Fluids 25, 10.1063/1.4811172.

El-Hassan, M., Meslem, A., Abed-Meraim, K., 2011. Experimental investigation of the flow in the near-field of a cross-shaped orifice jet. Physics of Fluids 23, 10.1063/1.3562841.

Elsinga, G. E., Scarano, F., Wieneke, B., van Oudheusden, B. W., 2016. Tomographic particle image velocimetry. Experiments in Fluids, 933–947.

Elsinga, G. E., Wieneke, B., Scarano, F., van Oudheusden, B. W., 2006. Tomographic particle image velocimetry. Experiments in Fluids 41, 933.

George, W. K., 1992. The decay of homogeneous isotropic turbulence. Physics of Fluids 4.

Ghaemi, S., Scarano, F., 2010. Multi-pass light amplification for tomographic paticle image velocimetry applications. Measurement Science and Technology 21, 127002.

Gomes-Fernandes, R., Ganapathisubramani, B., Vassilicos, J. C., 2012. Particle image velocimetry study of fractal-generated turbulence. Journal of Fluid Mechanics 711, 306–336.

Gordon, R., Herman, G., 1971. Reconstruction of pictures from their projections. Communications of the ACM 14, 759.

Grinstein, F., 2001. Vortex dynamics and entrainment in rectangular free jets. Journal of Fluid Mechanics 437, 69–101.

Grinstein, F., DeVore, C., 2014. Dynamics of coherent structures and transition to turbulence in free square jets. Physics of Fluids 8.

Gutmark, E. J., Grienstein, F. F., 1999. Flow control with noncircular jets. Annual Review of Fluid Mechanics 31, 239–272.

Hadžiabdić, M., Hanjalić, K., 2008. Vortical structures and heat transfer in a round impinging jet. Journal of Fluid Mechanics 596, 221–260.

Herman, G., Lent, A., 1976. Iterative reconstruction algorithms. Computers in Biology and Medicine 6, 273–294.

Ho, C. M., Gutmark, E. J., 1987. Vortex induction and mass entrainment in a small-aspect-ratio elliptic jet. Journal of Fluid Mechanics 179, 383–405.

Hoogendoorn, C., 1977. The effect of turbulence on heat transfer at a stagnation point. International Journal of Heat and Mass Transfer 20, 1333–1338.

Huang, L., El-Genk, M. S., 1998. Heat transfer and flow visualization experiments of swirling, multi-channel, and conventional impinging jets. International Journal of Heat and Mass Transfer 41, 593–600.

Hurst, D., Vassilicos, J. C., 2007. Scalings and decay of fractal-generated turbulence. Physics of Fluids 19 (3), 035103.

Hussain, A., Zaman, K., 1981. The preferred mode of the axisymmetric jet. Journal of Fluid Mechanics 110 (39).

Ianiro, A., Cardone, G., 2012. Heat transfer rate and uniformity in multi-channel swirling impinging jets. Applied Thermal Engineering 49, 89–98.

Incropera, F. P., Lavine, A., Theodore, T., DeWitt, D., 2011. Fundamentals of Heat and Mass Transfer. John Wiley & Sons.

Jambunathan, K., Lai, E., Moss, M. A., Button, B. L., 1992. A review of heat transfer data for single circular jet impingement. International Journal of Heat and Fluid Flow 13 (2), 106–115.

Jeong, J., Hussain, F., 1995. On the identification of a vortex. Journal of Fluid Mechanics 285, 69–94.

Kolmogorov, A. N., 1941. The local structure of turbulence in incompressible viscous fluid for very large reynolds numbers. Dokl. Akad. Nauk SSSR 30.

Laizet, S., Vassilicos, J., 2011. Multi-scale unfolding mechanism for energy-efficient turbulent mixing. Physical Review Letter E 86, 046302.

Landel, J. R., Caulfield, C. P., Woods, A. W., 2012a. Meandering due to large eddies and the statistically self-similar dynamics of quasi-two-dimensional jets. Journal of Fluid Mechanics 692, 347–368.

Landel, J. R., Caulfield, C. P., Woods, A. W., 2012b. Streamwise dispersion and mixing in quasi-two-dimensional steady turbulent jets. Journal of Fluid Mechanics 711, 212–258.

Levesque, P., BrÃľmond, P., Lasserre, J., Paupert, A., Balageas, D., 2005. Performance of fpa ir cameras and their improvement by time, space and frequency data processing. part i: Intrinsic characterization of the thermographic system. QIRT Journal 2, 97–112.

Liepmann, D., Gharib, M., 1992. The role of streamwise vorticity in the near-field entrainment of round jets. Journal of Fluid Mechanics 245, 643–668.

Lumley, J., 1992. Some comments on turbulence. Physics of Fluids A 20, 015101.

Lynch, K., Scarano, F., 2014. Experimenta ldetermination of tomographic piv accuracy by a 12-camera system. Measurements Science and Technology 25, 084003.

Lynch, K., Scarano, F., 2015. An efficient and accurate approach to mteâĂŚmart for timeâĂŚresolved tomographic piv. Experiments in Fluids 56 (66).

Maas, H. G., Gruen, A., Papantoniou, D., 1993. Particle tracking velocimetry in three dimensional flows. Experiments in Fluids 15, 133.

Martin, H., 1977. Heat and mass transfer between impinging gas jets and solid surfaces. In: In: Advances in heat transfer. Volume 13. New York, Academic Press, Inc., 1977, p. 1-60. Vol. 13. pp. 1–60.

Mazellier, N., Vassilicos, J. C., 2010. Turbulence without richardson–kolmogorov cascade. Physics of Fluids 22 (7), 075101.

McAdams, W., 1954. Heat transmission. McGraw-Hill.

Meola, C., de Luca, L., Carlomagno, G. M., 1996. Influence of shear layer dynamics on impingement heat transfer. Experimental Thermal and Fluid Science 13 (1), 29–37.

Michaelis, D., Novara, M., Scarano, F., Wieneke, B., 2010. Comparison of volume reconstruction techniques at different particle densities. In: 15th Int Symp on Applications of Laser Techniques to Fluid Mechanics.

Mishra, D., Muralidhar, K., Munshi, P., 1999. A robust mart algorithm for tomographic applications. Numerical Heat Transfer 35, 485.

Moffat, R., 1988. Describing the uncertainties in experimental results. Experimental Thermal and Fluid Science 1, 3–17.

Novara, M., Batenburg, K., Scarano, F., 2010. Motion tracking-enhanced mart for tomographic piv. Measurement Science and Technology 21, 035401.

O'Donovan, T., Murray, D., 2007. Jet impingement heat transfer - part ii: A temporal investigation of heat transfer and local fluid velocities. International Journal of Heat and Mass transfer 50, 3302–3314.

Polat, S., Huang, B., Mujumdar, A. S., Douglas, W. J. M., 1989. Numerical flow and heat transfer under impinging jets: a review. Annual Review of Heat Transfer 2 (2).

Pope, S., 2000. Turbulent flows. Cambridge University Press.

Raffel, M., Willert, C. E., Wereley, S. T., Kompenhans, J., 1997. Particle Image Velocimetry: a practical guide. Springer.

Rau, M. J., Dede, E. M., Garimella, S. V., 2014. Local single- and two-phase heat transfer from an impinging cross-shaped jet. International Journal of Heat and Mass Transfer 79, 432–436.

Reichardt, H., 1943. On a new theory of free turbulence. Royal Aeronautical Sociecty Journal 47, 167–176.

Rholfs, W., Haustein, H. D., Garbrecht, O., Kneer, R., 2012. Insights into the local heat transfer of a submerged impinging jet: Influence of local flow acceleration and vortex-wall interaction. International Journal of Heat and Mass transfer 55, 7728âĂŞ7736.

Richardson, L. F., 1922. Weather Prediction by Numerical Process. Cambridge University Press.

Scarano, F., 2013. Tomographic piv: principles and practice. Measurement Science and Technology 24 (1), 012001.

Schanz, D., s. Gesemann, Schroder, A., Wieneke, B., Novara, M., 2013. Non-uniform optical transfer function in particle imaging: calibration and application to tomo- graphic reconstruction. Measurement Science and Technology 24, 024009.

Schram, C., Hirschberg, A., Verzicco, R., 2004. Sound produced by vortex pairing: prediction based on particle image velocimetry. AIAA Journal 42 (11), 2234–2244.

Seoud, R. E., Vassilicos, J. C., 2007. Dissipation and decay of fractal-generated turbulence. Physics of Fluids 19, 105108.

Soloff, S. M., Adrian, R. J., Liu, Z. C., 1997. Distortion compensation for generalized stereoscopic particle image velocimetry. Measurements Science and Technology 8 (1441).

Sreenivasan, K. R., 1984. On the scaling of the turbulence energy dissipation rate. Physics of Fluids 27, 1048.

Symes, C., Fink, L., 1977. Effects of external turbulence upon the flow past cylinders. Structure and Mechanisms in Turbulence I, 86–102.

Taylor, G. I., 1935a. Statistical theory of turbulence. Proceedings of the Royal Society A 151, 421–444.

Taylor, G. I., 1935b. Statistical theory of turbulence. ii. Proceedings of the Royal Society A 151, 444–454.

Tennekes, H., Lumley, J., 1972. A first cours in turbulence. MIT Press.

Tsai, T., 1987. A versatile camera calibration technique for high-accuracy 3d machine vision metrology using off-the-shelf cameras and lenses. IEEE Journal of Robotics and Automation 4(RA-3), 323–344.

Valente, P., Vassilicos, J. C., 2011. The decay of turbulence generated by a class of multiscale grids. Journal of Fluid Mechanics 687, 300–340.

Valente, P., Vassilicos, J. C., 2015. The energy cascade in grid-generated non-equilibrium decaying turbulence. Physics of Fluids 27, 045103.

Vassilicos, J. C., 2015. Dissipation in turbulent flows. Annual Review of Fluid Mechanics 47, 95–114.

Violato, D., Ianiro, A., Cardone, G., Scarano, F., 2012. Three-dimensional vortex dynamics and convective heat transfer in circular and chevron impinging jets. International Journal of Heat and Fluid Flow 37, 22–36.

Violato, D., Scarano, F., 2011. Three-dimensional evolution of flow structures in transitional circular and chevron jets. Physics of Fluids 23.

Violato, D., Scarano, F., 2013. Three-dimensional analysis and aeroacoustic source characterization of jet core breakdown. Physics of Fluids 25 (1), 1–31.

Viskanta, R., 1993. Heat transfer to impinging isothermal gas and flame jets. Experimental thermal and fluid science 6 (2), 111–134.

Westerweel, J., 1997. Foundamentals of digital particle image velocimetry. Measurement Science and Technology 8 (12).

Wieneke, B., 2008. Volume self-calibration for 3d particle image velocimetry. Experiments in Fluids 45, 549–556.

Willert, C. E., Gharib, M., 1991. Digital particle image velocimetry. Experiments in Fluids 10, 181–193.

Wygnanski, I., Champagne, F., Mraslu, B., 1986. On the large-scale structures in two-dimensional, small-deficit, turbulent wakes. Journal of Fluid Mechanics 168, 31–37.

Yule, A., 1978. Large-scale structure in the mixing layer of a round jet. Journal of Fluid Mechanics 89 (3), 413–432.

Zhou, D. W., Lee, S. G., Ma, C., Bergles, A., 2006. Optimization of mesh screen for enhancing jet impingement heat transfer. International journal of heat and mass transfer 42, 501–510.

Zhou, D. W., Lee, S.-J., 2004. Heat transfer enhancement of impinging jets using mesh screens. International journal of heat and mass transfer 47 (10), 2097–2108.

List of Publications

Journal Papers

- G. Cafiero, G. Ceglia, S. Discetti, A. Ianiro, T. Astarita, G. Cardone (2014). On the three-dimensional precessing jet flow pas a sudden expansion. Experiments in Fluids, 55: 1677.
- G. Cafiero, S. Discetti, T. Astarita (2014). Heat transfer enhancement of impinging jets with fractal generated turbulence. International Journal of Heat and Mass Transfer,75:173-183.
- G. Cafiero, S. Discetti, T. Astarita (2015). Flow field topology of submerged jets with fractal generated turbulence. Physics of Fluids, 27:115103.
- G. Cafiero, S. Discetti, T. Astarita (2016). Flow field features of fractal impinging jets at short nozzle to plate distances. Under review from Experimental Thermal and Fluid Science.
- G. Cafiero, G. Castrillo, C. S. Greco, T. Astarita (2016). Effect of the grid geometry on the convective heat transfer of impinging jets. Under review from International Journal of Heat and Mass Transfer.
- G. Cafiero, A. W. Woods (2016). Arrested mixing in a decaying two-dimensional turbulent wake. Under review from Journal of Fluid Mechanics.
- N. Agüera, G. Cafiero, T. Astarita, S. Discetti (2016). Enemble 3D PTV for high resolution turbulent statistics. Under review from Measurement Science and Technology.

Book Chapter

- G. Cafiero, S. Discetti, T. Astarita (2016). Flow Field Topology of Impinging Jets with Fractal Inserts. Progress in Turbulence VI, Volume 165 of the series Springer Proceedings in Physics pp 243-248.

Conference Papers

- G. Cafiero, G. Ceglia, S. Discetti, A. Ianiro, T. Astarita, G. Cardone (2013). The three-dimensional swirling flow pas a sudden expansion. 10th International Symposium on Particle Image Velocimetry, 14-16 July, Delft (NL).

- T. Astarita, S. Discetti, G. Cafiero (2013). On the offect of fractal generated turbulence on the heat transfer of circular impinging jets. American Physical Society, 66th Annual Meeting, Division of Fluid Dynamics, 24-26 November, Pittsburgh (Pennsylvania, USA).

- G. Cafiero, S. Discetti, T. Astarita (2014). Fractal turbulence generation for impinging heat transfer enhancement. 3rd EPSRC-ERCOFTAC WORKSHOP: Turbulent flows generated/designed in multiscale/fractal ways: fundamentals and applications. 23-24 March, Imperial College, London (UK).

- G. Cafiero, S. Discetti, T. Astarita (2014). Flow field features of the near-wake of jets with fractal inserts. 17th International Symposium on Applications of Laser Techniques to Fluid Mechanics. 07-10 July, Lysbon (Portugal).

- G. Cafiero, S. Discetti, T. Astarita (2014). Fluid dynamics and heat transfer features of fractal impinging jets. Workshop on: Turbulence out of classical equilibrium in nature and engineering and multiscale-generated flows. 21-24 September, Bertinoro (Italy).

- G. Cafiero, S. Discetti, T. Astarita (2014). Experimental analysis of the performance of fractal stirrers for impinging jets heat

transfer enhancement. 10th International Conference on Heat transfer, Fluid Mechanics and Thermodynamics. 14-16 July, Orlando (Florida, USA).

- G. Cafiero, S. Discetti, T. Astarita (2014). Flow field features of impinging jets with fractal grids. American Physical Society, 67th Annual Meeting, Division of Fluid Dynamics, 23-25 November, San Francisco (California, USA).

- G. Cafiero, S. Discetti, T. Astarita (2015). Large coherent structures in fractal jets. 10th Pacific Symposium on Flow Visualization and Image Processing. 15-18 June, Naples (Italy).

- S. Discetti, G. Cafiero, T. Astarita (2015). Impinging jets with fractal grids: heat transfer and flow topology. 10th Pacific Symposium on Flow Visualization and Image Processing. 15-18 June, Naples (Italy).

- G. Cafiero, S. Discetti, T. Astarita (2015). Flow field characterization of round jets with fractal grid inserts. 11th International Symposium on Particle Image Velocimetry. 14-16 September, Santa Barbara (California, USA).

- G. Cafiero, S. Discetti, T. Astarita (2015). A systematic study on the effect of the fractal geometric parameters on the heat transfer features of circular impinging jets. Multiscale-forced Turbulent Flows: fundamentals and applications. 7-8 September, Sheffield (UK).

- G. Cafiero, S. Discetti, T. Astarita (2015). Flow field topology of free and impinging jets with fractal turbulence generators: a tomographic PIV study. Multiscale-forced Turbulent Flows: fundamentals and applications. 7-8 September, Sheffield (UK).

- T. Astarita, G. Castrillo, G. Cafiero (2015). On the effect of fractal geometric parameters on the heat transfer features of circular impinging jets. American Physical Society, 68th Annual Meeting, Division of Fluid Dynamics, 23-25 November, Boston (Massachusetts, USA).

Acknowledgements

Ever since I started writing this thesis, I knew that this would have been by far the most difficult part of all, because no matters how many kind words I will spend on each one of the people I am going to mention, it will surely be not enough to thank the support, the kindness, the friendship and the happy moments that anyone have always provided and shared with me. Anyway, let's give it a try...

First of all, I am enormously grateful to my supervisor, Prof. *Tommaso Astarita*. You were the person who, in the very first place, offered me the possibility of undertaking this career and I will always be thankful to you for this. Over these years I knocked to your door an infinite number of times and you were always ready to share your knowledge and give me support and advice. Again and again, thank you. I am also grateful to my second supervisor, Prof. *Stefano Discetti*. You guided my very first steps in this field, with enormous patience and dedication. Even when you moved to Madrid, you were always ready to help me. I am proud of being your first PhD student. I wish also to thank Prof. *Gennaro Cardone*, who was ready to help me, especially technical-wise. I am thankful to Prof. *Giovanni Maria Carlomagno*: he simply represents a reference point for every person who wants to be a scientist. It was always a good moment to stop by to say hello, and just enjoy one of the myriad of stories he has collected during his career. Speaking of Professors, it is not possible to mention and thank Prof. *Andrea Ianiro*, who is for sure one of the most brilliant, motivating and annoying people I ever met. I also wish to thank Prof. *Andy Woods*, who hosted me for about 7 months in Cambridge and spent every effort to make my stay in the UK as comfortable as possible. Thank you for the very long meetings and discussions we had.

I am grateful to my good friend and former lab collegue *Giuseppe Ceglia*, aka Peppe Ce', who patiently shared a lot of hours with me in the preparation of my first PIV experiments. I am thankful to be friend with *Francesco Avallone*, universally recognized as the state of the art, with whom I also had the chance to visit a couple of countries over the world. I wish to thank (Prof.) *Carlo Greco*, whose support for basically everything that ranges from the morning breakfast to the data analysis passing through the gambling has been of paramount importance for me over these years. I also want to thank the current PhD students, *Massimo, Giusy, Mattia and Gerardo* for bearing with me when I get mad about lab-stuff and bringing always good laughs in the lab. I wish also to thank *Peppe Sicardi* for helping me with the laboratory equipments and guiding me through the Italian bureaucracy.

I am thankful to my parents and my brother, who always provided me the necessary support and never questioned my choices. I am grateful to my uncle *Vincenzo* who used to be my first sponsor and fan, and I am sure he would still be...

I wish to thank my friends, *Gloria, Giusy, Alfonso, Vanda, Simone*, for being such supportive and always ready to go out for walking (very seldom), drinking (quite often), eating (always). Really, thank you. I am grateful to *Christian*, who never stepped down when I asked him to just stop studying/working and have a beer (actually lately play some tennis). *Wave* simply represents the fact that, sometimes, no matters how may kilometers are actually between two friends, you always know that he will be there. For this, for the past and for the future, thank you. *Stefano*, if I just think to the amount of stuff we went through over the past years, first of all I have an headache (probably hangover-related), then I just wish to thank you for being there when we were flatmates, when we used to commute together, when we studied together...just thanks. *Sara*, you put me in serious troubles when I had to decide in which section write your name: I should have put you in the lab section, because you spent there at least as much time as I did, no matter how late I was; but I should have also put you in the family section, because you are the closest thing I have to a sister. In the end I decided to put you here and thank you for everything you went through with me over these years.

Marti, you were there the very first day this adventure started. You

have not only accepted my late-working, my week-end working, my period abroad, my ups and downs but you have always believed in me and motivated to do my best to pursue my ambitions. You were there the first day of the past adventure, you will be there the first day of the future one.

Gioacchino Cafiero